# CHARACTERIZATION AND MODELING OF MECHANICAL BEHAVIOR OF POLYMERS AND COMPOSITES AT SMALL SCALES BY NANOINDENTATION

by

Tingge Xu


APPROVED BY SUPERVISORY COMMITTEE:

_____

Dr. Hongbing Lu, Chair

_____

Dr. Dong Qian

_____

Dr. Terry V. Baughn

_____

Dr. Majid Minary-Jolandan

*This dissertation is dedicated to my family.*

# CHARACTERIZATION AND MODELING OF MECHANICAL BEHAVIOR OF POLYMERS AND COMPOSITES AT SMALL SCALES BY NANOINDENTATION

by

TINGGE XU, BS, MS

DISSERTATION

Presented to the Faculty of

The University of Texas at Dallas

in Partial Fulfillment

of the Requirements

for the Degree of

DOCTOR OF PHILOSOPHY IN

MECHANICAL ENGINEERING

THE UNIVERSITY OF TEXAS AT DALLAS

May 2017

# ACKNOWLEDGMENTS

As I approach the final stage of my PhD studies, I look back over my four years at The University of Texas at Dallas and feel so fortunate to have had Dr. Hongbing Lu as my advisor. I would like to express my deepest gratitude to Dr. Lu for his intelligent supervision, invaluable guidance, immense support and help over the years. Dr. Lu gave me unlimited freedom exploring new questions regarding mechanics of material. His passion in exploring new fields, his insightful ideas, enormous patience and strong encouragement have inspired the entire path of my research. Without Dr. Lu, this dissertation would never be possible. Thank you Dr. Lu, for everything you have done for me.

I also wish to give my heartiest appreciation to my dissertation committee members, Dr. Dong Qian, Dr. Terry Baughn, and Dr. Majid Minary-Jolandan. Their valuable suggestions and advice strengthened this work significantly. I would like to thank Dr. Qian, who offered two wonderful courses, which laid the solid foundation of my knowledge about the nonlinear finite element method. I would like to thank Dr. Baughn for his encouragement and guidance. He brought me into the field of mechanics of semiconductor and electronic packaging materials. His experience as a professional engineer provided invaluable information for my future career. I would also like to thank Dr. Minary for allowing me to use his equipment for my research.

I am fortunate to have many other wonderful collaborators. I would like to thank Dr. Xiao Hu Liu from IBM Thomas J. Watson Research Center, for his insights, guidance and invaluable suggestions for my future career. I would also like to thank Dr. Samit Roy at The University of Alabama for allowing me to work on an interesting composite problem. My sincere thanks to

Les Stark and James Huckabee from Texas Instruments for offering the opportunity to work on viscoelastic characterization of molding compound and die-attach adhesives.

I would extend my acknowledgments to many individuals at The University of Texas at Dallas. In particular, my earnest acknowledgments go to Dr. Huiyang Luo for his help in lots of experimental design, statistical analysis and journal manuscript preparation. I would like to thank Dr. Zhenxing Hu for fluorescent stereo microscopy and digital image correlation. My sincere thanks to Dr. Yingjie Du, who was a former PhD student of Dr. Lu, for sharing his nanoindentation experience. I would like to thank Zhe Xu for his help on AFM and SEM. I would also thank Dr. Jeong-Bong Lee, Dr. Jun-Hyeon Yoo and Sachin Babu for UV-lithography. I would thank Dr. Ray H. Baughman, Dr. Shaoli Fang, Dr. Na Li and Dr. Jing Lu for providing carbon nanotube sheets. Moreover, I wish to express my sincere gratitude to all my friends and colleagues who provided suggestions and assistance in and out of the lab during my time at UTD. Just to name a few: Dr. Jiangtao Di, Dr. Wenwei Jiang, Dr. Kui Tan, Xuemin Wang, Kevin Huang, Rui Zhang, Peiyuan Kang, Mahmoud Baniasadi, Mohammad Karim, Shogo Wada, and Clint Nicely.

Finally, I am very grateful to my parents, Mr. Jin Xu and Ms. Ke Li, for their endless support and love.

February 2017

CHARACTERIZATION AND MODELING OF MECHANICAL BEHAVIOR OF POLYMERS AND COMPOSITES AT SMALL SCALES BY NANOINDENTATION

Tingge Xu, PhD
The University of Texas at Dallas, 2017

Supervising Professor: Dr. Hongbing Lu

Polymer has been used extensively for the final MEMS structures or devices. In order to ensure the design reliability, it is critical to precisely determine the mechanical properties of the polymer-based electronic packaging materials at microscale. In recent years, nanoindentation technique is gradually becoming an effective technique for determining the local mechanical properties at the microscale and nanoscale. In this study, the mechanical properties of SU-8, a photoresist material of great interest to MEMS community, were measured under both micropillar compression and nanoindentation on a film on a substrate by nanoindentation. Measurement results in literature characterizing the mechanical behavior of SU-8, by elastic-plastic analysis of nanoindentation data, have shown to provide incorrect results. In this study, an appropriate viscoelastic analysis of nanoindentation load-displacement data was conducted, the time-average Young's modulus at a given strain rate was determined to be near 3.6 GPa, which agrees with the reported values in literature obtained from tension and bending, and also correlates reasonably well with data from microcompression. This work indicates that

viscoelastic analysis is necessary to extract the valid mechanical properties at nano/microscales for SU-8.

The same viscoelastic analysis approach has also been applied to characterize the mechanical properties of a molding compound on a packaged integrated circuit (IC) by spherical nanoindentation using a 50 μm radius diamond tip. The molding compound is a heterogeneous material, consisting of assorted diameters of glass beads embedded in an epoxy. Statistical analysis was conducted to determine the representative volume element (RVE) size for a nanoindentation grid. Nanoindentation was made on the RVE to determine the effective viscoelastic properties. The relaxation functions were converted to temperature-dependent Young's modulus at a given strain rate at several elevated temperatures. The spatial distribution of the Young's modulus at a given strain rate was also determined using nanoindentation with a Berkovich tip.

In addition to the application on MEMS structure, nanoindentation technique has also been extended to characterize the fiber reinforced polymer matrix composites, which have found increasing applications in such areas as aerospace, automotive, wind farms, offshore drilling, sports, and construction. In this study, Fiber push-in nanoindentation was conducted on a unidirectional carbon fiber reinforced bismaleimide resin composite (IM7/BMI) subjected to environmental degradation to determine the interfacial shear strength. It was found that thermal oxidation at 245$^{o}$C in air leads to a significant reduction in interfacial shear strength of the IM7/BMI unidirectional composite. Moisture-saturated specimens under thermal shock showed a significant reduction in interfacial shear strength as well.

It is thus encouraged to increase the interfacial strength of fiber reinforced polymer matrix composites. In this study, we propose using multiwall carbon nanotube sheet to spiral-wrap around an individual carbon fiber for enhancement of mechanical properties of the fiber/matrix interphase that directly influences the fiber/matrix debond strength and compressive strength of the composite. Different methods were used in experiments to characterize the interfacial shear strengths. All experimental results show consistently a significant improvement in interfacial shear strength by using MWNT scrolled carbon fibers in a composite.

TABLE OF CONTENTS

LIST OF FIGURES

LIST OF TABLES

# CHAPTER 1

# INTRODUCTION

## 1.1 Introduction

In recent years nanoindentation technique, also known as depth-sensing indentation, is gradually becoming an effective technique for determining the local mechanical properties at the microscale and nanoscale. The areas of its applications have been growing in the past 25 years due to the commercial availability of nanoindentation instrumentation and the ease of applying the technique to measure mechanical properties of very small amounts of materials, such as thin solid films deposited on substrate, wires, components in microelectromechanical and nanoelectromechanical systems (MEMS/NEMS). Nanoindentation Methods for measuring the elastic-plastic properties, such as Young's modulus and hardness, have been well established by Oliver and Pharr [1, 2]. The Oliver-Pharr method simplifies nanoindentation experiment procedures significantly on elastic-plastic material, due to the fact that the contact area is measured at submicron resolution through indenter shape calibration, which does not require to image the nanoindentation impression optically, as conventional indentation experiments did.

The materials used by the MEMS and NEMS industries are not only the typical silicon-based materials, but also metals, ceramics and polymers. For the proper functioning of MEMS/NEMS, it is important to calculate the stress and deformation to ensure the design reliability. To this end, it is critical to determine the mechanical properties of the electronic packaging materials at microscale for stress analysis of the MEMS. While nanoindentation technique has been widely used to measure mechanical properties of elastic-plastic component on MEMS, it has attracted increasing attention for measuring mechanical properties of

viscoelastic materials, such as polymers. The Oliver-Pharr method, however, experiences difficulties to measure the mechanical properties of viscoelastic materials. One well-known phenomenon is the formation of unloading "nose" or negative stiffness during unloading that often occurs during slow loading-unloading history in nanoindentation on a viscoelastic material. Thus, measurement results in the literature characterizing the mechanical behavior of viscoelastic components on MEMS, by the Oliver-Pharr method, have shown to provide incorrect results. Numerous approaches have been developed to measure the mechanical properties of viscoelastic materials [3-5]. Lu *et al* [3] developed a method to measure the creep compliance of polymers using either a Berkovich or a spherical indenter tip, by analyzing the nanoindentaion loading curve. The creep compliance can be converted to the time-average Young's modulus at a given strain rate [3].

In this study, we will use this method to determine the time-average Young's modulus of SU-8 thin film, which is a negative photoresist material of great interest of the MEMS community. We find that nanoindentation of SU-8 can be successfully modeled and therefore used for the extraction of mechanical properties from SU-8, if this material is analyzed as a viscoelastic material. The method in general and the extracted values in particular are definitely of interest to the MEMS community in view of the design of SU-8 MEMS devices.

In accelerated life testing for an integrated circuit (IC) under thermal cycling, the molding compound can play a significant role on the active device, wire bonds and package leads, and result in mechanical failure. In this study, we will addresses an important question, related to prediction of the lifespan of integrated circuits exposed to thermal cycling. The goal is to determine time dependent behavior of molding compound. The experiments were performed on

end predict itself, using nanoindentation technique and results were compared to measurements performed on bulk specimen made from the dame material.

In addition to the application on MEMS structure, nanoindentation technique has also been extended to characterize the fiber reinforced polymer matrix composites, which have found increasing applications in such areas as aerospace, automotive, wind farms, offshore drilling, sports, and construction. In these composites failure manifests in one of the four primary modes: fiber microbuckling in compression, fiber/matrix interfacial debonding, fiber fracture (or fragmentation), and matrix cracking. Load transfer has to take place through the interface between the fiber and polymer matrix, and the matrix is primarily responsible for shear load transfer. In this investigation, fiber push-in nanoindentation was conducted on a unidirectional carbon fiber reinforced bismaleimide resin composite (IM7/BMI), subjected to environmental degradation, to determine the interfacial shear strength. It is evident that extensive thermal oxidation and steam blistering degrade the fiber/matrix bonding, which makes it easier to initiate and propagate microcracks along the interface, potentially leading to global failure of the structural components in aircraft.

It is thus encouraged towards increase the interfacial strength of fiber reinforced polymer matrix composites. In this study, we propose to use CNT sheet to spiral-wrap around an individual carbon fiber for enhancement of mechanical properties of the fiber/matrix interphase that directly influences the fiber/matrix debond strength and compressive strength of the composite.

This dissertation is divided to the following six chapters. The first chapter here gives general introduction and background on the nanoindentation. Chapter 2 presents the mechanical

characterization of SU-8 by compression of micropillars and nanoindentation on a film supported by a substrate, taking the viscoelastic effect into account. Chapter 3 describes the mechanical properties of a molding compound on a packaged integrated circuits at service temperatures. Chapter 4 presents fiber push-in experiments and simulations on evaluating the effects of thermal oxidation and steam blistering on the interface behavior of IM7/BMI unidirectional composite. Chapter 5 discusses the novel approach to improve the interface strength of polymer matrix composite, by using carbon nanotube sheet scrolled carbon fibers. Chapter 6 discusses the general conclusions and future work. Each chapter has an introductory remarks specific to the topic and conclusions of the findings.

## 1.2 References


1. Oliver, Warren Carl, and George Mathews Pharr. "An improved technique for determining hardness and elastic modulus using load and displacement sensing indentation experiments." *Journal of materials research* 7, no. 06 (1992): 1564-1583.

2. Oliver, Warren C., and Georges M. Pharr. "Measurement of hardness and elastic modulus by instrumented indentation: Advances in understanding and refinements to methodology." *Journal of materials research* 19, no. 01 (2004): 3-20.

3. Lu, H., B. Wang, J. Ma, G. Huang, and H. Viswanathan. "Measurement of creep compliance of solid polymers by nanoindentation." *Mechanics of time-dependent materials* 7, no. 3-4 (2003): 189-207.

4. Huang, G., and H. Lu. "Measurements of two independent viscoelastic functions by nanoindentation." *Experimental Mechanics* 47, no. 1 (2007): 87-98.

5. Cheng, Yang-Tse, Che-Min Cheng, and Wangyang Ni. "Methods of obtaining instantaneous modulus of viscoelastic solids using displacement-controlled instrumented indentation with axisymmetric indenters of arbitrary smooth profiles." *Materials Science and Engineering: A* 423, no. 1 (2006): 2-7.

# CHAPTER 2

# CHARACTERIZATION OF THE MECHANICAL BEHAVIOR OF SU-8 AT MICROSCALE BY VISOELASTIC ANALYSIS*

## 2.1 Introduction

Ever since its invention by IBM [1], the epoxy-based negative photoresist SU-8 has been used extensively for nano/micro-fabrication, for lithography, as a sacrificial micro-mold for electroplating, and also as the final microstructures in MEMS, including micro gears [2], optical waveguide [3], microfluidic channel [4], micro-cantilevers for atomic force microscopy [5], and neural probes [6]. The widespread applications derive from its unique set of properties including exceptional photosensitivity, ease of manipulations, mechanical stiffness and strength, and thermal and chemical stability [7, 8].

In recent years, there is an increasing trend in the use of SU-8 for the final MEMS structures or devices. Proper estimation of mechanical properties of SU-8 is certainly beneficial in some of the devices such as SU-8 microneedle [9] and SU-8 implantable neural interface devices [6, 10]. It is crucial to have precisely measured mechanical properties of SU-8 at microscale for certain applications such SU-8-based intraocular pressure sensor [11] and SU-8 cantilever-based sensors [12, 13].

For the proper functioning of SU-8, it is important to calculate the stress and deformation to ensure the design reliability. To this end, it is critical to determine the mechanical properties of

---

* Reprinted with permission from "Xu, Tingge, Jun Hyeon Yoo, Sachin Babu, Samit Roy, Jeong-Bong Lee, and Hongbing Lu. "Characterization of the mechanical behavior of SU-8 at microscale by viscoelastic analysis." Journal of Micromechanics and Microengineering 26, no. 10 (2016): 105001." Published August 23, 2016. doi:10.1088/0960-1317/26/10/105001 

SU-8 at microscale for stress analysis of the SU-8 MEMS. The reported glass-transition temperature ($T_g$) for fully crosslinked SU-8 is over 200°C, and the degradation temperature ($T_d$) is around 380 °C [1]. To determine the bi-axial elastic modulus and the coefficient of thermal expansion (CTE), Lorenz et al. [7-8] measured the bow response of a 20 μm thick SU-8 film on both Si and Al substrates after being subjected to a thermal cycling ($\Delta T$=75°C). The reported bi-axial modulus was 5.18 GPa, and the CTE was 52 ppm/°C. They also measured the friction coefficient, yielding a value of 0.19. Numerous results have been reported for the Young's modulus of SU-8 [14-26]. The reported Young's modulus varies from 0.9 to 7.4 GPa. Lorenz *et al* reported a tensile modulus of 4.02 GPa for a 200 μm SU-8 film [14]. Namazu et al. [15] conducted tensile tests on microscale and macroscale SU-8 specimens, and reported a Young's modulus of 3.5 GPa for samples of all sizes tested. Robin et al. [16, 17] conducted in-situ microtensile tests under a scanning electron microscope, and reported Young's modulus values between 2.3 and 4.4 GPa, at different strain rates and sample preparation conditions. In addition to tension, nanoindentation was made on SU-8 thin films [18-24], and gave a Young's modulus value that is typically 1.5 to 2 times of the data obtained from microtension or bending [23].

It has been determined for many metal and polymer materials that its mechanical properties depend on the size [27-29]. It is in general a belief that SU-8 shows size-effect in the mechanical properties. Robin et al. [17] investigated the size effect of SU-8, and found that the mechanical properties depend on the size of the SU-8 sample when the sample thickness is smaller than 2 μm. For micropillar compression experiments reported in literature, focused ion beam (FIB) was often used to prepare a micropillar specimen. That approach is not appropriate for polymer because it can induce significant surface defects due to the interaction of the high-energy Ga ions

with polymer [30]. In addition, if FIB is used to prepare a SU-8 micropillar, the micropillar will be supported by the SU-8 substrate. Under microcompression, the micropillar has a tendency to sink into the substrate, making it difficult to calculate the mechanical properties of the micropillar [31].

In this paper, we used ultraviolet (UV) lithography process to prepare SU-8 micropillars on silicon substrate, so that it is accurate to calculate the resulting stress and strain under compression to determine the mechanical properties of SU-8 micropillars of different diameters. The micropillars prepares using this process do not have beam damage on the surface typically accompanied by micropillars prepared by focused ion beam [29]. The micropillars were subsequently compressed using a flat-ended tip under a nanoindenter to measure the mechanical response.

In addition to micropillar compression in this paper, we also carried out nanoindentation on a SU-8 film supported by a substrate to measure the properties. This is a convenient approach, which was used extensively for characterization of the mechanical properties of small amounts of polymers. Wouters et al. carried out nanoindentation experiments on SU-8, and found that the Young's modulus determined from nanoindentation was different from those obtained in tension or bending experiments [23]. They indicated that the Oliver-Pharr method [32, 33] for nanoindentation is not appropriate for measurement of Young's modulus for SU-8, and that numerous testing conditions, including loading/unloading rate and holding time, can affect the results. As reported by Namazu et al., SU-8 exhibits viscoelastic behavior even at room temperature [15]. As such, the Oliver-Pharr method experiences difficulties to measure the mechanical properties of viscoelastic materials since the method does not take into account of

viscoelastic behavior. For a viscoelastic material, the fading memory effects are present in the nanoindentation load-displacement curve. A well-known phenomenon is the formation of unloading "noise" giving negative stiffness during slow unloading [34, 35]. Therefore viscoelastic analysis is necessary to measure the accurate mechanical properties of a polymer by nanoindentation, even a fast loading/unloading rate is applied: there is a tendency for the Oliver-Pharr approach to overestimate the Young's modulus [36]. Numerous approaches have been developed to measure the mechanical properties of viscoelastic materials [36-38]. Lu et al. [36] developed a method to measure the creep compliance of polymers using either a Berkovich or a spherical indenter tip, by analyzing the nanoindentaion loading curve. The creep compliance can be converted to the time-average Young's modulus at a given strain rate [36]. This approach has been applied to composites [39, 40], biomedical materials [41, 42], and other time-dependent materials. In this paper, we will use this method to determine the time-average Young's modulus of SU-8 thin film at a given strain rate, and examine the validity of the nanoindentation technique for SU-8.

## 2.2 Experimental details

### 2.2.1 Sample preparation

An array of circular cylindrical SU-8 micropillars with diameters of 6 ~ 18 μm and a pitch of 100 μm was fabricated with lithography process, as shown in Figure 2.1. SU-8 2025 (MicroChem Inc., Woburn, MA) was first spin-coated on silicon wafer to form a 25 μm thick SU-8 film. The SU-8 on the substrate was subsequently soft baked on a hot plate at 65°C for 3 minutes, at 95°C for 5 minutes, and it was then cooled down to and baked at 65 °C for 3 minutes. After that an

ultraviolet (UV) light dose of 160 mJ/cm$^2$ was used to form the micropillar array as shown in Figure 2.1(c). Next, the SU-8 sample was baked again with the same procedures used in the soft bake process. The actual height of a micropillar as measured by a profilometer was 24.1 μm. It is noted that the SU-8 micropillars fabricated in this way are slightly tapered, with a tapering angle near 2$^o$. The diameter at the top surface is close to the nominal value, while the diameter at the bottom surface is smaller than the nominal value.

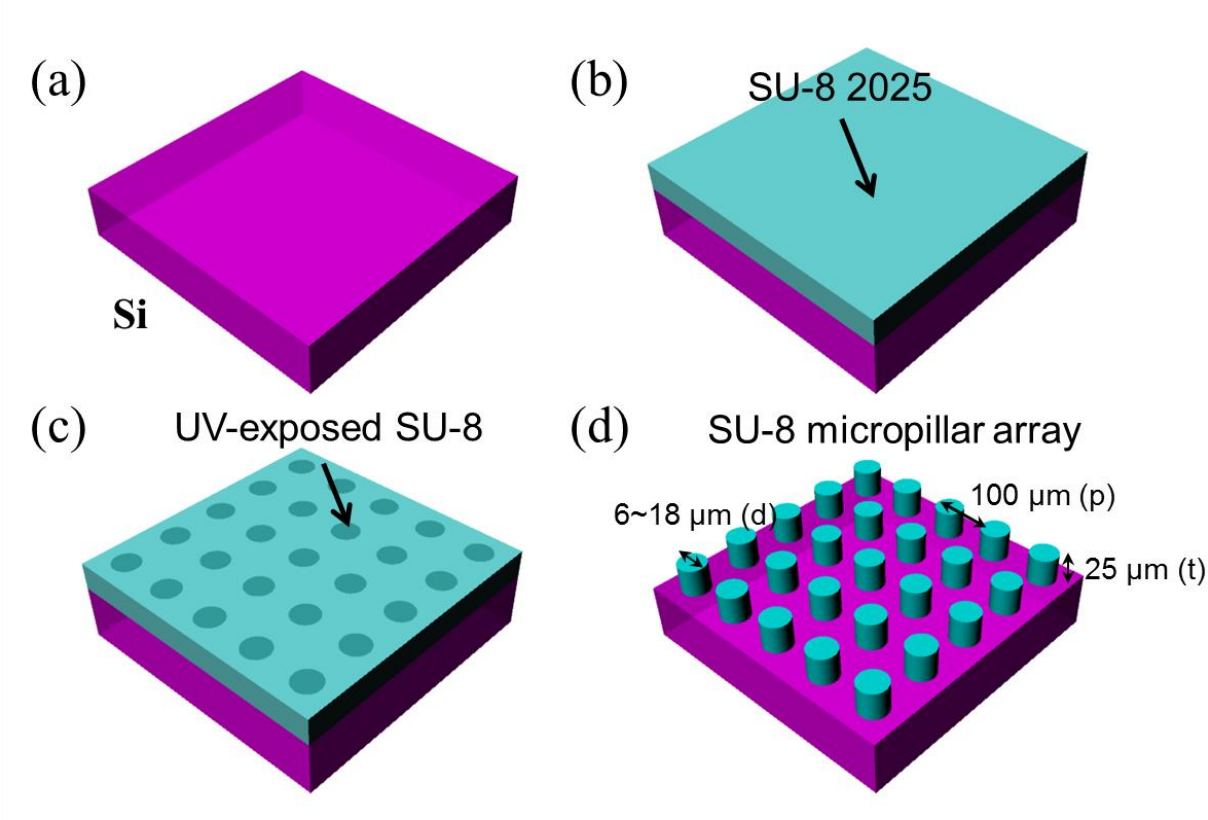


Figure 2.1. Fabrication sequence of SU-8 micropillar for nanoindentation testing (a) bare silicon wafer (b) SU-8 2025 spin coating (c) UV-expose (d) patterned SU-8 micropillar with various sizes.

### 2.2.2 Microcompression of a SU-8 micropillar

Once the SU-8 micropillar array was fabricated, microcompression on a micropillar was conducted on an Agilent G200 nanoindentation system. The nanoindentation system can reach a maximum indentation depth of 500 μm (resolution of 0.2 nm) and a maximum load of 500 mN (resolution of 50 nN). A diamond flat punch tip, with 100 μm diameter was used as a compression platen for this microcompression. The diameter of the flat punch was larger than SU-8 micropillars, thus resulting in a uniaxial compression configuration. All the microcompression experiments were conducted under load-controlled conditions. Since the Agilent G200 system is inherently a load-controlled equipment, it is convenient and better suited for the measurement performed under load-controlled loading history [43]. Care was taken to minimize the effect of dust or other particles between flat punch indenter and the micropillar sample surface, the diamond flat punch was cleaned before testing, and the samples were prepared and stored in sealed storage cases in the clean-room facility. To make sure that the indenter tip is in full contact with the top surface of a micropillar, calibration was performed to obtain an accurate lateral position of the flat punch relative to the sample surface with the use of an optical microscope on the nanoindentation system. More experimental details are described in [28, 33].

Microcompression experiments were conducted on SU-8 micropillars of diameters of 8, 12 and 16 μm at constant loading rates of 0.05, 0.5, and 5 mN/s to investigate the effect of loading rate. For micropillars with the same diameters, the same maximum load was reached, while the loading rates were controlled and varied by specifying the duration of the loading time. Microcompression was also conducted on micropillars with diameters of 6, 8, 10, 12, 14, 16 and

18 μm, under a fixed loading rate to investigate the sample size effect, if any. Care has been taken to avoid buckling. The Euler's buckling load $F=\pi^2 EI/H_e^2$, where $E$ is the Young's modulus, $I$ is the area moment of inertia of the cross section, and $H_e$ is the effective height of the micropillar (in this case equals half of the height of the micropillars), respectively. If the slenderness ratio (effective height to the radius of gyration) is smaller than $\sqrt{2\pi^2 E/\sigma_y}$, the Euler formula gives a unit load (critical load divided by cross sectional area) higher than the yield stress $\sigma_y$ of the materiel; under such a situation, the Johnson formula is appropriate, in which case, the buckling load $F=\sigma_y A[1-\left(\frac{\sigma_y}{4\pi^2 E}\right)\left(\frac{H_e}{r}\right)^2]$, where $A$ is the cross section area and $r$ is the radius of gyration. In this study, the aspect ratios (height to radius) of micropillars are at or smaller than 4, corresponding to a slenderness ratio of 2. Using estimated values for Young's modulus and yield stress for SU-8, when at an aspect ratio of 4, the SU-8 micropillar will not experience buckling before yielding occurs. The load-displacement data obtained from microcompression on the nanoindentation system converted to stress-strain relationship. Eight or more experiments were conducted under same conditions (loading rate, micropillar size) to obtain reproducible data.

### 2.2.3 Nanoindentation on SU-8 thin film

In addition to microcompression on a micropillar, nanoindentation on a SU-8 thin film was also conducted on film prepared by the same process as described in Section 2.1. The thickness of the thin-film was around 21 μm. The same Agilent G200 nanoindentation system was used, with a diamond Berkvoich indenter tip. A maximum load of 5 mN was applied on the indenter tip with

constant loading rates of 0.25, 1, and 2.5 mN/s, with a holding time of 10 s. All experiments were conducted at room temperature.

## 2.3 Results and discussion

### 2.3.1 Microcompression of SU-8 micropillars

**Engineering stress-strain curves**

The engineering stress-strain relationships were calculated from the load-displacement data acquired during microcompression experiments. Figure 2.2 shows typical load-displacement curves at a loading rate of 0.5 mN/s for eight SU-8 micropillars with a diameter of 18 μm. The nonlinear region, designated as "toe" region, below 200 nm is due to the imperfect contact between the micropillar and flat punch tip. It is followed by a linear region, which ends with yielding at the onset of nonlinearity. This is followed by strain burst, corresponding to a plateau region, leading to failure of the micropillar. This observation is consistent with results reported previously on single crystal micropillars [28, 30]. To the best of our knowledge, this paper reports the first set of results for microcompression of SU-8 micropillars. The load-displacement curves obtained from micropillars with the same diameter are highly reproducible. Consequently, highly repeatable results have also been obtained for micropillars with different diameters. The undeformed and deformed shapes of the 18 μm diameter SU-8 micropillars are shown in Figure 2.3. It is noted that the bottom end of a SU-8 micropillar is supported by the rigid silicon wafer. Therefore, there is no sink-in of the micropillar into the substrate, as confirmed in Figure 2.3(b). Microcompression experiments were conducted on several different diameters with several different loading rates to investigate the size effect and rate-dependent behavior, if any.

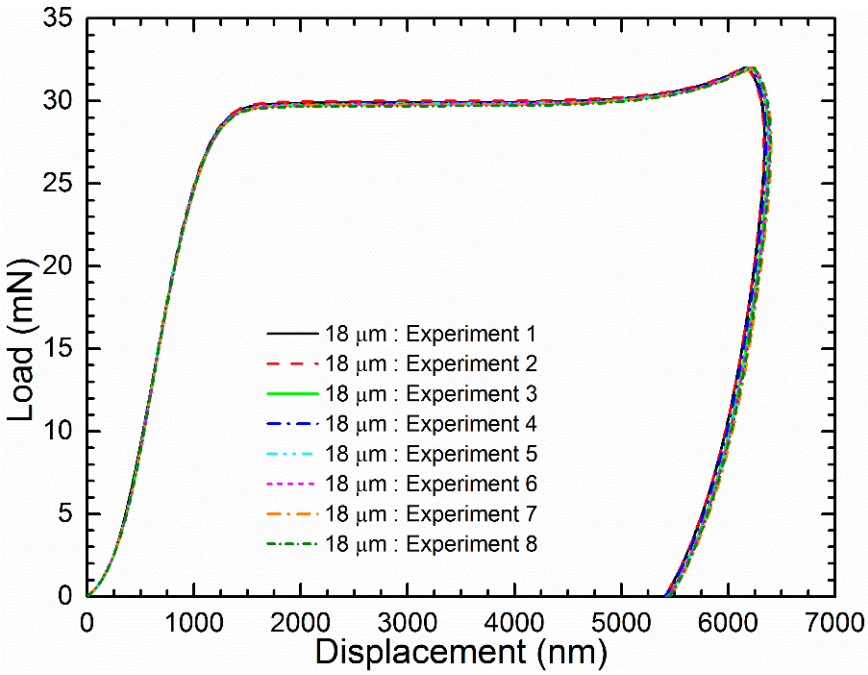


Figure 2.2. Typical microcompression load-displacement curves for SU-8 micropillars at a loading rate 0.5 mN/s. Curves from eight microcompression experiments are plotted. The curves are highly reproducible, with a difference within 1% in loading portion where data is analyzed to determine mechanical properties of SU-8.

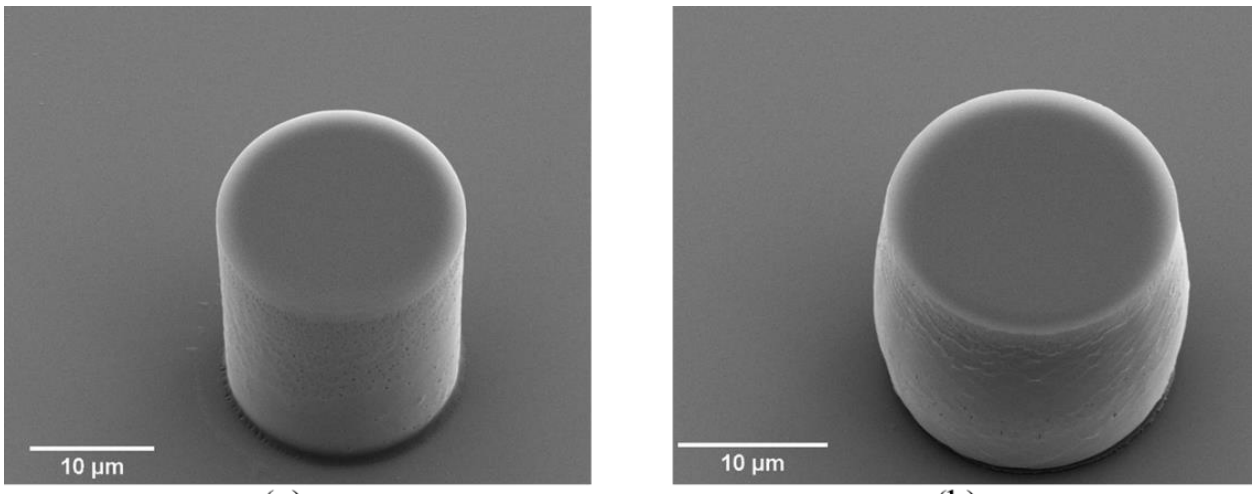


(a) (b)

Figure 2.3. (a) SEM micrograph for an undeformed SU-8 micropillar with 18 $\mu$m diameter (b) deformed shape of a SU-8 micropillar with 18 μm diameter. With the use of an aspect ratio at or smaller than 4 buckling was not observed in microcompression.

The micropillars fabricated by UV lithography is slightly tapered with a tapering angle of 2-3$^{o}$, due to the deep etching process used for the micropillars. The tapered geometry of the micropillar is next considered to calculate stress and strain data, following the methods by Zhang et al. [44] and Shin et al. [31]. With the consideration of the tapered geometry of a micropillar, the Young's modulus $E$ could be calculated using [45]

$$E = \frac{4PH}{\pi D_0 (D_0 - 2H \tan\theta)\delta} \tag{2.1}$$

where $P$ is the compressive force, $H$ is the height of the micropillar, $D_0$ is the maximum diameter of the micropillar, $\theta$ is the tapering angle, and $\delta$ is the displacement.

To calculate the stress, the compressive force was divided by the cross section area of the micropillar. Previous studies by Zhang et al. [44] and Frick et al. [46] suggested the use of the diameter at the mid-span of the micropillar to calculate the cross section area for stress calculation. This approach has been generally accepted [31, 47-49].

To verify this approach, we conducted finite element method (FEM) simulations. Microcompression of a SU-8 micropillar was simulated using ABAQUS standard V6.14 [50]. An axisymmetric model was established and the typical meshes for a SU-8 micropillar are shown in Figure 2.4. Approximately 6,000 and 18,000 CAX4R elements were used, for 6 μm and 18 μm diameter micropillars, respectively. The micropillar height was 25 μm for both simulations. The flat punch indenter tip and substrate were modeled as rigid. Mesh convergence studies were conducted to ensure that proper mesh refinement has been achieved.

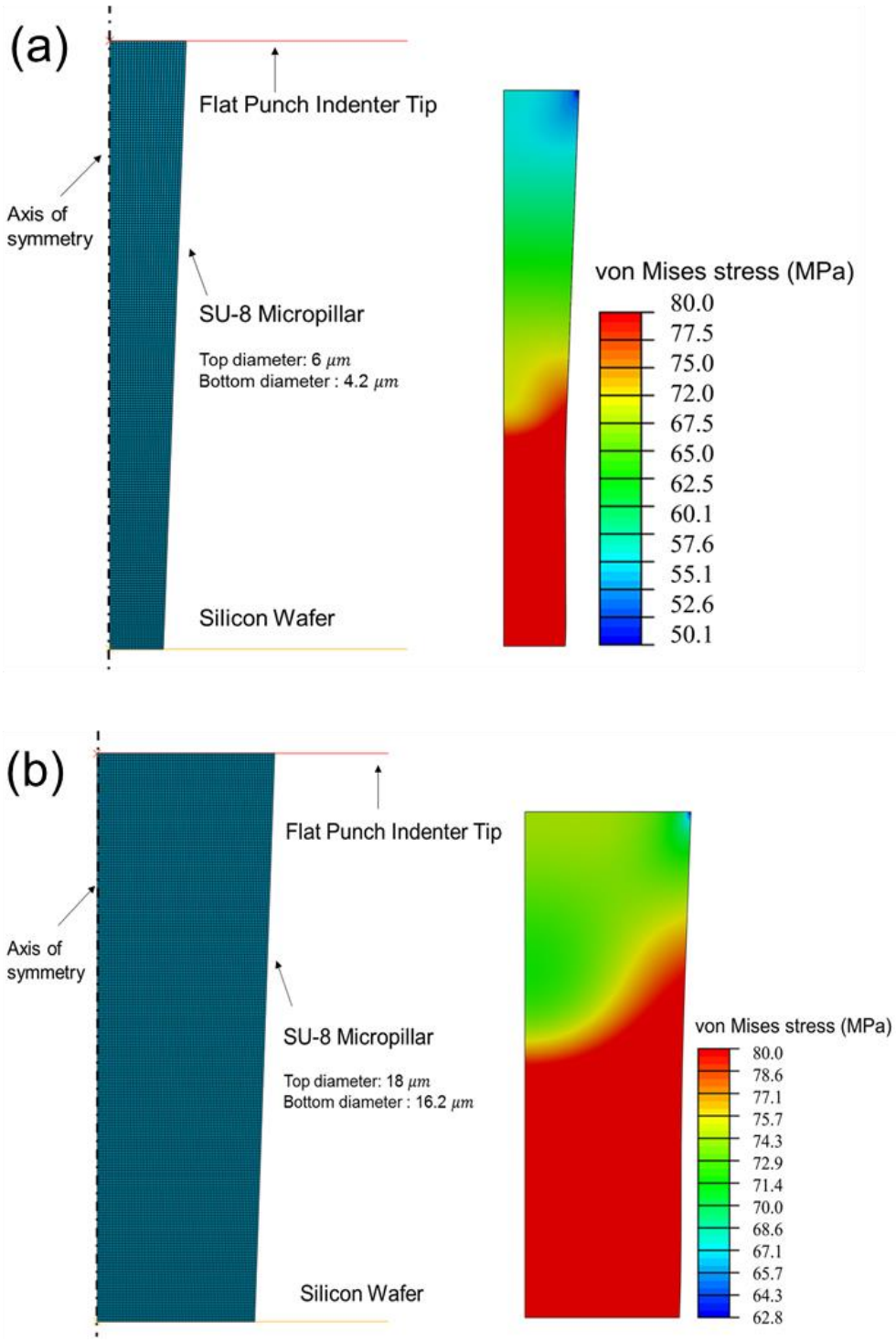


Figure 2.4. FEM simulations (a) Typical mesh and von Mises stress map at a deformed state for a micropillar with 6 µm diameter, a half model is shown (b) Typical mesh and von Mises stress contour plot at a deformed state for a micropillar with 18 µm diameter, a half model is shown.

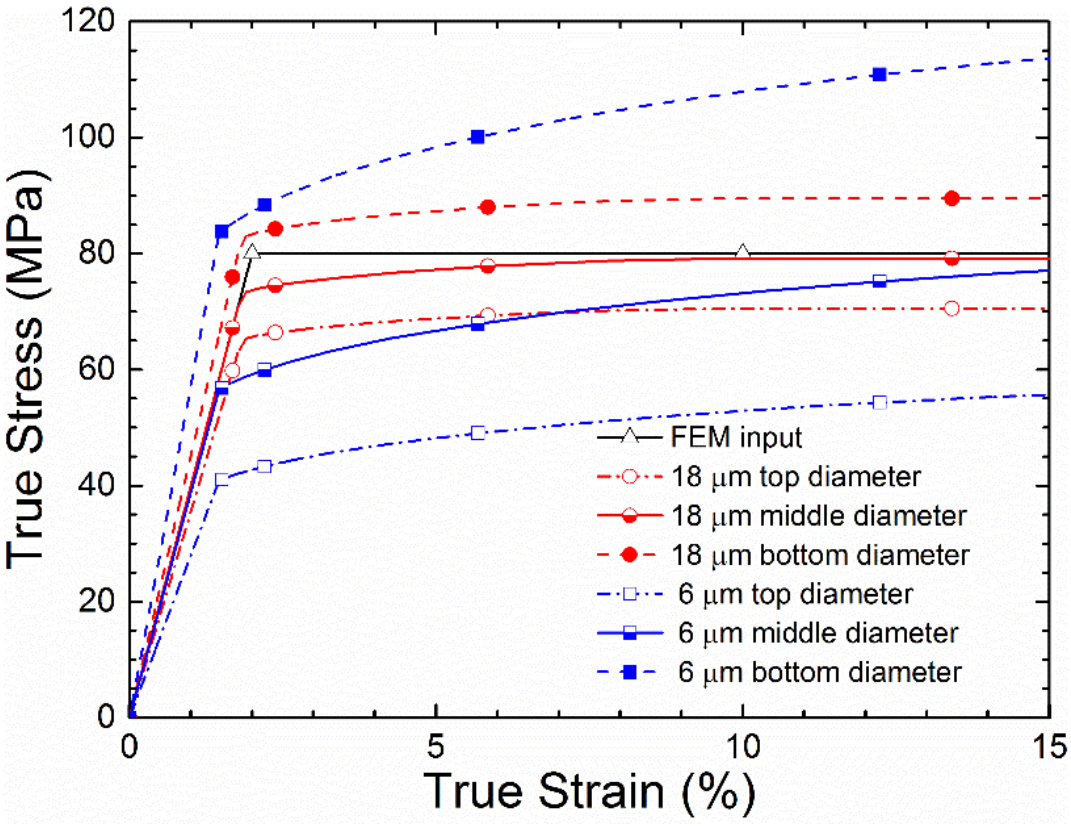


Figure 2.5. Comparison of the true stress-strain relationships. The black dash-dot line provides the input stress-strain relationship in ABAQUS simulations; the other lines are the recovered results from FEM simulations considering the tapered geometry.

Since the load-displacement curves shown in Figure 2.2 resemble the behavior of an elastic-perfectly plastic material, an elastic-perfectly plastic model was used in FEM simulations. The Young's modulus and yield strength were taken as 4 GPa and 80 MPa, respectively for the model. Figure 2.4(a) and 4(b) show contours of von Mises stress on the deformed configurations for 6 μm and 18 μm diameter micropillars, respectively. Stress concentration occurs due to the tapered geometry at the bottom end of the micropillar, which leads to yielding in the region where the stress reaches the yield strength. To investigate the effect of the tapered geometry, the top, middle and bottom diameter for each micropillar were used to calculate the engineering

stress, respectively. The input to the FEM simulations is shown by the black dash-dot line. As indicated in Figure 2.5, using top diameter underestimates the Young's modulus and yield strength, while the use of the bottom diameter overestimates the mechanical properties. The degree of inaccuracy increases as the micropillar diameter decreases. However, if the diameter of the mid-span of the micropillar is selected as the reference diameter, a very good agreement with FEM on Young's modulus is observed, as shown in Figure 2.5.

Performing FEM simulations shows that it is appropriate to take the diameter of the mid-span of the micropillar's cross-sectional area for the calculation of the Young's modulus. However, the yield strength determined by the mid-span diameter is still underestimated, and the error increases as the diameter of micropillar decreases. In this paper, we labeled the size of the micropillars using the diameter of the top surface. The diameter of the mid-span of the micropillar was used for calculating engineering stress.

**Effect of Loading Rate**

Figure 2.6 shows the engineering stress-strain curves of micropillars with different diameters subject at several loading rates. Each curve represents the average data from five independent microcompression experiments, the differences in results obtained from different experiments are in general within 1%; the error bars are not plotted since they are nearly invisible. Due to uncertainties (mainly noisy data in results obtained from short times in the loading period) in experimental data for microcompression on 8 μm micropillars at a loading rate of 5 mN/s, those data are not included in Figure 2.6. In Figure 2.6, toe correction at small strains, up to 0.8% has been made on these curves following the ASTM Standard D695-15 [51]. All the engineering stress-strain curves are plotted up to the strain level of 8%. The calculation of the Young's

modulus relies primarily on the data outside of the toe region, typically at strains between 0.8% and 3.5%. Figure 2.6 indicates that both Young's modulus and compressive yield strength increase with the increase of loading rate. These results show that SU-8 exhibits rate-dependent behavior even at room temperature.

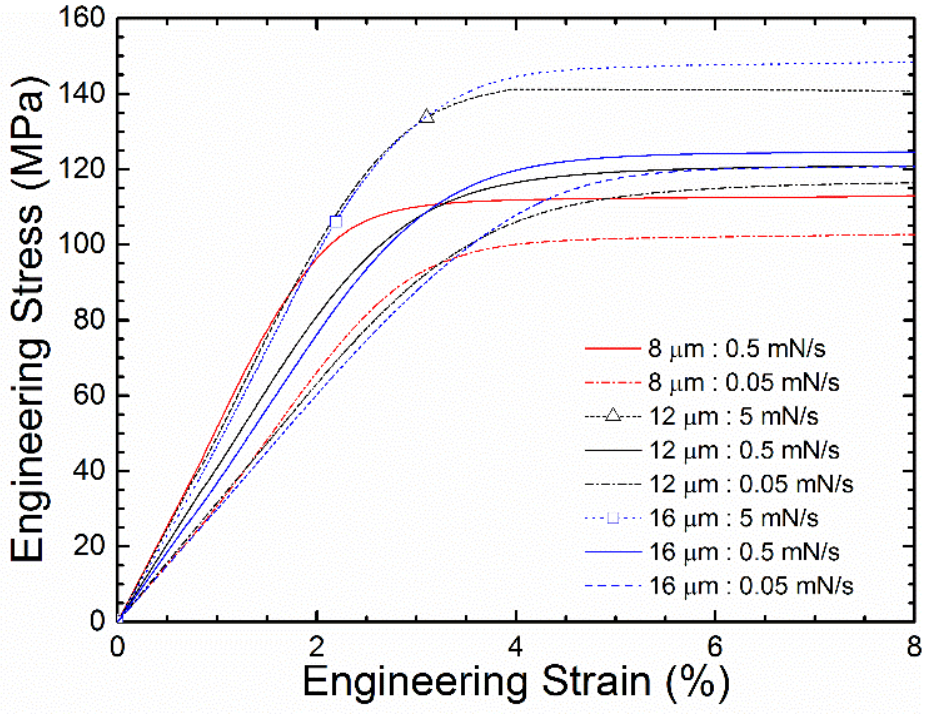


Figure 2.6. Microcompression experiments data: engineering stress-strain curves for SU-8 micropillars at different loading rates. One curve corresponds to the average data from five independent microcompression experiments. The differences in results obtained from different experiments are in general within 1%; the error bars are not plotted since they are nearly invisible.

**Viscoelastic Analysis of Microcompression of SU-8 micropillars**

Since SU-8 exhibits viscoelastic behavior at room temperature, viscoelastic analysis is used on experimental data. The load-displacement data obtained in microcompression experiments was used to calculate the time-average Young's modulus at a given strain rate, using viscoelastic analysis. Following a similar approach shown in [36,52,53], the time-dependent

microcompression displacement $\delta(t)$, under a prescribed arbitrary compressive loading history $P(t)$ in a viscoelastic material, is given by,

$$\delta(t) = \frac{4H}{\pi D_0 (D_0 - 2H\tan\theta)} \int_0^t C(t-\xi)\left[\frac{dP(\xi)}{d\xi}\right] d\xi \tag{2.2}$$

where $C(t)$ is the uniaxial creep compliance. $H$ is the height of the micropillar, $D_0$ is the maximum diameter of the micropillar. The general representation of the creep function based on the Kelvin model is,

$$C(t) = C_0 + \sum_{i=1}^{N} C_i (1 - e^{-t/\tau_i}) \tag{2.3}$$

where $C_0$ and $C_i$ ($i$=1,…$N$) are creep coefficients and $\tau_i$ ($i$=1,…$N$) are retardation times. Under a constant rate loading history, $P(t) = \dot{P}_o t H(t)$, where $\dot{P}_o$ is the constant loading rate, $t$ is elapsed time, substituting Equation (2.3) into (2.2) yields,

$$\delta(t) = \frac{4H}{\pi D_0 (D_0 - 2H\tan\theta)} \left[ (C_0 + \sum_{i=1}^{N} C_i) P(t) - \sum_{i=1}^{N} C_i (\dot{P}_o \tau_i)(1 - e^{-P(t)/(\dot{P}_0 \tau_i)}) \right] \tag{2.4}$$

By fitting Equation (2.4) to the experimental load-displacement curves, the best-fit parameters $C_0$ and $C_i$ can be determined. Once $C_0$ and the $C_i$ are determined, Equation (2.3) is used to calculate the creep compliance $C(t)$. The Young's relaxation modulus $E(t)$, is determined using the Volterra equation [54],

$$\int_0^t E(\xi) C(t-\xi) d\xi = t \tag{2.5}$$

Although Equation (2.5) is ill-posed [55, 56], errors in the relaxation modulus can be minimized if the creep compliance data is developed for very short times. The algorithm recently developed by Luk-Cyr et al. [57] was implemented to avoid the ill-posed issue of the Volterra equation.

From Equation (2.5), Young's relaxation modulus, $E(t)$ was obtained in the form of the generalized Maxwell model given as,

$$E(t) = E_\infty + \sum_{i=1}^{N} E_i e^{-t/\lambda_i} \tag{2.6}$$

where $E_\infty$ and $E_i$ ($i$=1,…$N$) are relaxation coefficients, and $\lambda_i$ ($i$=1,…$N$) are relaxation times, respectively. For a linearly viscoelastic material under uniaxial stress state, the uniaxial stress $\sigma(t)$ can be calculated from the applied strain history $\varepsilon(t)$, using the Boltzmann superposition principle,

$$\sigma(t) = \int_o^t E(t-\xi)\frac{d\varepsilon(\xi)}{d\xi}d\xi \tag{2.7}$$

For a linearly viscoelastic material, the fundamental viscoelastic functions in the time domain are relaxation and creep functions. Young's modulus at a given strain rate can be calculated from a viscoelastic function. In engineering applications, the linearly viscoelastic material is often modeled as a linearly elastic material, in which Young's modulus and Poisson's ratio are used as input. In this paper, Young's modulus at a given strain rate is calculated from the Young's relaxation function. Under a constant strain rate $\varepsilon(t) = \dot{\varepsilon}_0 t$, where $\dot{\varepsilon}_0$ is the constant strain rate, Equation (2.6) becomes [58],

$$\overline{E}(\dot{\varepsilon}_0) = \frac{\sigma(t)}{\varepsilon(t)} = \frac{1}{t-t_0}\int_{t_0}^{t} E(\xi)d\xi = \overline{E}(t) \tag{2.8}$$

where $\bar{E}(\dot{\varepsilon}_0)$ is the Young's modulus at strain rate $\dot{\varepsilon}_0$, and $\bar{E}(t)$ is the average Young's relaxation modulus from time $t_0$ to $t$. Equation (2.8) indicates that the Young's modulus at a given strain rate is equal to the time-average Young's relaxation modulus. At constant strain rate $\varepsilon(t) = \dot{\varepsilon}_0 t$, substituting relaxation modulus in Equation (2.6) into Equation (2.8) yields,

$$\overline{E}(\dot{\varepsilon}_0) = E_\infty + \sum_{i=1}^{n} E_i \frac{\lambda_i \dot{\varepsilon}_0}{\varepsilon}[1 - e^{\varepsilon/\lambda_i \dot{\varepsilon}_0}] \tag{2.9}$$

The time-average Young's modulus at a given strain rate is thus determined.

We re-evaluated the data shown in Figure 2.6, and present the Young's modulus value as a function of strain rate in Table 2.1. We only fit the displacement up to 300 nm, corresponding to 1.2 % strain, below which the SU-8 micropillars of different diameters show linear behavior. As strain rate increases, the time-average Young's modulus increases.

Table 2.1. Young's modulus at a given strain rate determined by viscoelastic analysis on microcompression data: strain rate effect.

| Diameter (μm) | Young's modulus (GPa) | Strain Rate ($s^{-1}$) |
|---|---|---|
| 6 | $3.12 \pm 0.02$ | $3.2\times10^{-4}$ |
| 6 | $4.86 \pm 0.03$ | $2.1\times10^{-3}$ |
| 12 | $3.04 \pm 0.03$ | $1.5\times10^{-4}$ |
| 12 | $4.11 \pm 0.04$ | $1.2\times10^{-3}$ |
| 12 | $4.75 \pm 0.04$ | $9.1\times10^{-3}$ |
| 16 | $2.91 \pm 0.02$ | $8.3\times10^{-5}$ |
| 16 | $3.72 \pm 0.02$ | $6.8\times10^{-4}$ |
| 16 | $4.66 \pm 0.03$ | $5.3\times10^{-3}$ |

**Size Effect**

Numerous studies have shown size-dependent behavior at small scales for various materials [27-31, 43-49]. Size-effect has been reported for SU-8 thin film from nanoindentation experiments using a sharp indenter tip [26] and microtensile tests [15, 17]. Microcompression on a micropillar has been used extensively to investigate the size effect in plastic deformation. Those results show in general "smaller is stronger" [27-31, 43-49]. To investigate the size effect, a stress rate approximately 1.8 MPa/s was used for all diameters.

Engineering stress-strain relationships for micropillars with diameters of 6, 8, 10, 12, 14, 16, and 18 μm are plotted in Figure 2.7. The engineering stress-strain curves start with linear elastic behavior, followed by yielding. After around 2.5% strain, all the samples display large strain bursts and no work-hardening was observed. Since the experiments were conducted under load-

control, the strain bursts may suggest the existence of a relatively strong strain softening after yielding [30]. The inset of Figure 2.7 shows that the time-average Young's modulus at a given strain rate decreases from 4.42 GPa to 3.73 GPa, as the diameter increases from 6 μm to 18 μm. The approximate strain rate is shown in Table 2.2, they are generally in the neighborhood of $10^{-3}$ $s^{-1}$. The average value is 4.1 GPa, which is in a good agreement with data obtained by García et al. [59], who reported Young's modulus of 3.7 GPa for a SU-8 micropillar with 40 μm diameter.

Table 2.2. Young's modulus at a given strain rate determined by viscoelastic analysis on microcompression data: size effect.

| Diameter (μm) | Young's modulus (GPa) | Strain Rate ($s^{-1}$) |
|---|---|---|
| 6 | $4.42 \pm 0.03$ | $7.6\times10^{-4}$ |
| 8 | $4.28 \pm 0.05$ | $8.4\times10^{-4}$ |
| 10 | $4.19 \pm 0.05$ | $7.8\times10^{-4}$ |
| 12 | $4.18 \pm 0.04$ | $8.0\times10^{-4}$ |
| 14 | $4.09 \pm 0.02$ | $9.6\times10^{-4}$ |
| 16 | $3.81 \pm 0.02$ | $1.04\times10^{-3}$ |
| 18 | $3.73 \pm 0.03$ | $1.1\times10^{-3}$ |

The yield strength as a function of size shows "the larger the stronger" phenomenon. Such behavior has been observed in nanocrystalline metals, for example, Jang and Greer [60] performed in-situ compression experiments on 60 nm nanocrystalline Ni-W nanopillars and discovered that their strength decreases by 42% as pillar diameter changes from 1.6 μm down to 100 nm. However, not only because such length scale was not reached in this study, but also, unlike crystalline materials, there is no intrinsic structural length scale in the pure SU-8 epoxy that could influence the yield strength at the microscale. The underlying mechanisms governing this behavior are not clear. Availability of the weak bonds, which affect the yielding in glassy polymers [61] may be different.

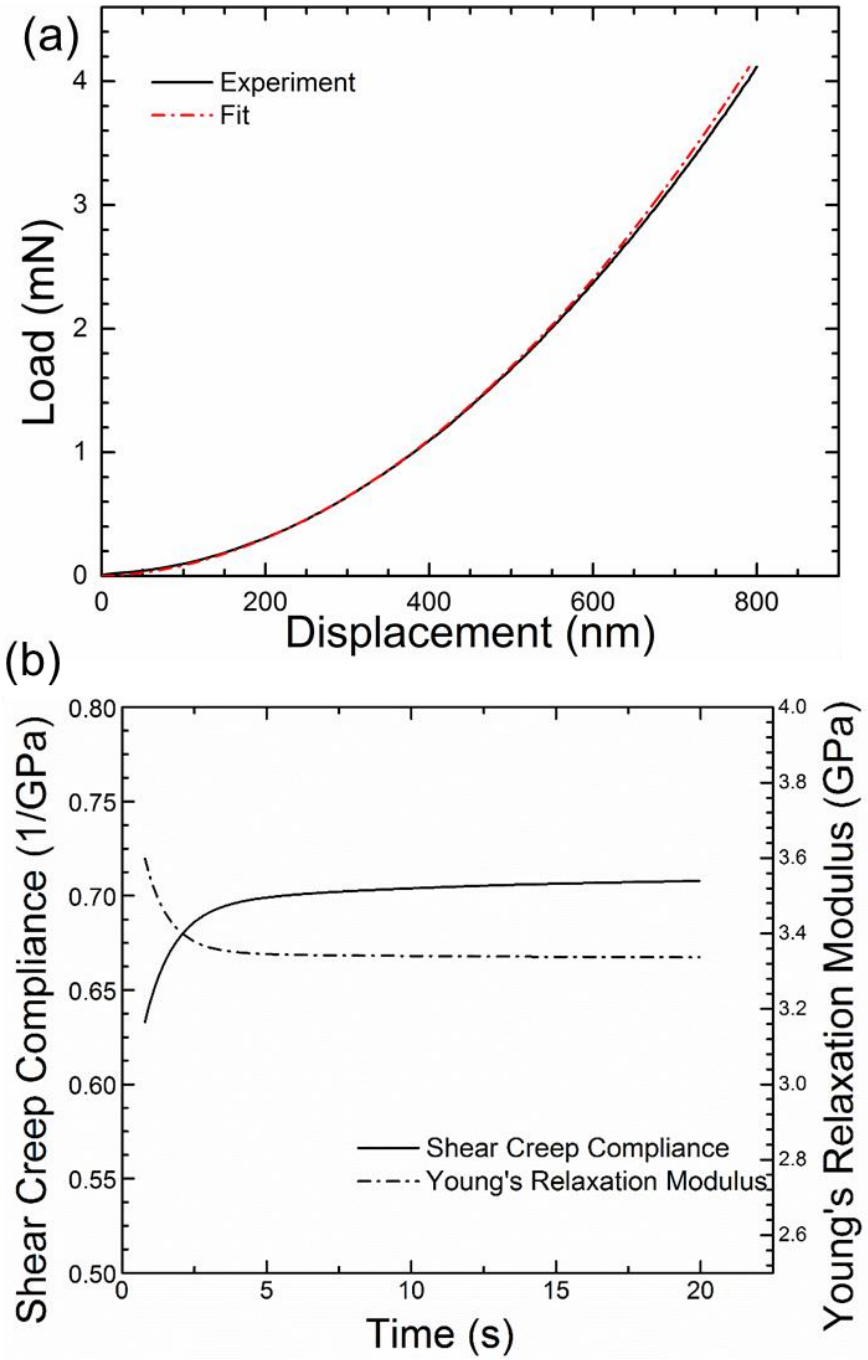


Figure 2.7. Engineering stress-strain curves for SU-8 micropillars with different diameters. Each curve is the average data from 10 independent microcompression experiments, the differences in results obtained from different experiments are in general within 1%; the error bars are not plotted since they are nearly invisible. The inset shows the Young's modulus and yield strength as a function of micropillar diameter.

In addition, failure stress in amorphous materials depends strongly on the local strength, which in turn depends on morphology and topography [62]. In this case, in analysis, the choice of reference diameter could affect the result in the calculation of yield strength. As stated in 2.3.1, while one can determine the Young's modulus with accuracy, the yield strength can be underestimated when the mid-surface diameter is used for calculation of stress. The degree of under-estimation is larger for a smaller diameter, as shown in Figure 2.5. A similar trend is also shown in Figure 2.6. The compressive yield strength ($108.4 \pm 10.0$ MPa) determined from compression of a micropillar is slightly higher than the value obtained from tensile tests (nearly 60~70 MPa [16, 17]). These results are consistent with data reported for in polymers. For the sizes of micropillars investigated in this study, the yield strength does not show size effect.

### 2.3.2 Viscoelastic Analysis of Nanoindentation on SU-8 Thin Film

Nanoindentation with a Berkovich tip was made on 25 μm thick SU-8 film supported on silicon wafer substrate. The nanoindentation load-displacement curves are shown in Figure 2.8. At the same loading rate, the nanoindentation load-displacement curves are consistent. The initial part of the unloading curves does not show "noise" or negative unloading slope. The Young's modulus values calculated by the Oliver-Pharr method were $5.88 \pm 0.02$, $5.87 \pm 0.02$, and $5.97 \pm 0.03$ GPa, at loading rates 0.25, 1.0 and 2.5 mN/s, respectively. These Young's modulus values are within the range of 5~7.4 GPa reported in literature from nanoindentation measurements on SU-8 thin film in the literature [18-24]. SU-8, however, is a polymer, exhibiting viscoelastic behavior, so that viscoelastic nanoindentation analysis is necessary to determine accurately the Young's modulus. This will be described in this section.

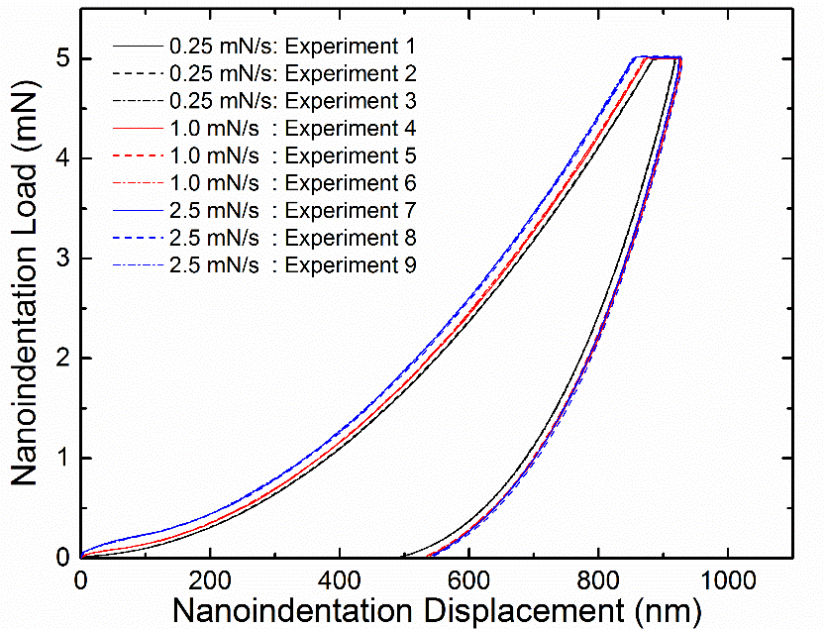


Figure 2.8. Nanoindentation load-displacement curves at three different loading rates.

Lu et al. [36] developed a method using viscoelastic analysis to extract the shear creep compliance of a viscoelastic material from nanoindentation load-displacement curve. In this section, we apply that approach to calculate the Young's modulus of the SU-8 thin film.

The Berkovich indenter tip is modeled as an axisymmetric conical indenter with a half-cone angle of 70.3°. Under a constant rate loading history, $P(t) = \dot{P}_o t H(t)$, where $\dot{P}_o$ is the constant loading rate, $t$ is elapsed time, and $H(t)$ is the Heaviside unit step function, considering nanoindentation by a rigid conical indenter tip into a half-space composed of a linearly viscoelastic material, the nanoindentation displacement $h(t)$ is given by,

$$h^2(t) = \frac{1}{4}\pi(1-\nu)\tan\alpha \times \left[ (J_0 + \sum_{i=1}^{N} J_i) P(t) - \sum_{i=1}^{N} J_i (\dot{P}_o \tau_i)(1 - e^{-P(t)/(\dot{P}_0 \tau_i)}) \right] \quad (2.10)$$

where $\alpha$ = 19.7°, and $\nu$ is the Poisson's ratio, which is taken as 0.22 [18]. $J_0$ and $J_i$ ($i$=1,…$N$) are shear creep coefficients and $\tau_i$ ($i$=1,…$N$) are retardation times.

In the generalized Kelvin model, $J(t)$ is given as a Prony series,

$$J(t) = J_0 + \sum_{i=1}^{N} J_i(1-e^{-t/\tau_i}) \tag{2.11}$$

The Volterra equation is now given as,

$$\int_0^t E(\xi)J(t-\xi)d\xi = 2(1+\nu)t \tag{2.12}$$

It is noted that the choice of the fitting parameters is not unique and that different parameter sets can provide the same shear creep compliance. Knauss and Zhao [63] indicated that the choice of the retardation times is not subject to single stringent criterion and suggested that allowing for one retardation time per decade is usually satisfactory. In this paper, five predetermined retardation times were selected, they are 0.01 s, 0.1 s, 1 s, 10 s, and 100 s, which will encompass the experimental time frame to provide a smooth creep function. The corresponding compliance parameters $J_i$ were obtained from this curve fitting process. The best-fit parameters were then used in Equation (2.11) and Equation (2.12) to obtain the Young's relaxation modulus. Finally Equation (2.8) and Equation (2.9) were used to calculated the Young's modulus at a given strain rate.

In Figure 2.9, one set of nanoindentation data was used to illustrate the viscoelastic analysis approach. Both the experimental and fitted load-displacement curves are shown in Figure 2.9(a). The least squares correlation coefficient is $9.9 \times 10^{-5}$, indicating a good correlation. The parameters used in Equation (2.10) to obtain the fitted curve as shown in Figure 2.9(a) were used in Equation (2.11) to calculate the shear creep compliance, given as,

$$\begin{aligned} J(t) = {} & 0.1878 + 0.1872(1-e^{\frac{-t}{0.01}}) + 0.1823(1-e^{\frac{-t}{0.1}}) + 0.1361(1-e^{-t}) \\ & + 0.01664(1-e^{\frac{-t}{10}}) + 3.143\times10^{-4}(1-e^{\frac{-t}{100}}) \qquad 1/\text{GPa} \end{aligned} \tag{2.13}$$

where $t$ is time in seconds. By implementing the approach developed by Luk-Cyr *et al.* [57], the Young's relaxation function was determined as,

$$E(t) = 3.345 + 6.917e^{-205.4t} + 1.898e^{-14.63t} + 0.8917e^{-1.273t} + 4.585\times10^{-31}e^{-t} + 0.08929e^{-0.1027t} \quad \text{GPa} \tag{2.14}$$

The Young's relaxation function and shear creep compliance are shown in Figure 2.9(b). Subsequently the Young's modulus at a given strain rate $9.3\times10^{-4}$ $s^{-1}$ was calculated as 3.426 GPa. In this paper the nanoindentation is conducted under a constant loading rate. Time-average Young's relaxation modulus values were calculated via Equation (2.8), since it is equivalent to Young's modulus at a given strain rate. The nominal strain rate was determined from Equation (2.9) up to compressive strain $\varepsilon$=1%. For the loading rates 0.25 mN/s, 1 mN/s, and 2.5 mN/s, the time-average Young's modulus determined are at strain rates in the neighborhood of $1\times10^{-3}$, $4\times10^{-3}$, and $8\times10^{-3}$, respectively.

Following these procedures, nanoindentation data at three different loading rates, 0.25 mN/s, 1 mN/s, and 2.5 mN/s was analyzed. The time-average Young's modulus at each loading rate was determined to be $3.48\pm0.05$, $3.51\pm0.02$ and $3.65\pm0.02$ GPa, respectively. The time-average Young's modulus shows a slight increasing trend as the strain/loading rate increases, which is typical for a viscoelastic material. The time-average Young's modulus values determined by viscoelastic analysis of nanoindentation on SU-8 thin film agree very well with that determined by microcompression conducted on SU-8 micropillars.

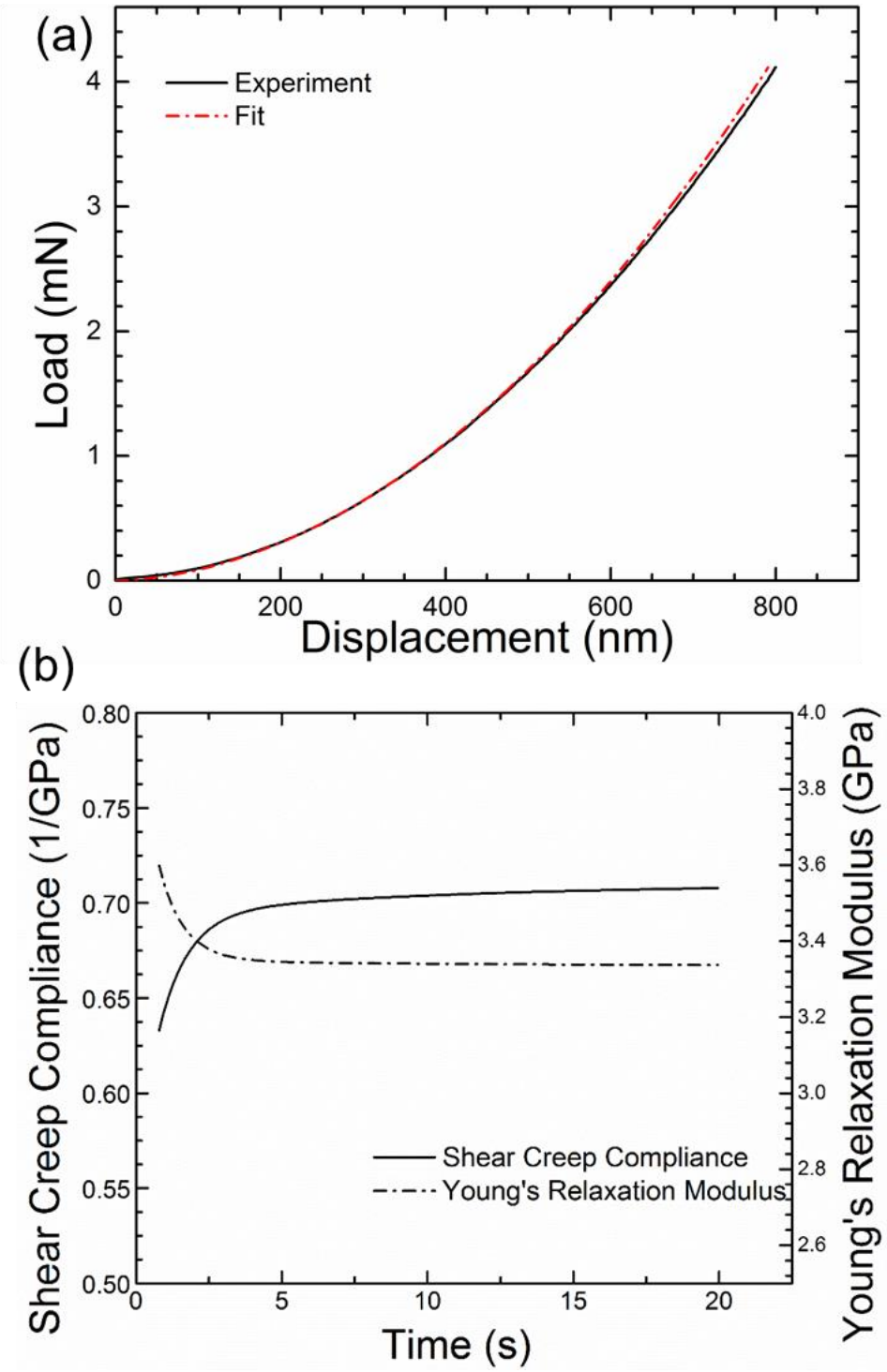


Figure 2.9. Typical nanoindentation results on SU-8 thin film, at a loading rate 0.25 mN/s (a) experimental and fitted nanoindentation load - displacement curves, (b) shear creep compliance and Young's relaxation modulus.

Table 2.3. Comparison of Young's modulus obtained from different experiments and analysis. "---" indicates that data was not available from literature.

| References | Method | Strain/Loading Rate | Young's Modulus (GPa) |
|---|---|---|---|
| Namazu *et al.* [15] | Tensile Tests | $1\times10^{-4}$ $s^{-1}$ | 3.56 |
| Robin *et al.* [17] | Tensile Tests | 0.001 $s^{-1}$ | 3.55 |
| Robin *et al.* [17] | Tensile Tests | 0.01 $s^{-1}$ | 3.96 |
| Wouters *et al.* [23] | Tensile Tests | $1.5\times10^{-4}$ $s^{-1}$ | 2.2 |
| Wouters *et al.* [23] | Nanoindentation (Oliver-Pharr Method) | --- | 7.4 |
| Chiou *et al.* [18] | Nanoindentation (Oliver-Pharr Method) | --- | 5.2 |
| Al-Halhouli *et al.* [19] | Nanoindentation (Oliver-Pharr Method) | 0.3 mN/s | 5.6 |
| Seena *et al.* [20] | Nanoindentation (Oliver-Pharr Method) | --- | 6.0 |
| Kandpal *et al.* [21] | Nanoindentation (Oliver-Pharr Method) | --- | 8.1 |
| Kang *et al.* [22] | Nanoindentation (Oliver-Pharr Method) | --- | 5.4 |
| Le Rouzic *et al.* [24] | Nanoindentation (Oliver-Pharr Method) | --- | 6.1 |
| Our Results | Micropillar Compressions | | 4.1 |
| Oliver-Pharr Method | Nanoindentation | 0.25 mN/s | $5.88 \pm 0.02$ |
| Oliver-Pharr Method | Nanoindentation | 1.0 mN/s | $5.87 \pm 0.02$ |
| Oliver-Pharr Method | Nanoindentation | 2.5 mN/s | $5.97 \pm 0.03$ |
| Viscoelastic Analysis | Nanoindentation | 0.25 mN/s | $3.48\pm0.05$ |
| Viscoelastic Analysis | Nanoindentation | 1.0 mN/s | $3.51\pm0.02$ |
| Viscoelastic Analysis | Nanoindentation | 2.5 mN/s | $3.65\pm0.02$ |

In addition, they are consistent with the data reported in literature [15, 17, 23], obtained from uniaxial tensile experiments. It is noted that the Young's modulus obtained from the

Oliver-Pharr method give values around 6.0 GPa, these Young's modulus values overestimated the Young's modulus of SU-8 thin film. The comparison is shown in Table 2.3. Robin *et al.* [17] determined that the Young's modulus values were 3.55 and 3.96 GPa for 0.001 $s^{-1}$ and 0.01 $s^{-1}$, respectively. Their data agree reasonably well with the Young's modulus determined by viscoelastic nanoindentation, at strain rates 0.001 $s^{-1}$ and 0.008 $s^{-1}$ (3.48 and 3.65 GPa, respectively). Thus, this study indicates that nanoidentation is still an effective tool to determine the mechanical properties of SU-8 thin film, provided that appropriate viscoelastic analysis is used.

## 2.4 Conclusion

Mechanical properties of SU-8 were measured by compression of micropillars and nanoindentation on a film supported by a substrate. Microcompression experiments were conducted on different sizes of SU-8 micropillars at different loading rates. It was confirmed that SU-8 exhibits viscoelastic behavior at room temperature, and its mechanical properties are rate-dependent. The mechanical properties of SU-8, including the Young's modulus and yield strength are generally higher at higher loading rate. Young's modulus and yield strength were also determined as a function of micropillar diameter. Young's modulus shows a decreasing trend, from 4.4 GPa to 3.7 GPa, as the diameter increases from 6 μm to 18 μm. The yield strength shows an increasing trend as sample size increases. Further investigations are needed to obtain in-depth understanding to explain the observed size-dependency. Since SU-8 is a viscoelastic material, an appropriate analysis of nanoindentation load-displacement data was conducted. Time-average Young's modulus at a given strain rate determined by our approach agrees very well with literature values obtained from tensile or bending tests, and also correlates

reasonably well with data from microcompression. Considering the ease of preparing SU-8 thin film, nanoindentation is still a very effective technique for characterizing mechanical properties at small scales. In this case, viscoelastic nanoindentation analysis is needed to extract the mechanical properties.

## 2.5 References


1. LaBianca, Nancy C., and Jeffrey D. Gelorme. "High-aspect-ratio resist for thick-film applications." In *SPIE's 1995 Symposium on Microlithography*, pp. 846-852. International Society for Optics and Photonics, 1995.

2. Lorenz, Hubert, M. Despont, P. Vettiger, and Philippe Renaud. "Fabrication of photoplastic high-aspect ratio microparts and micromolds using SU-8 UV resist." *Microsystem Technologies* 4, no. 3 (1998): 143-146.

3. Shew, B. Y., C. H. Kuo, Y. C. Huang, and Y. H. Tsai. "UV-LIGA interferometer biosensor based on the SU-8 optical waveguide." *Sensors and Actuators A: Physical* 120, no. 2 (2005): 383-389.

4. Carlier, J., S. Arscott, V. Thomy, J. C. Fourrier, F. Caron, J. C. Camart, C. Druon, and P. Tabourier. "Integrated microfluidics based on multi-layered SU-8 for mass spectrometry analysis." *Journal of micromechanics and Microengineering* 14, no. 4 (2004): 619.

5. Genolet, Grégoire, Jürgen Brugger, Michel Despont, Ute Drechsler, Peter Vettiger, N. F. De Rooij, and Dario Anselmetti. "Soft, entirely photoplastic probes for scanning force microscopy." *Review of scientific instruments* 70, no. 5 (1999): 2398-2401.

6. Cho, Sung-Hoon, Hong Meng Lu, Lawrence Cauller, Mario I. Romero-Ortega, Jeong-Bong Lee, and Gareth A. Hughes. "Biocompatible SU-8-based microprobes for recording neural spike signals from regenerated peripheral nerve fibers." *IEEE Sensors Journal* 8, no. 11 (2008): 1830-1836.

7. Lorenz, Hubert, M. Laudon, and Philippe Renaud. "Mechanical characterization of a new high-aspect-ratio near UV-photoresist." *Microelectronic Engineering* 41 (1998): 371-374.

8. Lorenz, Hubert, M. Despont, N. Fahrni, J. Brugger, P. Vettiger, and Philippe Renaud. "High-aspect-ratio, ultrathick, negative-tone near-UV photoresist and its applications for MEMS." *Sensors and Actuators A: Physical* 64, no. 1 (1998): 33-39.

9. Xiang, Zhuolin, Hao Wang, Aakanksha Pant, Giorgia Pastorin, and Chengkuo Lee. "Development of vertical SU-8 microneedles for transdermal drug delivery by double drawing lithography technology." *Biomicrofluidics* 7, no. 6 (2013): 066501.

10. Cho, Sung-Hoon, Ning Xue, Lawrence Cauller, Will Rosellini, and Jeong-Bong Lee. "A SU-8-based fully integrated biocompatible inductively powered wireless neurostimulator." *Journal of Microelectromechanical Systems* 22, no. 1 (2013): 170-176.

11. Xue, Ning, Sung-Pil Chang, and Jeong-Bong Lee. "A SU-8-based microfabricated implantable inductively coupled passive RF wireless intraocular pressure sensor." *Journal of Microelectromechanical Systems* 21, no. 6 (2012): 1338-1346.

12. Reddy, C. Vijaya Bhaskar, Mrunal A. Khaderbad, Sahir Gandhi, Manoj Kandpal, Sheetal Patil, K. Narasaiah Chetty, K. Govinda Rajulu, P. C. K. Chary, M. Ravikanth, and V. Ramgopal Rao. "Piezoresistive SU-8 cantilever with Fe (III) porphyrin coating for CO sensing." *IEEE Transactions on Nanotechnology* 11, no. 4 (2012): 701-706.

13. Kim, Jong Yun, Young-Soo Choi, Bong-Kee Lee, and Dong-Weon Lee. "Surface-patterned SU-8 cantilever arrays for preliminary screening of cardiac toxicity." *Biosensors and Bioelectronics* 80 (2016): 456-462.

14. Lorenz, Hubert, M. Despont, N. Fahrni, N. LaBianca, Philippe Renaud, and P. Vettiger. "SU-8: a low-cost negative resist for MEMS." *Journal of Micromechanics and Microengineering* 7, no. 3 (1997): 121.

15. Namazu, T., S. Inoue, K. Takio, T. Fujita, K. Maenaka, and K. Koterazawa. "Visco-elastic properties of micron-thick SU-8 polymers measured by two different types of uniaxial tensile tests." In *18th IEEE International Conference on Micro Electro Mechanical Systems, 2005. MEMS 2005.*, pp. 447-450. IEEE, 2005.

16. Robin, C. J., Aakansha Vishnoi, and Krishna N. Jonnalagadda. "Mechanical behavior and anisotropy of spin-coated SU-8 thin films for MEMS." *Journal of Microelectromechanical Systems* 23, no. 1 (2014): 168-180.

17. Robin, C. J., and K. N. Jonnalagadda. "Effect of size and moisture on the mechanical behavior of SU-8 thin films." *Journal of Micromechanics and Microengineering* 26, no. 2 (2016): 025020.

18. Chiou, De-Yi, Mu-Yueh Chen, Ming-Wei Chang, and Hsu-Cheng Deng. "Characterization and optimization design of the polymer-based capacitive micro-arrayed ultrasonic transducer." *Japanese Journal of Applied Physics* 46, no. 11R (2007): 7496.

19. Al-Halhouli, A. T., I. Kampen, T. Krah, and S. Büttgenbach. "Nanoindentation testing of SU-8 photoresist mechanical properties." *Microelectronic Engineering* 85, no. 5 (2008): 942-944.

20. Seena, V., Avil Fernandes, Prita Pant, Soumyo Mukherji, and V. Ramgopal Rao. "Polymer nanocomposite nanomechanical cantilever sensors: material characterization, device development and application in explosive vapour detection." *Nanotechnology* 22, no. 29 (2011): 295501.

21. Kandpal, Manoj, Chandrashekhar Sharan, Pankaj Poddar, K. Prashanthi, Prakash R. Apte, and V. Ramgopal Rao. "Photopatternable nano-composite (SU-8/ZnO) thin films for piezo-electric applications." *Applied Physics Letters* 101, no. 10 (2012): 104102.

22. Kang, Yuji, Makoto Okada, Yasuki Nakai, Yuichi Haruyama, Kazuhiro Kanda, and Shinji Matsui. "Mechanical characteristics of imprinted nanostructures fabricated with a poly (dimethylsiloxane) mold." *Journal of Vacuum Science & Technology B* 29, no. 6 (2011): 06FC10.

23. Wouters, Kristof, Pieter Gijsenbergh, and Robert Puers. "Comparison of methods for the mechanical characterization of polymers for MEMS applications." *Journal of Micromechanics and Microengineering* 21, no. 11 (2011): 115027.

24. Le Rouzic, Julian, Patrick Delobelle, Bernard Cretin, Pascal Vairac, and Fabien Amiot. "Simultaneous measurement of Young's modulus and Poisson's ratio at microscale with two-modes scanning microdeformation microscopy." *Materials Letters* 68 (2012): 370-373.

25. Feng, Ru, and Richard J. Farris. "Influence of processing conditions on the thermal and mechanical properties of SU8 negative photoresist coatings." *Journal of Micromechanics and Microengineering* 13, no. 1 (2002): 80.

26. Khoo, Hwa Seng, Kuo-Kang Liu, and Fan-Gang Tseng. "Mechanical strength and interfacial failure analysis of cantilevered SU-8 microposts." *Journal of micromechanics and microengineering* 13, no. 6 (2003): 822.

27. Uchic, Michael D., Dennis M. Dimiduk, Jeffrey N. Florando, and William D. Nix. "Sample dimensions influence strength and crystal plasticity." *Science* 305, no. 5686 (2004): 986-989.

28. Uchic, Michael D., Paul A. Shade, and Dennis M. Dimiduk. "Plasticity of micrometer-scale single crystals in compression." *Annual Review of Materials Research* 39 (2009): 361-386.

29. Wang, S., Y. Yang, L. M. Zhou, and Y-W. Mai. "Size effect in microcompression of epoxy micropillars." *Journal of Materials Science* 47, no. 16 (2012): 6047-6055.

30. Bei, Hongbin, Sanghoon Shim, Easo P. George, Michael K. Miller, E. G. Herbert, and George Mathews Pharr. "Compressive strengths of molybdenum alloy micro-pillars prepared using a new technique." *Scripta Materialia* 57, no. 5 (2007): 397-400.

31. Shin, C., H-H. Jin, H. Sung, D-J. Kim, Y. S. Choi, and K. Oh. "Evaluation of irradiation effects on fracture strength of silicon carbide using micropillar compression tests." *Experimental Mechanics* 53, no. 4 (2013): 687-697.

32. Oliver, Warren Carl, and George Mathews Pharr. "An improved technique for determining hardness and elastic modulus using load and displacement sensing indentation experiments." *Journal of materials research* 7, no. 06 (1992): 1564-1583.

33. Oliver, Warren C., and Georges M. Pharr. "Measurement of hardness and elastic modulus by instrumented indentation: Advances in understanding and refinements to methodology." *Journal of materials research* 19, no. 01 (2004): 3-20.

34. Briscoe, B. J., L. Fiori, and E. Pelillo. "Nano-indentation of polymeric surfaces." *Journal of Physics D: Applied Physics* 31, no. 19 (1998): 2395.

35. VanLandingham, Mark R. *Review of instrumented indentation*. National Inst Of Standards and Technology Gaithersburg MD, 2003.

36. Lu, H., B. Wang, J. Ma, G. Huang, and H. Viswanathan. "Measurement of creep compliance of solid polymers by nanoindentation." *Mechanics of time-dependent materials* 7, no. 3-4 (2003): 189-207.

37. Huang, G., and H. Lu. "Measurements of two independent viscoelastic functions by nanoindentation." *Experimental Mechanics* 47, no. 1 (2007): 87-98.

38. Cheng, Yang-Tse, Che-Min Cheng, and Wangyang Ni. "Methods of obtaining instantaneous modulus of viscoelastic solids using displacement-controlled instrumented indentation with axisymmetric indenters of arbitrary smooth profiles." *Materials Science and Engineering: A* 423, no. 1 (2006): 2-7.

39. Lu, Hongbing, Gang Huang, Bo Wang, Arif Mamedov, and Sachin Gupta. "Characterization of the linear viscoelastic behavior of single-wall carbon nanotube/polyelectrolyte multilayer nanocomposite film using nanoindentation." *Thin Solid Films* 500, no. 1 (2006): 197-202.

40. Xu, T., Y. Du, H. Luo, G-H. Kim, Z. Xu, M. Minary-Jolandan, L. Stark, T. Baughn, and H. Lu. "Measurement of Temperature-Dependent Young's Modulus at a Strain Rate for a Molding Compound by Nanoindentation." *Experimental Mechanics* (2016): 1-13.

41. Daphalapurkar, Nitin P., Chenkai Dai, Rong Z. Gan, and Hongbing Lu. "Characterization of the linearly viscoelastic behavior of human tympanic membrane by nanoindentation." *Journal of the mechanical behavior of biomedical materials* 2, no. 1 (2009): 82-92.

42. Sadr, Alireza, Yasushi Shimada, Hongbing Lu, and Junji Tagami. "The viscoelastic behavior of dental adhesives: a nanoindentation study." *Dental Materials* 25, no. 1 (2009): 13-19.

43. Uchic, Michael D., and Dennis M. Dimiduk. "A methodology to investigate size scale effects in crystalline plasticity using uniaxial compression testing." *Materials Science and Engineering: A* 400 (2005): 268-278.

44. Zhang, Haitao, Brian E. Schuster, Qiuming Wei, and Kaliat T. Ramesh. "The design of accurate micro-compression experiments." *Scripta Materialia* 54, no. 2 (2006): 181-186.

45. Yang, Y., J. C. Ye, J. Lu, F. X. Liu, and P. K. Liaw. "Effects of specimen geometry and base material on the mechanical behavior of focused-ion-beam-fabricated metallic-glass micropillars." *Acta Materialia* 57, no. 5 (2009): 1613-1623.

46. Frick, C. P., B. G. Clark, S. Orso, A. S. Schneider, and E. Arzt. "Size effect on strength and strain hardening of small-scale [111] nickel compression pillars." *Materials Science and Engineering: A* 489, no. 1 (2008): 319-329.

47. Shan, Z. W., Raja K. Mishra, SA Syed Asif, Oden L. Warren, and Andrew M. Minor. "Mechanical annealing and source-limited deformation in submicrometre-diameter Ni crystals." *Nature materials* 7, no. 2 (2008): 115-119.

48. Gram, Michael D., John S. Carpenter, and Peter M. Anderson. "An indentation-based method to determine constituent strengths within nanolayered composites." *Acta Materialia* 92 (2015): 255-264.

49. Schwiedrzik, Jakob, Rejin Raghavan, Alexander Bürki, Victor LeNader, Uwe Wolfram, Johann Michler, and Philippe Zysset. "In situ micropillar compression reveals superior strength and ductility but an absence of damage in lamellar bone." *Nature materials* 13, no. 7 (2014): 740-747.

50. ABAQUS, V. "6.14 documentation." *Dassault Systemes Simulia Corporation* (2014).

51. ASTM. *Standard Test Method for Compressive Properties of Rigid Plastics* ASTM D695-15, 2015.

52. Du, Ping, Chen Cheng, Hongbing Lu, and Xin Zhang. "Investigation of cellular contraction forces in the frequency domain using a PDMS micropillar-based force transducer." *Journal of Microelectromechanical Systems* 22, no. 1 (2013): 44-53.

53. Du, Ping, I-Kuan Lin, Hongbing Lu, and Xin Zhang. "Extension of the beam theory for polymer bio-transducers with low aspect ratios and viscoelastic characteristics." *Journal of Micromechanics and Microengineering* 20, no. 9 (2010): 095016.

54. Ferry, John D. *Viscoelastic properties of polymers*. John Wiley & Sons, 1980.

55. Emri, Igor, and N. W. Tschoegl. "Generating line spectra from experimental responses. Part I: Relaxation modulus and creep compliance." *Rheologica Acta* 32, no. 3 (1993): 311-322.

56. Tschoegl, N. W., and I. Emri. "Generating line spectra from experimental responses. III. Interconversion between relaxation and retardation behavior." *International Journal of Polymeric Materials* 18, no. 1-2 (1992): 117-127.

57. Luk-Cyr, Jacques, Thibaut Crochon, Chun Li, and Martin Lévesque. "Interconversion of linearly viscoelastic material functions expressed as Prony series: a closure." *Mechanics of Time-Dependent Materials* 17, no. 1 (2013): 53-82.

58. Luo, Huiyang, Yanli Zhang, Bo Wang, and Hongbing Lu. "Characterization of the compressive behavior of glass fiber reinforced polyurethane foam at different strain rates." *Journal of Offshore Mechanics and Arctic Engineering* 132, no. 2 (2010): 021301.

59. García, Enrique J., A. John Hart, Brian L. Wardle, and Alexander H. Slocum. "Fabrication and Nanocompression Testing of Aligned Carbon-Nanotube–Polymer Nanocomposites." *Advanced materials* 19, no. 16 (2007): 2151-2156.

60. Jang, Dongchan, and Julia R. Greer. "Size-induced weakening and grain boundary-assisted deformation in 60 nm grained Ni nanopillars." *Scripta Materialia* 64, no. 1 (2011): 77-80.

61. Stachurski, Z. H. "Deformation mechanisms and yield strength in amorphous polymers." *Progress in polymer science* 22, no. 3 (1997): 407-474.

62. Greer, Julia R., and Jeff Th M. De Hosson. "Plasticity in small-sized metallic systems: Intrinsic versus extrinsic size effect." *Progress in Materials Science* 56, no. 6 (2011): 654-724.

63. Knauss, Wolfgang G., and J. Zhao. "Improved relaxation time coverage in ramp-strain histories." *Mechanics of Time-Dependent Materials* 11, no. 3-4 (2007): 199-216.

# CHAPTER 3

# MEASUREMENT OF TEMPERATURE-DEPENDENT YOUNG'S MODULUS AT A STRAIN RATE FOR A MOLDING COMPOUND BY NANOINDENTATION†

## 3.1 Introduction

Typical integrated circuits (IC) are assembled from multiple components, including molding compound, die-attach adhesive, silicon dielectric, solder joints, and copper traces/pads. Each component has its own constitutive behavior when subjected to thermal cycling. In accelerated life testing for an IC under thermal cycling, the molding compound can play a significant role on the active device, wire bonds and package leads, and result in mechanical failure. The molding compound is made of assorted diameters of glass beads embedded in a polymer such as epoxy, and exhibits viscoelastic properties which depend on the processing conditions, geometry, confining conditions by neighboring components, as well as temperature. In order to mitigate failure in the package design and improve the life predication capability, the mechanical properties of all the components are required. Unfortunately, material properties are often difficult to obtain, particularly over the temperature range the IC may experience. Mechanical properties of the polymers, such as molding compounds rarely have sufficient properties since they generally exhibit viscoelastic characteristics. Accordingly, the effort presented will focus on the development of the temperature-dependent Young's modulus at a given strain rate of a heterogeneous molding compound [1-6].

---

† Reprinted with permission from "Xu, T., Y. Du, H. Luo, G-H. Kim, Z. Xu, M. Minary-Jolandan, L. Stark, T. Baughn, and H. Lu. "Measurement of Temperature-Dependent Young's Modulus at a Strain Rate for a Molding Compound by Nanoindentation." *Experimental Mechanics* (2016): 1-13." Published September 22, 2016. doi:10.1007/s11340-016-0205-7 

Moreover, molding compounds may exhibit viscoelastic behavior even at room temperature [1-8], and it is well known that the mechanical properties of polymers exhibit loading/thermal history and morphology which may depend on processing conditions. In addition, the viscoelastic properties depend on the confining conditions imposed from adjacent packaging materials and their corresponding coefficient of thermal expansion. Under confining pressure, the polymer could shift its viscoelastic properties towards glassy state [9].

The characterization of viscoelastic properties, such as the relaxation modulus is normally conducted using either relaxation or creep experiments in the time domain, or using dynamic mechanical analysis (DMA) in the frequency domain [10,11]. The viscoelastic properties for a molding compound on a production integrated circuit depend on the processing conditions where conventional tensile and compression experimental results from a bulk material may be not applicable. In recent years the nanoindentation technique, also known as depth-sensing indentation, is gradually becoming an effective technique for determining the local mechanical properties at the microscale and nanoscale. Methods for measuring the elastic-plastic properties, such as Young's modulus and hardness have been well established by Oliver and Pharr [12-13]. The wide acceptance of nanoindentation technique stems from improvements incorporated in the technique. For example, the need for the direct observation of the residual indentation impression is no longer required. Instead, the unloading curve is used to extract the elastic properties of an elastic-plastic material, namely, elastic modulus and hardness by calculating the area of the indent impression from the loading/unloading curves. This method is very well established and has been implemented in commercially instrumented nanoindenters for use on elastic-plastic materials, such as sand grains [14-16], glass bead [17], and metal-organic framework materials

[18]. Inverse methodologies, using numerical techniques, in combination with experimental results have been developed effectively to measure material properties and also stress-strain relationships [19-20].

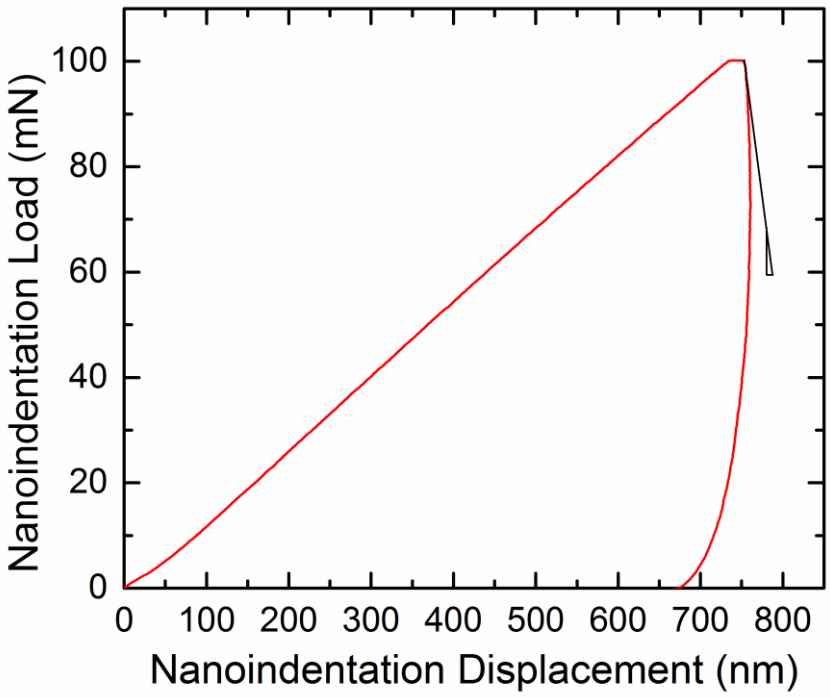


Figure 3.1. Nanoindentation load-displacement curve showing a negative slope at the initial unloading stage at a loading/unloading rate of 0.2 mN/s.

The Oliver-Pharr method, however, experiences difficulties to measure the mechanical properties of viscoelastic materials. One well-known phenomenon is the formation of unloading "nose" or negative stiffness during unloading that often occurs during slow loading-unloading history in nanoindentation on a viscoelastic material [21-22]. For nanoindentation conducted on polymers, a negative slope of the initial unloading curve was formed as shown in Figure 3.1. In which case, viscoelastic analysis is needed to extract the mechanical property data. In recent years, numerous methods have been developed to measure linearly viscoelastic functions of polymers, composites, biomedical materials, and other time-dependent materials, in both time

and frequency domain. Lu et al. [23] developed to measure the creep compliance of polymers using either a Berkovich indenter or a spherical indenter. Huang et al. [24] measured the viscoelastic functions in the frequency-domain using a spherical indenter. Huang and Lu [25] devised a method to measure two independent viscoelastic functions using both axisymmetric and asymmetric nanoindenter tips allowing separation of two independent viscoelastic functions. Cheng et al. [26] derived analytical solutions for linearly viscoelastic deformation under a flat-punch indentation and provided a method to measure viscoelastic properties described by a three-element viscoelastic model. Lu et al. [27] developed methods to measure general linearly viscoelastic functions in both time and frequency domains using flat punch nanoindentation. Cheng and Cheng [28] derived an expression of unloading stiffness for a linearly viscoelastic solid under nanoindentation. Cheng et al [29] derived a relationship between the initial unloading slope, contact depth, and the instantaneous relaxation modulus for displacement-controlled indentation in a linearly viscoelastic solid by a rigid indenter with an arbitrary axisymmetric smooth profile. Cao [30] developed a nanoindentation method to determine the exponent of a viscoplastic material in which stress follows a power law relationship with the strain rate. Kucuk et al. [31] modeled spherical nanoindentation on poly(methyl methacrylate) (PMMA) using the nonlinear Burgers model. By inverse calculations from the finite element simulations, they were able to capture the unloading "nose". Nanoindentation has been used for the characterization of the viscoelastic behavior of a wide range of materials. Lu et al [32] measured both the in-plane and the through-thickness linearly viscoelastic properties of the single-wall carbon nanotubes (SWNT)/polyelectrolyte multilayer nanocomposite film. Using AFM nanoindentation measurement, Francius et al. [33] measured the viscoelastic properties of polyelectrolyte

multilayer films represented by a standard linear solid model. Sadr et al. [34] measured the properties of dental compounds and found that the Young's modulus was significantly over-estimated using nanoindentation technique without consideration of viscoelastic effects. Huang et al. [35] and Daphalapurkar et al. [36] used nanoindentation to measure viscoelastic properties of a human tympanic membrane. These techniques can be used to measure viscoelastic properties through theoretical or numerical analysis.

Specifically for molding compounds, measurement results in the literature characterizing the mechanical behavior by the Oliver-Pharr method [1, 37] have shown to provide incorrect results. At elevated temperatures, the pronounced viscoelastic effects will exacerbate the inaccuracy of the measurements. Thus alternative viscoelastic measurement methods must be used in order to extract accurate temperature- and time-dependent properties of the molding compound. In addition, because the molding compound consists of assorted diameters of glass beads embedded in an epoxy, it is highly heterogeneous. To determine the material properties of a molding compound on a packaged IC, full-field deformation measurement techniques were used [38,39]. Digital Image Correlation (DIC) technique [40,41] was used in connection with numerical analysis to determine the material properties [38,39]. However, to the best of our knowledge, there is no published work to measure the mechanical properties of heterogeneous molding compounds at elevated temperatures by nanoindentation.

Thus, the purpose of this paper is to characterize the material behavior of a molding compound at various temperatures for use in structural analysis which takes material properties as a function of temperature, to improve the life prediction capability for integrated circuits subjected to thermal cycling. It is also important to understand the impact on the properties of a

material imposed by the constraints from the over molding materials and adjacent components. Based on these concerns the material testing is directed at measuring the Young's modulus at a given strain rate of a molding compound over temperature, *in-situ*, in an integrated circuit package. The material in test will also be subjected to the assembly process environment, which will provide more representative values during thermal cycling. At selected service temperatures, time dependent properties of the molding compound, in thin form, were measured by instrumented nanoindentation developed by Lu et al. [23]. The IC was polished to expose the molding compound, and then nanoindentation experiments were conducted on the exposed compound to determine the nanoindentation displacement as a function of time subjected to a prescribed load history. The nanoindentation load-displacement curve was analyzed and temperature-dependent Young's modulus at a given strain rate was determined. The spatial distribution of the Young's modulus at a given strain rate on the heterogeneous molding compound was determined from a series of nanoindentations. The Young's modulus at a given strain rate mapping was compared with an optical micrograph of the tested region of the molding compound.

### 3.2 Theoretical Background

Lu et al. [23] developed a method using viscoelastic analysis to extract the shear creep compliance of a viscoelastic material from a nanoindentation load-displacement curve. In this paper, we follow a similar approach to obtain the shear creep compliance of the molding compound. The relaxation modulus was determined through the interconversion of the viscoelastic properties, to determine the temperature-dependent Young's modulus at a given strain rate. This approach is based on linear viscoelasticity and Sneddon's solution [42].

Under a constant rate loading history, $P(t) = \dot{P}_o t H(t)$, where $\dot{P}_o$ is the constant loading rate, $t$ is elapsed time, and $H(t)$ is the Heaviside unit step function, consider nanoindentation by a rigid spherical indenter tip into a half-space composed of a linearly viscoelastic material, the nanoindentation displacement $h(t)$ is,

$$h^{3/2}(t) = \frac{3(1-\nu)}{8\sqrt{R}} \times \left[ (J_0 + \sum_{i=1}^{N} J_i) P(t) - \sum_{i=1}^{N} J_i (\dot{P}_o \tau_i)(1 - e^{-P(t)/(\dot{P}_0 \tau_i)}) \right] \tag{3.1}$$

where $R$ is the indenter tip radius, $\nu$ is the Poisson's ratio, which is assumed as 0.3. $J_0$ and $J_i$ ($i$=1,…$N$) are shear creep coefficients and $\tau_i$ ($i$=1,…$N$) are retardation times. In the generalized Kelvin model $J(t)$ is given as,

$$J(t) = J_0 + \sum_{i=1}^{N} J_i (1 - e^{-t/\tau_i}) \tag{3.2}$$

By fitting Equation (3.1) to the experimental load-displacement curves generated from the nanoindentation, the parameters $J_0$ and $J_i$ can be determined. Once $J_0$ and the $J_i$ are determined, Equation (3.2) can be used to describe the creep compliance $J(t)$. Other viscoelastic functions, such as the Young's relaxation modulus $E(t)$, can be determined using the Volterra equation [9].

$$\int_0^t E(\xi) J(t - \xi) d\xi = 2(1+\nu)t \tag{3.3}$$

Although Equation (3.3) is ill-posed [43-44], errors in the relaxation modulus can be minimized if the creep compliance data is developed for very short times. Several methods are available in literature [46-48], and the algorithm recently developed by Luk-Cyr et al. [46] was implemented to avoid the ill-posed issue of the Volterra equation.

From Equation (3.3), Young's relaxation modulus, $E(t)$ was obtained from the generalized Maxwell model as,

$$E(t) = E_{\infty} + \sum_{i=1}^{N} E_i e^{-t/\lambda_i} \tag{3.4}$$

where $E_\infty$ and $E_i$ ($i$=1,…$N$) are relaxation coefficients, and $\lambda_i$ ($i$=1,…$N$) are relaxation times, respectively. For a linearly viscoelastic material under uniaxial stress state, the uniaxial stress $\sigma(t)$ can be calculated from the applied strain history $\varepsilon(t)$, using the Boltzmann superposition principle

$$\sigma(t) = \int_o^t E(t-\xi)\frac{d\varepsilon(\xi)}{d\xi}d\xi \tag{3.5}$$

For a linearly viscoelastic material, the fundamental viscoelastic functions in the time domain are either relaxation or creep. Young's modulus at a given strain rate can be calculated from a viscoelastic function. In engineering application, the linearly viscoelastic material is often modeled as a linearly elastic material, in which Young's modulus and Poisson's ratio are used as input. In this paper, the Young's modulus at a given strain rate is calculated from the Young's relaxation function. Under a constant strain rate $\varepsilon(t) = \dot{\varepsilon}_0 t$, where $\dot{\varepsilon}_0$ is the constant strain rate, Equation (3.5) becomes [48, 49]

$$\overline{E}(\dot{\varepsilon}_0) = \frac{\sigma(t)}{\varepsilon(t)} = \frac{1}{t-t_0}\int_{t_0}^{t} E(\xi)d\xi = \overline{E}(t) \tag{3.6}$$

where $\bar{E}(\dot{\varepsilon_0})$ is the Young's modulus at strain rate $\dot{\varepsilon_0}$, and $\bar{E}(t)$ is average Young's relaxation modulus from time $t_0$ to $t$. Equation (3.6) indicates that Young's modulus at a given strain rate is equal to the time-average Young's relaxation modulus. The value of $t_0$ is chosen to be a short

time in order to develop dependable experimental data. At constant strain rate $\varepsilon(t) = \dot{\varepsilon}_0 t$, substituting relaxation modulus in Equation (3.4) into Equation (3.6) yields,

$$\overline{E}(\dot{\varepsilon}_0) = E_\infty + \sum_{i=1}^{n} E_i \frac{\lambda_i \dot{\varepsilon}_0}{\varepsilon}[1 - e^{\varepsilon/\lambda_i \dot{\varepsilon}_0}] \tag{3.7}$$

In addition, the temperature-dependent Young's relaxation modulus was also determined at the end of loading. For example, if the elapsed time is 5 seconds, then

$$E_{5s} = E\big|_{t=5s} \tag{3.8}$$

### 3.3 Experiments

The tensile specimens were prepared using the injection molding process, and the Young's modulus was determined at selected temperatures. For nanoindentation experiments, the selected IC was embedded into epoxy potting material (modified Bisphenol A-Epichlorohydin Epoxy, Allied High Tech Products, Inc.). Each potted sample was cured at room temperature for 24 hours. The ICs were cut diagonally to expose a large area to observe significant number of different sizes of the embedded glass beads as shown at low magnification in Figure 3.2(a) and a higher magnification in Figure 3.2(b). The exposed surface of the molding IC was chemo-mechanically polished to a surface roughness around 30 nm. An Atomic Force Microscope (AFM) image of the surface profile is shown in Figure 3.2(c). The glass beads are somewhat circular and are typically on the order of 10 to 30 μm in diameter. The beads are surrounded by the epoxy. An Agilent G200 Nano Indenter was used for nanoindentation measurements. The indenter can reach a maximum indentation depth of 500 μm (resolution at 0.2 nm) and a maximum load of 500 mN (resolution at 50 nN).

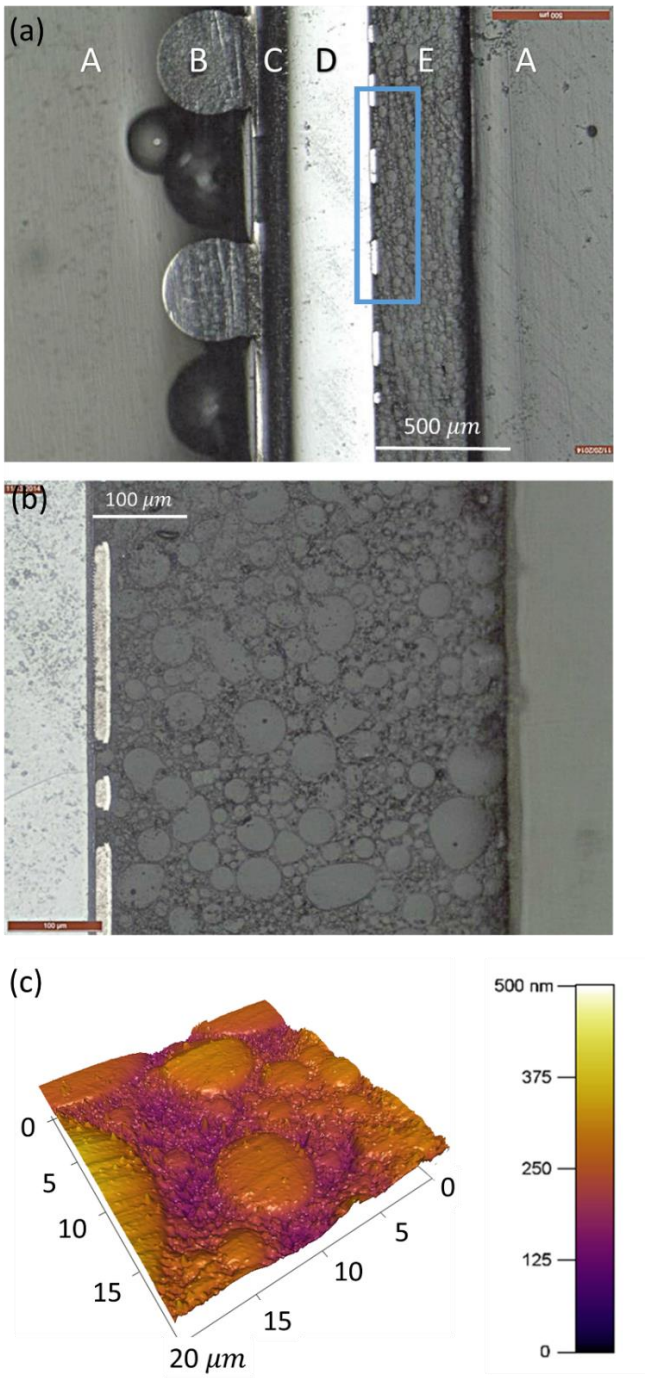


Figure 3.2. Surface images of the exposed molding compound: (a) optical micrograph of an IC chip at low magnification; A - Epoxy matrix, B - Solder, C - Die attach adhesive, D - Silicon die, E - Molding compound, (b) optical micrograph at a higher magnification of the rectangular region in (a), (c) AFM image showing the surface topography of the molding compound after polishing. Surface roughness (RMS) is 31.6 nm.

A spherical indenter tip with radius of 50 μm, made from a single crystal diamond, was used in this investigation. The schematic diagram of spherical indenter is shown in Figure 3.3(a). Ivankovic et al. [1] used a Berkovich tip to measure the Young's modulus of molding compounds, to indent deeply to obtain the bulk property. However, since the aim of this paper is to measure the Young's modulus at elevated temperature, strong viscoelastic effects will play an important role, so that Ivankovic's approach [1] may not guarantee the accuracy of measurement, especially at elevated temperatures. The analysis approach was restricted to linear viscoelasticity following the approach in [23], which restricted the initiation of plastic deformation. The large spherical indenter was chosen since it will reduce the possibility of a nonlinear deformation. A maximum load of 100 mN was applied on the indenter tip with a constant loading rate of 20 mN/s. Experiments were conducted at 20$^{o}$C, 50$^{o}$C, 70$^{o}$C, 90 $^{o}$C, 110 $^{o}$C, 125 $^{o}$C, using an Agilent heating stage.

Clearly, a single nanoindentation experiment provides only local mechanical properties since the diameter of the glass beads varies from approximately 10 to 30 μm. The spherical indenter tip with a large radius was used to indent on a glass bead and the surrounding epoxy simultaneously. Indentation sites were laid out in a rectangular array with a 50 μm Cartesian spacing in both directions, as schematically illustrated in Figure 3.3(b). The purpose was to provide sufficient distance between neighboring indents to mitigate any residual stress influence. Since the size of the glass beads in the molding compound in this study range from 10~30 μm, a spherical nanoindenter tip radius of 50 μm was used, giving a contact radius of approximately 10 μm at a nanoindentation depth of 1 μm. The spherical tip will make contact with glass beads and/or epoxy under nanoindentation at different sites. When a sufficiently large number of

nanoindentations are made, statistical analysis will provide effective mechanical properties of the molding compound.

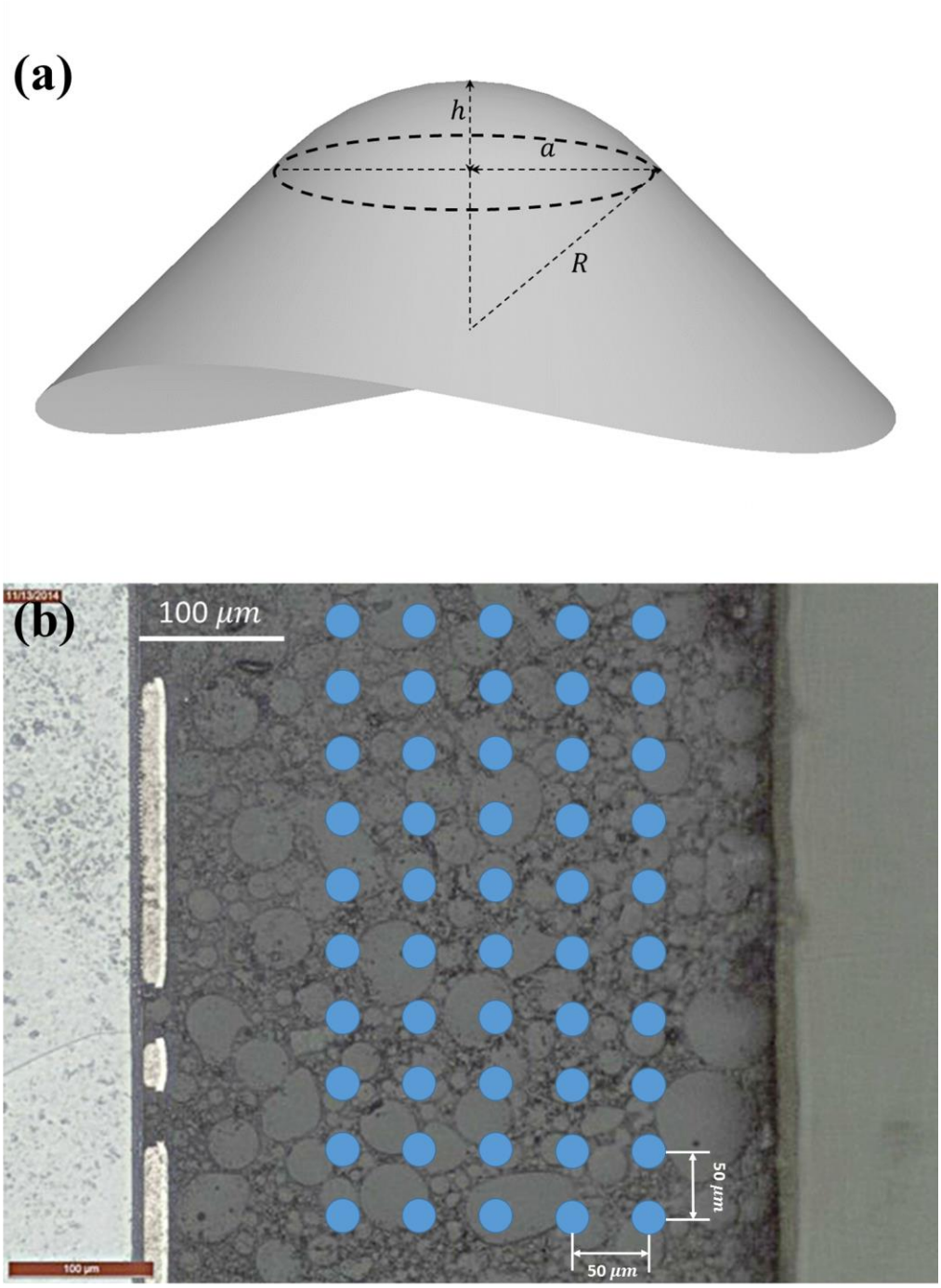


Figure 3.3. Illustration of the spherical indenter and indentation sites: (a) geometry of spherical indenter tip, (b) a rectangular grid of nanoindentation sites.

### 3.3.1 Determination of Representative Volume Element (RVE)

Since the size of the glass beads in the molding compound in this study range from 10~30 μm, a spherical nanoindenter tip radius of 50 μm was used, giving a contact radius of approximately 10 μm at a nanoindentation depth of 1 μm. The spherical tip will make contact with glass beads and/or epoxy under nanoindentation at different sites. When a sufficiently large number of nanoindentations are made, statistical analysis will provide effective mechanical properties of the molding compound. In order to establish a rational for the minimum number of indentations, a total of 100 experiments were performed. In Figure 3.4, nanoindentation load-displacement data from 5 to 100 nanoindentations was evaluated in groups. The initial average value of Young's modulus at a given strain rate was obtained from a 5 nanoindentation sample set. The sample set was subsequently increased to the number of indents shown on the abscissa in Figure 3.4 with the average value of Young's modulus at the given strain rate and the error bars (representing the standard deviation). The data suggests that at least 40 nanoindentations were required to produce a stable and converged result, with equally important the variation of the standard deviation. Figure 3.4 indicates that the first 2 to 3 data points were low, the data then increased and became stable. It suggests that there were not enough indents involved at the 5 and 10 indents to capture the effective properties of the heterogeneous molding compounds. As the number of indents increased, larger area was involved and the higher standard deviation reflects the heterogeneous nature of the molding compound. The size of an RVE determined by nanoindentation likely depends on the radius of the spherical tip used. In section "Spatial Distribution of Young's Modulus", the RVE size will also be determined using a Berkovich tip, and compared with the RVE size determined by the spherical tip with 50 μm radius.

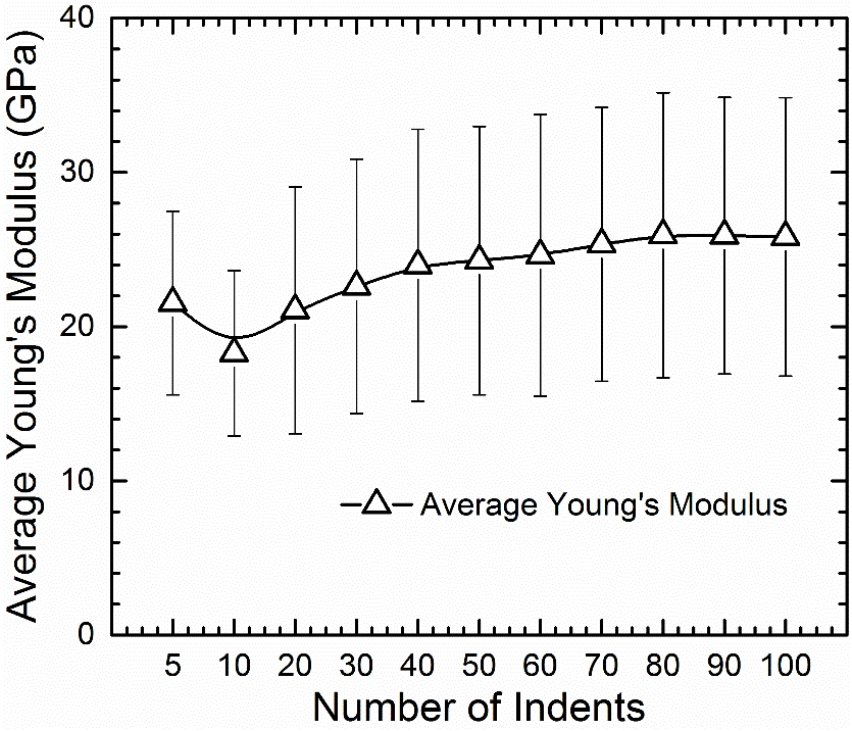


Figure 3.4. Average Young's modulus at strain rates near $10^{-3}$ $s^{-1}$ as a function of the number of indents in a rectangular grid of nanoindentation sites; the data is used to determine the representative volume element size.

Another approach to establish the RVE or number of indents is by use of the well-known ten-time rule. For a composite material, the RVE is generally ten times of the largest characteristic dimension. For the molding compound under study, the largest diameter of the bead is around 30 μm. Thus a square region with side lengths of 300 μm would provide a qualified RVE. The area of the recommended RVE is 90,000 $\mu m^2$. For a 10 × 5 indentation sites, with 50 μm spacing, the area is slightly larger than the 90,000 $\mu m^2$. Accordingly, 50 nanoindentation experiments are sufficient to characterize the effective properties of the molding compound under study. The 10 × 5 indentation sites, with 50 μm spacing, were used for room and elevated temperature experiments.

## 3.4 Results and Discussions

In this section, the methodology for determining Young's modulus at a given strain rate at room temperature will be demonstrated. The nanoindentation results are used to determine the temperature-dependent Young's modulus at a given strain rate, which will be compared with modulus data from bulk sample. Finally, the spatial distribution of the experimentally determined Young's modulus values at a given strain rate will be correlated with an optical micrograph showing the matrix materials and glass beads of the molding compound.

### 3.4.1 Nanoindentation at Room Temperature

The nanoindentations were made at the 20 × 5 grid to extract the effective property of the molding compound. Nanoindentations were carried out under load-control, in which the indenter tip was pressed onto the sample and the load was increased linearly while simultaneously recording the displacement. In the approach used in this paper, the loading curve rather than the unloading curve was used to extract the viscoelastic functions. Thus, in Figure 3.5, only the loading portion of the nanoindentation load-displacement curves at $20^{o}$ and $125^{o}$C are shown and the unloading portion is not shown. Since the nanoindentation experiments were conducted under a prescribed force history, and the measurements were made on displacements at different sites, scattering in the displacements was reflected in the two phase material consisting of the soft polymer and the stiff glass beads, the error bars show the standard deviation in the displacements. When the indenter primarily touches the polymer, the maximum displacement is relatively large, as compared to an indention made directly on a glass bead. The displacement at maximum load varied from 400 to 1000 nm.

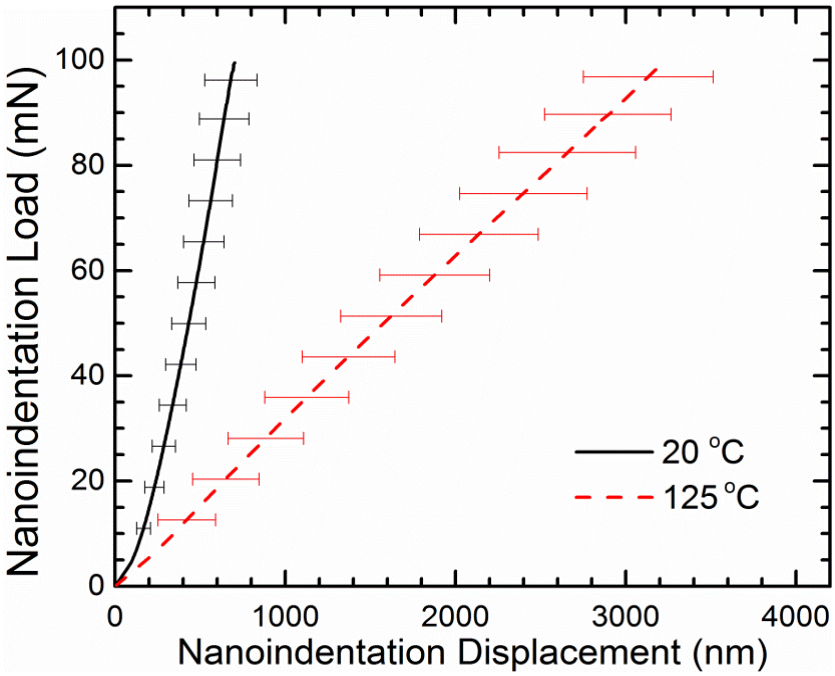


Figure 3.5. Nanoindentation load - displacement curves at 20°C and 125°C. Experiments were conducted under a given nanoindentation force history, the error bar shows standard deviation in displacements.

For each nanoindentation experiment, a nonlinear least squares fit was implemented to fit Equation (3.1) into the experimental load-displacement curve to determine the best-fit parameters: $J_0, J_1, \ldots, J_N$ for the given $\tau_1, \tau_2, \ldots, \tau_N$. It is noted that the choice of the fitting parameters is not unique and that different parameter sets can provide the same shear creep compliance. Knauss and Zhao [50] indicated that the choice of the retardation times is not subject to single stringent criterion and suggested that allowing for one retardation time per decade is usually satisfactory. In this paper, five predetermined retardation times were selected, they are 0.01 s, 0.1 s, 1 s, 10 s, and 100 s, which will encompass the experimental time frame to provide a smooth creep function. The corresponding compliance parameters $J_i$ were obtained from this curve fitting process. The best-fit parameters were then used in Equation (3.2) and

Equation (3.3) to obtain the Young's relaxation modulus. Finally Equation (3.6) and Equation (3.7) were used to calculated the Young's modulus at a given strain rate.

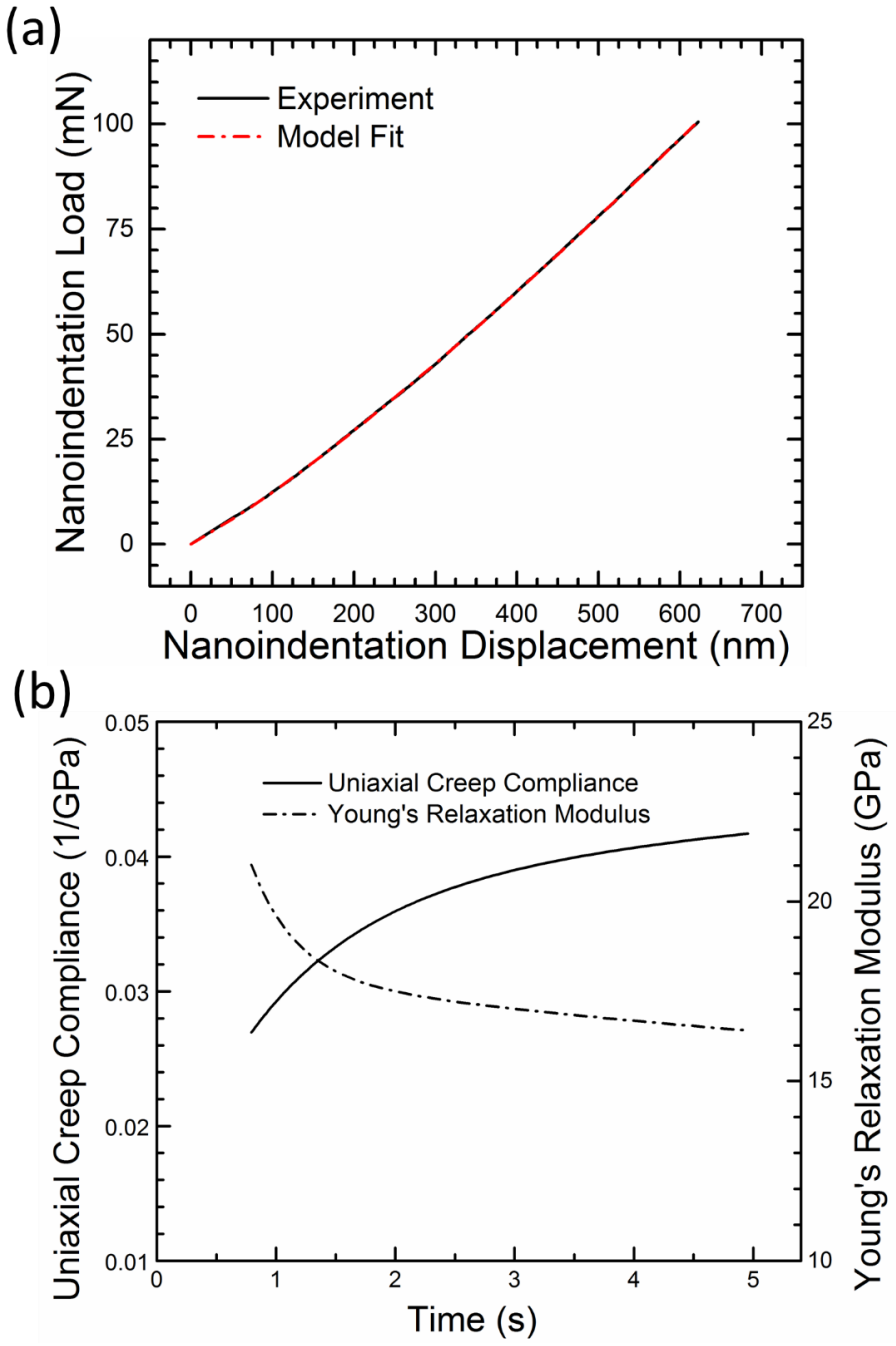


Figure 3.6. Nanoindentation results at 20°C: (a) experimental and fitted nanoindentation load - displacement curves, (b) uniaxial creep compliance and Young's relaxation modulus.

This procedure is illustrated with one set of nanoindentation data. Both the experimental and fitted load-displacement curves are shown in Figure 3.6(a). The least squares correlation coefficient is $1.3\times10^{-4}$, indicating a good correlation. The parameters used in Equation (3.1) to obtain the fitted curve as shown in Figure 3.6(a) were used in Equation (3.2) to determine the shear creep compliance, given as,

$$J(t) = 0.01071 + 0.01206(1-e^{\frac{-t}{0.01}}) + 0.02417(1-e^{\frac{-t}{0.1}}) + 0.08932(1-e^{-t}) + 0.04393(1-e^{\frac{-t}{10}}) + 0.00546(1-e^{\frac{-t}{100}}) \quad \text{(1/GPa)} \tag{3.9}$$

where $t$ is elapsed time in seconds. By implementing the approach by Luk-Cyr's et al. [42], the Young's relaxation function was determined as,

$$E(t) = 13.99 + 146.22e^{-231.1t} + 52.65e^{-21.28t} + 25.71e^{-2.647t} + 3.859e^{-0.1294t} + 0.4035e^{-0.01030t} \quad \text{(GPa)} \tag{3.10}$$

The uniaxial creep compliance (can be directly calculated from shear creep compliance by assuming the constant Poisson's ratio) and Young's relaxation function are shown in Figure 3.6(b). Subsequently the Young's modulus at a given strain rate $8.3\times10^{-4}$ $s^{-1}$ and Young's relaxation modulus $E_{5s}$ were calculated as 17.4 GPa and 16.4 GPa, respectively.

Similarly, for the rest of the 100 experiments conducted at room temperature, curve fitting was performed with the same procedure shown above. Finally, the average value of all one hundred experiments, for the two phase material was obtained and cited as Young's modulus at room temperature for a given strain rate. As long as the indentation area meets the RVE requirement, the effective property of the highly heterogeneous molding compound can be determined. In this study, the isotropic response of the molding compound was assumed. Future

work may take into account the anisotropy of the interface of glass beads and surrounding polymer matrix.

### 3.4.2 Nanoindentation at Elevated Temperatures

Nanoindentation load-displacement curves generated from experiments at elevated temperatures were obtained at 50±0.3ºC, 70±0.5ºC, 90±1ºC, 110±2.2ºC and 125±3ºC. Figure 3.7 shows the average experimental and fitted curves for all temperatures.

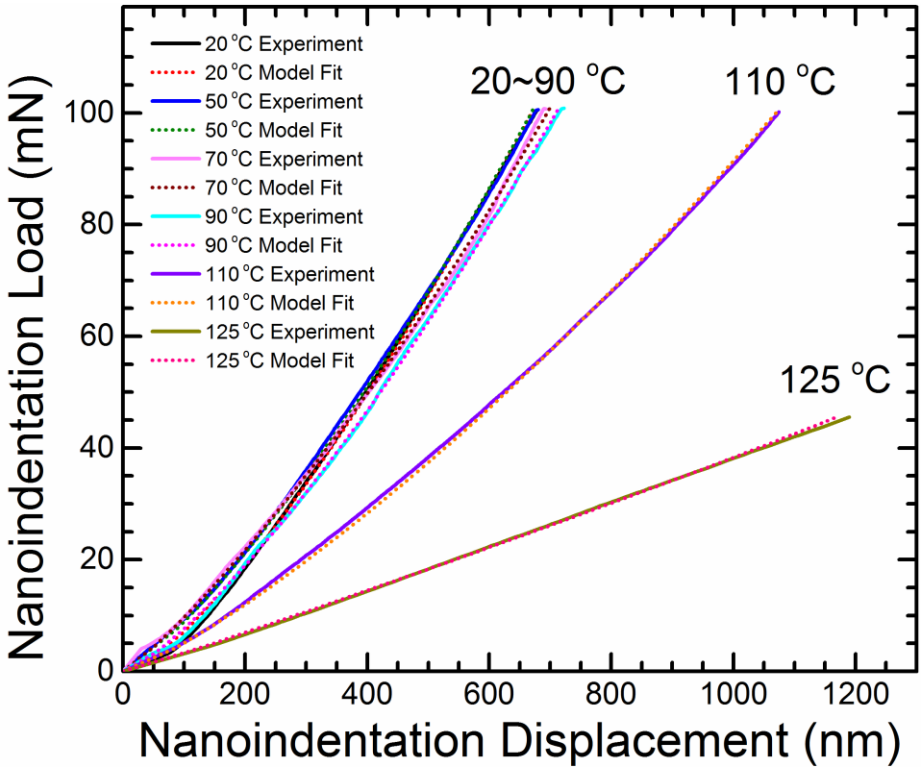


Figure 3.7. Typical nanoindentation load - displacement curves at several temperatures. Solid lines are experimental data and dotted lines are fitted curves from Equation (3.1).

Clearly the higher temperature softens the polymer and reduces the stiffness. The temperature influence is also observed in Figure 3.5 from the wider data band for the 125ºC experiment as compared to the 20ºC data bands. The wider data bands at 125ºC suggest the

polymer is sufficiently soft to allow the indenter to deflect not only the polymer but also the glass beads in the polymer. It is possible that the polymer at 125°C has reached the glass transition region.

As shown in Figure 3.7, when temperature increased, the displacement at maximum load became larger, a common trend for most materials. At temperatures lower than 90°C, the typical nanoindentation load-displacement curves were close to each other, and the range of the maximum displacement for the 20°C to 90°C temperature range was very similar, indicating that the molding compound has not approached its glass transition region and the reinforcement from the glass beads is significant. When the temperatures were increased to approximately 110°C and 125°C, both the shape of nanoindentation curves and the maximum displacement values changed significantly, compared to those below 90°C. Note that, for the molding compound under investigation, the displacement limit for linear viscoelasticity was set to 1200 nm, thus, at 125°C, the nanoindentation load-displacement curve up to 1200 nm depth was used for fitting by Equation (3.1) and shown in Figure 3.7. Following the previous procedures, the Young's modulus at a given strain rate and Young's relaxation modulus $E_{5s}$ for each experiment, at each temperature were calculated and the effective properties were calculated from the average of the results obtained at different sites.

Figure 3.8 shows the Young's modulus at a given strain rate and Young's relaxation modulus $E_{5s}$. As expected, the effective Young's modulus decreases as the temperature increases. In addition, the error bar indicates the standard deviation. The standard deviation is higher at lower temperatures, this is likely due to the fact that at lower temperatures the polymer provides support to the glass beads so that there is a significant contrast in modulus values,

depending on whether the indenter tip makes contact with only polymer or the glass beads supported by the stiff polymer at a lower temperature.

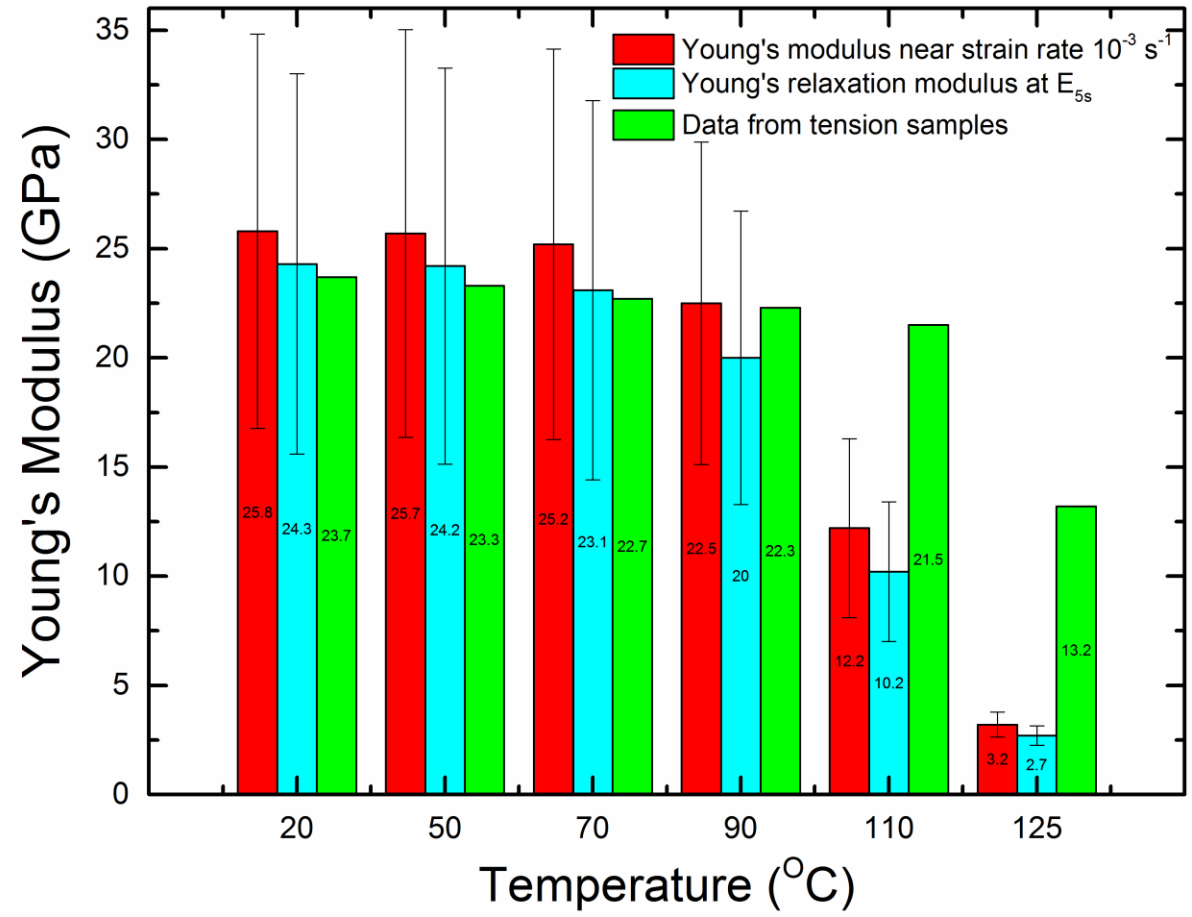


Figure 3.8. Temperature-dependent modulus data, including Young's modulus at strain rate in the neighborhood of $10^{-3}$ $s^{-1}$. Young's relaxation modulus at time t = 5s which is the ending point of nanoindentation experiment at various temperatures, and bulk data obtained from dog-bone samples.

However, at elevated temperatures (especially at 110°C and 125°C), the polymer approached its glass transition region and became softer, providing less support to the glass beads, and thus the load spreading of the glass beads had less influence on the deflection response. Also, Figure 3.8 shows the comparison of the two calculated temperature-dependent effective Young's modulus values obtained from nanoindentation with the material properties

obtained from bulk samples. It is seen that, at temperatures lower than 110$^{o}$C, the effective Young's modulus values obtained from nanoindentation agree reasonably well with data obtained from bulk samples. At 110$^{o}$C and 125$^{o}$C, the effective Young's modulus values obtained from nanoindentation were lower than data for the bulk samples. For bulk samples under uniaxial loads for measurement of Young's modulus, glass beads displace collectively to satisfy plane assumption, thus glass beads provide stiffness to the molding compound; for a small amount of molding compound in IC under nanoindentation, glass beads, with a weak support from polymer at a higher temperature, are displaced by a nanoindenter tip and deform locally so that the contribution of the softer material behavior from the polymer plays a more significant role in the stiffness of the molding compound, giving smaller modulus than the traditional bulk testing. The higher modulus values compared to the lower nanoindentation values is influenced by the bulk material sample size interacting with the large volume of beads, by the influence of the Poisson contraction during experiment. The effect on packaging dimensions and processing [51,52] herein may explain the difference at high temperatures between the bulk material data and the nanoindentation results.

### 3.4.3 Effect of Poisson's Ratio

In general, for a viscoelastic material, Poisson's ratio is a function of temperature and time. In the analysis of the nanoindentation data in this study, a constant Poisson's ratio of 0.3 was used for all temperatures, primarily for the following reasons: first, the Poisson's ratio of 0.3 is often used for finite element analysis of molding compound used in the glassy state; second, the Poisson's ratio is in general around 0.3 for epoxies at room temperature, it becomes larger when the temperature gradually approaches the glass transition regime. The volume fraction of glass

beads in the molding compound in this study is approximately 70%. When the rule of mixture is used to estimate the Poisson's ratio at elevated temperatures, the Poisson's ratio for the molding compound will not change appreciably with temperature, and as a result the calculated Young's modulus data is not sensitive to the Poisson's ratio.

Table 3.1. Effect of Poisson's ratio on the average Young's modulus at given strain rate.

| Temperature (°C) | Assumed Poisson's ratio | Young's Modulus at given strain rate (GPa) | Poisson's ratio taken from [1] | Young's Modulus at given strain rate (GPa) | Difference in modulus |
|---|---|---|---|---|---|
| 22 | 0.3 | 25.8±9.0 | 0.32 | 25.9±9.1 | 0.4% |
| 50 | 0.3 | 25.7±9.3 | 0.34 | 26.4±9.6 | 2.7% |
| 70 | 0.3 | 25.2±8.9 | 0.37 | 26.6±9.4 | 5.4% |
| 90 | 0.3 | 22.5±7.4 | 0.38 | 24.1±7.9 | 6.9% |
| 110 | 0.3 | 12.2±4.1 | 0.395 | 13.2±4.4 | 8.4% |
| 125 | 0.3 | 3.2±0.6 | 0.42 | 3.5±0.7 | 10.5% |

Since the Poisson's ratio for the molding compound at elevated temperatures is not available in literature, we took the temperature-dependent Poisson's ratio data for PMMA [54] to estimate the trend of the Poisson's ratio for the epoxy used in this study. The Poisson ratio for the epoxy is estimated to be between 0.3 and 0.45. If the Poisson's ratio of the molding compound is same as the epoxy, Young's modulus at given strain rates at different temperatures was obtained by the viscoelastic analysis. The calculated effective properties are shown in Table 3.1. The difference is in general less than 10%. If the rule of mixture is used, the Poisson's ratio of the molding compound is estimated in the range of 0.28 at room temperature to 0.34 at 125°C, giving a difference of less than 3% in Young's modulus at a given strain rate.

### 3.4.4 Spatial Distribution of Young's Modulus

Nanoindentation on composites and other multi-phase materials was made to determine the properties of the individual constituents [55-58]. In this study, however the attention was not focused on extracting material properties for individual phases, rather the effective properties of a two-part heterogeneous molding compound. The approach used for the development of the RVE also provided a method to produce a mapping of the experimental Young's modulus over the region of interest. The Young's modulus map was plotted to compare the experimental results with an optical micrograph, to show the polymer and the random bead distribution. Clearly the high value of Young's modulus regions should map to the locations in the optical micrograph showing glass beads as observed in Figure 3.9(a).

To obtain a high resolution modulus map, a Berkovich tip was used. The maximum nanoindentation load was selected as 15 mN and the molding compound region of interest used a $30 \times 30$ grid with a 5 μm distance between neighboring nanoindentation sites. The typical maximum displacement attained was around 700 nm. Thus the 5 μm distance was sufficient to eliminate the residual stress effect from other indents, since the plastic zone was around 2~3 times of the maximum nanoindentation depth [59, 60]. The equation for linearly viscoelastic analysis with a Berkovich tip can be found in [23]. After obtaining the discrete Young's modulus at each nanoindentation site, instead of plotting results directly like a checkerboard [55, 58], cubic interpolation was implemented to obtain a smooth contour plot. Figure 3.9(b) shows that the spatial distribution of Young's modulus has captured the influence of the glass beads and the surrounding polymers. There is in very good agreement between the optical micrograph and Young's modulus map, which further validated the approach.

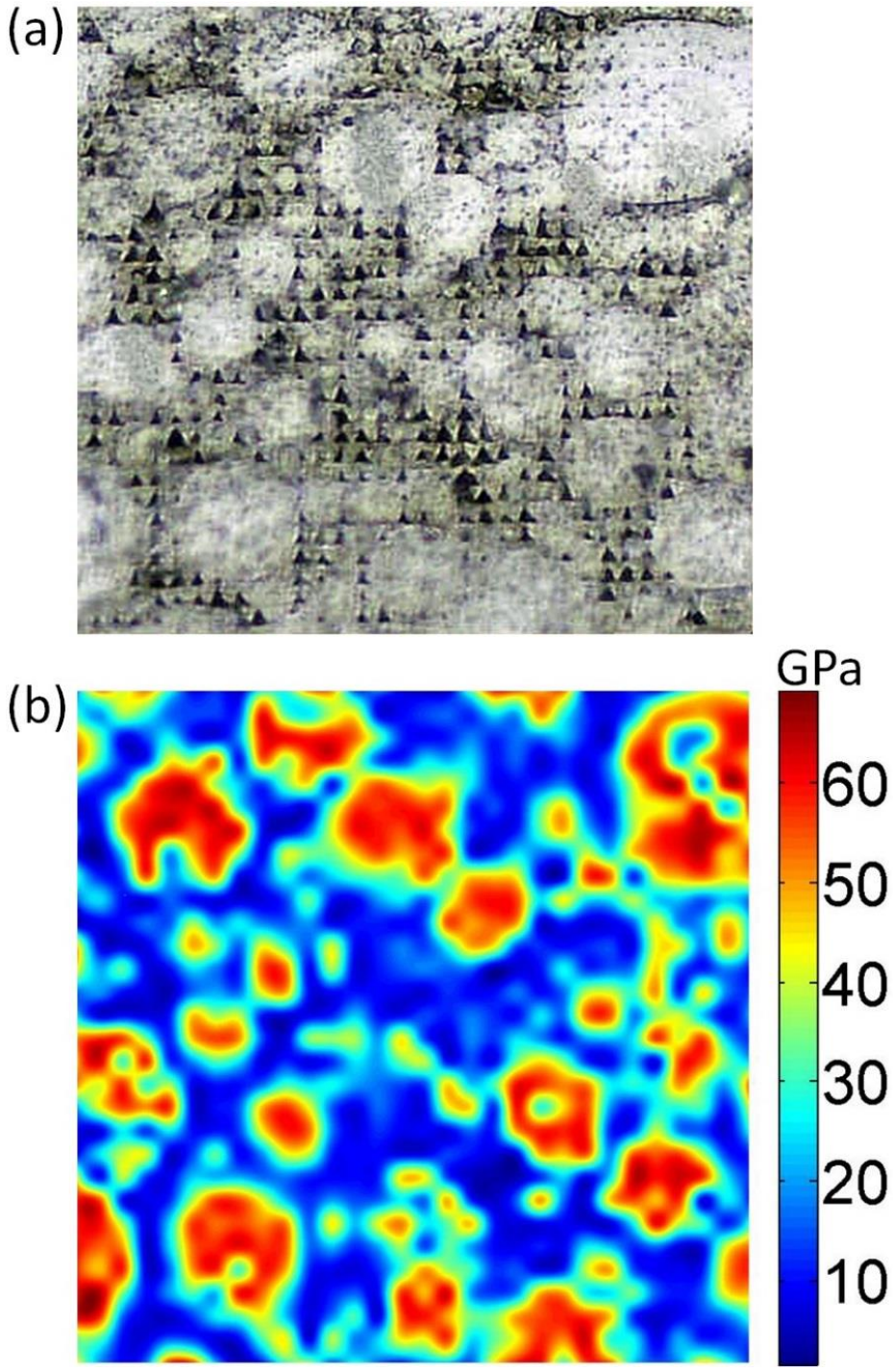


Figure 3.9. Spatial variation of effective Young's modulus at strain rates near 10-3 s-1: (a) optical micrograph of residual indents from 30 × 30 nanoindentations by Berkovich tip on the surface of a molding compound, (b) distribution of effective Young's modulus at strain rates near 10-3 s-1 in the same area shown in (a).

Since a grid pattern of nanoindentations were conducted, the data contains information such as surface and volume fraction. With information contained in the experiments, further statistical analysis can be applied to determine the properties of the polymer and glass beads independently, then generate the molding compound properties based on the statistical representation of the constituents. Statistical analysis was conducted on the data in the Figure 3.9(b). The volume ratio of glass beads to epoxy in the molding compound can be determined as the proportion of the frequency of Young's modulus measured by nanoindentation when the number of data points is large. Due to the heterogeneous nature of the sample, the glass beads and the epoxy are in random distributions, and the probability density function follows a Gaussian-like distribution.

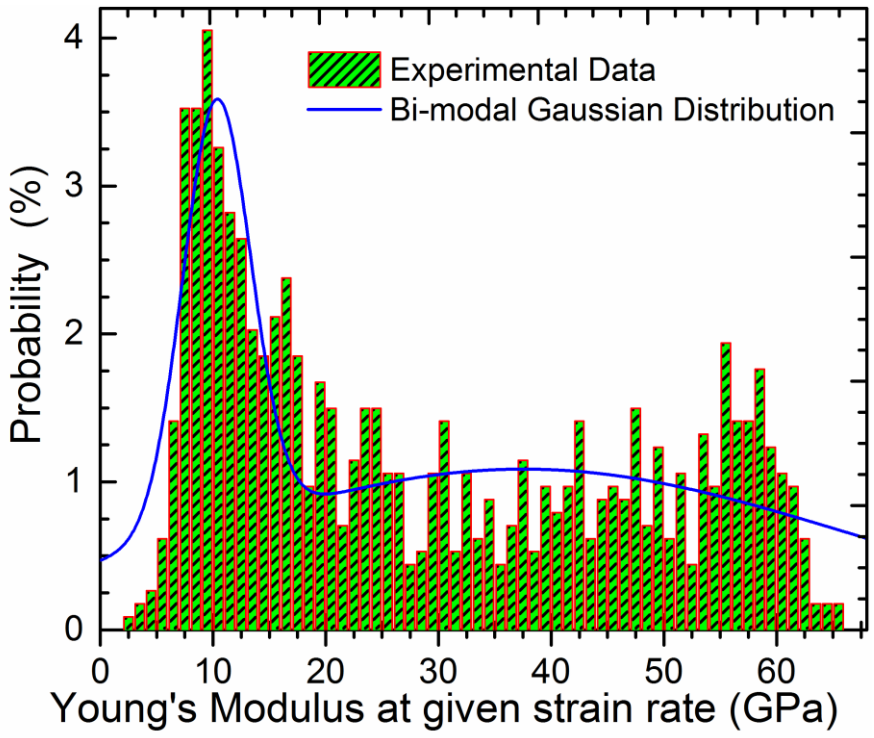


Figure 3.10. Histogram for the Young's modulus at strain rates near $10^{-3}$ $s^{-1}$ for the molding compound. The peaks values are for epoxy and glass beads. Volume fraction of the glass beads is 78.2%.

From the histogram in Figure 3.10, two peaks were identified. The probability distribution of Young's modulus of the molding compound is assumed to follow the summation of two independent Gaussian distributions given by,

$$G(E|\mu_1,\sigma_1,\mu_2,\sigma_2,\alpha)=\frac{\alpha}{\sigma_1\sqrt{2\pi}}e^{\frac{-(E-\mu_1)^2}{2\sigma_1^2}}+\frac{1-\alpha}{\sigma_2\sqrt{2\pi}}e^{\frac{-(E-\mu_2)^2}{2\sigma_2^2}} \quad (3.11)$$

where $\mu_1$ and $\mu_2$ are the expectation values; $\sigma_1$ and $\sigma_2$ are the standard deviations (SDs) for the epoxy and glass beads, respectively; $\alpha$ and (1- $\alpha$) are the weight factors for the epoxy and glass beads, respectively. The best-fit parameters were determined using the Levenberg-Marquardt algorithm. Table 3.2 summarizes the best-fit model parameters with 0.661 coefficient of determinant. The volume ratio for epoxy to glass beads was determined as 21.8/78.2.

Table 3.2. Parameters for the Bi-modal Gaussian distribution of the Young's modulus at a given strain rate of the molding compound.

| Parameters | $\mu_1$ (GPa) | $\sigma_1$ (GPa) | $\mu_2$ (GPa) | $\sigma_2$ (GPa) | $\alpha$ |
|---|---|---|---|---|---|
| Value | 10.3±0.34 | 3.02±0.48 | 37.5±5.44 | 28.7±9.78 | 0.218±0.080 |
| Constituent | Epoxy | Epoxy | Glass beads | Glass beads | Epoxy |

The optical micrograph of the molding compound, as shown in Figure 3.9(a), was analyzed using ImageJ [61], and the surface fraction of glass beads was calculated as 70.3%, which is close to the 78.2% volume fraction obtained from the statistical analysis of the Young's modulus data. The effective Young's modulus at a given strain rate, obtained from the rule of mixture, is $E$ = 31.5 GPa, which is slightly higher than what was obtained from average data, 28.8 GPa, from the 900 sites of nanoindentation; the difference is about 9.4%. Also, from the spherical

nanoindentation, the effective Young's modulus at a given strain rate was obtained as 25.8 GPa. These numbers are in general in reasonable agreement.

RVE analysis was made for nanoindentation using a Berkovich indenter tip at 900 nanoindentation sites. The average value of Young's modulus at a given strain rate was obtained from nanoindentation on a square grid of $N \times N$, where $N$ is the number of grid points on each side of the square. The space between two neighboring grid points was maintained at 5 μm. The number of grid points was gradually increased, subsequently the average value and the standard deviation of Young's modulus at the given strain rate were evaluated.

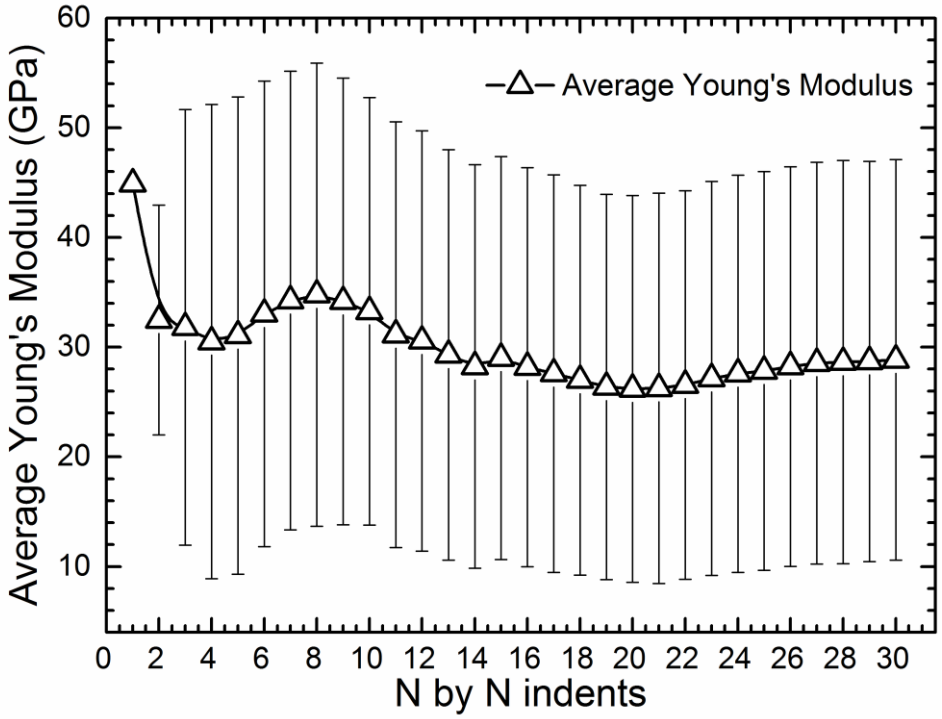


Figure 3.11. Average Young's modulus at given strain rates as a function of the number of indents (N×N) in a rectangular grid of Berkovich nanoindentation sites.

In Figure 3.11, nanoindentation load-displacement data from $1 \times 1$ to $30 \times 30$ nanoindentations are shown in groups. The data suggests that at $26 \times 26$ nanoindentations,

corresponding to an RVE area of 125 μm × 125 μm, were required to produce converging result. The side length of 125 μm is about six times of the average glass bead diameter, which is 20 μm. In comparison with the RVE size (90,000 $\mu m^2$) determined by the 50 μm spherical tip, the RVE size determined using a Berkovich tip is smaller. However a much larger number of nanoindentations are needed to obtain the effective mechanical property data compared with the use of spherical tip with 50 μm radius: It only took 50 nanoindentations to obtain the effective Young's modulus at a given strain when a spherical tip of 50 μm radius was used, while it required more than 600 nanoindentations using a Berkovich tip. The effective Young's modulus at a given strain rate, obtained from RVE using Berkovich tip, is about 28.8 GPa, which is within 12% of the value of 25.8 GPa, which is the value determined by RVE using spherical nanoindentation.

Table 3.3. Young's modulus of the molding compound obtained from different methods.

| Method | E (GPa) | Standard Deviation |
|---|---|---|
| Elastic-plastic analysis [12,13] | 39.7 | 15.6 |
| Viscoelastic analysis [23] | 28.8 | 16.4 |

As mentioned earlier, the Oliver-Pharr method, experiences difficulties to measure the mechanical properties of viscoelastic materials. One well-known phenomenon is the formation of unloading "nose" or negative stiffness during unloading that often occurs during slow loading-unloading in nanoindentation on a viscoelastic material [21, 22]. For our experiments, a negative slope of initial unloading curve was shown as in Figure 3.1. For those 900 nanoindentation experiments mentioned above, the average Young's modulus calculated from Oliver-Pharr

method is shown in Table 3.3, which yields a nearly 40% larger Young's modulus value than obtained from the approach used in this paper.

## 3.5 Conclusions

Young's modulus for a molding compound was measured by nanoindentation on a production IC that was potted and cross-sectioned. A 50 μm radius diamond spherical tip was used in nanoindentations, from which the effective properties of the highly heterogeneous molding compound were determined. The effective Young's modulus values at a given strain rate were obtained at 20°C, 50°C, 70°C, 90°C, 110°C and 125°C. The experimental load-displacement curves were fit to an analytical model, generating the parameters for the Prony series for the shear creep compliance function, which was further inverted to determine the effective Young's relaxation modulus and also the Young's modulus at a given strain rate.

Two separate definitions, namely an effective Young's modulus at a given strain rate and Young's relaxation modulus at a given time were used to represent the temperature-dependent Young's modulus of the molding compound. The values obtained from the two methods were in good agreement with data obtained from bulk samples at or below 90°C. However when the temperature was near or higher than 110°C, the Young's modulus at a given strain rate determined by nanoindentation was significantly lower than the data obtained from bulk samples. In addition, nanoindentations were made at a large number of sites on a rectangular grid using a Berkovich tip, to generate the spatial distribution of Young's modulus at room temperature to compare to an optical micrograph of the molding compound. The modulus map was in a good agreement with optical micrograph showing high modulus values in regions where glass beads were prevalent and low modulus values elsewhere.

## 3.6 References


1. Ivankovic, Andrej, Kris Vanstreels, Daniel Vanderstraeten, Guy Brizar, Renaud Gillon, Eddy Blansaer, and Bart Vandevelde. "Comparison of experimental methods for the extraction of the elastic modulus of molding compounds used in IC packaging." *Microelectronics Reliability* 52, no. 11 (2012): 2677-2684.

2. Zou, Yida, J. C. Suhling, R. C. Jaeger, Shun-Tien Lin, J. T. Benoit, and R. R. Grzybowski. "Die surface stress variation during thermal cycling and thermal aging reliability tests." In *Electronic Components and Technology Conference, 1999. 1999 Proceedings. 49th*, pp. 1249-1260. IEEE, 1999.

3. Schindler-Saefkow, Florian, F. Rost, A. Otto, W. Faust, B. Wunderle, B. Michel, and S. Rzepka. "Stress chip measurements of the internal package stress for process characterization and health monitoring." In *Thermal, Mechanical and Multi-Physics Simulation and Experiments in Microelectronics and Microsystems (EuroSimE), 2012 13th International Conference on*, pp. 1-10. IEEE, 2012.

4. Hong, Bor Zen, and Lo-Soun Su. "On thermal stresses and reliability of a PBGA chip scale package." In *Electronic Components & Technology Conference, 1998. 48th IEEE*, pp. 503-510. IEEE, 1998.

5. Clement, A., and M. Saint-Paul. "Ultrasonic measurements of microelectronic molding compounds." *Journal of Materials Science: Materials in Electronics* 13, no. 1 (2002): 21-25.

6. Canumalla, Sridhar, and Michael G. Oravecz. "Nondestructive elastic property characterization of IC encapsulants." *ASME APPLIED MECHANICS DIVISION-PUBLICATIONS-AMD* 222 (1997): 25-32.

7. Kim, Yeong K., In Soo Park, and Jooho Choi. "Warpage mechanism analyses of strip panel type PBGA chip packaging." *Microelectronics Reliability* 50, no. 3 (2010): 398-406.

8. Miyake, Kiyoshi, Tsukasa Yoshida, Hyung Gil Baik, and Sang Wook Park. "Viscoelastic warpage analysis of surface mount package." *Journal of Electronic Packaging* 123, no. 2 (2001): 101-104.

9. Ferry, John D. *Viscoelastic properties of polymers*. John Wiley & Sons, 1980.

10. Lu, H., and Wolfgang G. Knauss. "The role of dilatation in the nonlinearly viscoelastic behavior of PMMA under multiaxial stress states." *Mechanics of Time-Dependent Materials* 2, no. 4 (1998): 307-334.

11. Knauss, Wolfgang G., Igor Emri, and Hongbing Lu. *Mechanics of polymers: viscoelasticity*. Springer US, 2008.

12. Oliver, Warren Carl, and George Mathews Pharr. "An improved technique for determining hardness and elastic modulus using load and displacement sensing indentation experiments." *Journal of materials research* 7, no. 06 (1992): 1564-1583.

13. Oliver, Warren C., and Georges M. Pharr. "Measurement of hardness and elastic modulus by instrumented indentation: Advances in understanding and refinements to methodology." *Journal of materials research* 19, no. 01 (2004): 3-20.

14. Daphalapurkar, N. P., F. Wang, B. Fu, H. Lu, and R. Komanduri. "Determination of mechanical properties of sand grains by nanoindentation." *Experimental Mechanics* 51, no. 5 (2011): 719-728.

15. Wang, F., B. Fu, H. Luo, S. Staggs, R. A. Mirshams, W. L. Cooper, S. Y. Park, M. J. Kim, C. Hartley, and H. Lu. "Characterization of the grain-level mechanical behavior of Eglin sand by nanoindentation." *Experimental Mechanics* 54, no. 5 (2014): 871-884.

16. Hu, Zhenxing, Yingjie Du, Huiyang Luo, Bin Zhong, and Hongbing Lu. "Internal deformation measurement and force chain characterization of mason sand under confined compression using incremental digital volume correlation." *Experimental Mechanics* 54, no. 9 (2014): 1575-1586.

17. Luo, Huiyang, Yingjie Du, Zhenxing Hu, and Hongbing Lu. "High-strain rate compressive behavior of dry mason sand under confinement." In *Dynamic Behavior of Materials, Volume 1*, pp. 325-333. Springer International Publishing, 2015.

18. Canepa, Pieremanuele, Kui Tan, Yingjie Du, Hongbing Lu, Yves J. Chabal, and Timo Thonhauser. "Structural, elastic, thermal, and electronic responses of small-molecule-loaded metal–organic framework materials." *Journal of Materials Chemistry A* 3, no. 3 (2015): 986-995.

19. Liu, Y., B. Wang, M. Yoshino, S. Roy, H. Lu, and R. Komanduri. "Combined numerical simulation and nanoindentation for determining mechanical properties of single crystal copper at mesoscale." *Journal of the Mechanics and Physics of Solids* 53, no. 12 (2005): 2718-2741.

20. Liu, Y., S. Varghese, J. Ma, M. Yoshino, H. Lu, and R. Komanduri. "Orientation effects in nanoindentation of single crystal copper." *International Journal of Plasticity* 24, no. 11 (2008): 1990-2015.

21. Briscoe, B. J., L. Fiori, and E. Pelillo. "Nano-indentation of polymeric surfaces." *Journal of Physics D: Applied Physics* 31, no. 19 (1998): 2395.

22. VanLandingham, Mark R. *Review of instrumented indentation*. National Inst Of Standards and Technology Gaithersburg MD, 2003.

23. Lu, H., B. Wang, J. Ma, G. Huang, and H. Viswanathan. "Measurement of creep compliance of solid polymers by nanoindentation." *Mechanics of time-dependent materials* 7, no. 3-4 (2003): 189-207.

24. Huang, G., B. Wang, and H. Lu. "Measurements of viscoelastic functions of polymers in the frequency-domain using nanoindentation." *Mechanics of Time-Dependent Materials* 8, no. 4 (2004): 345-364.

25. Huang, G., and H. Lu. "Measurements of two independent viscoelastic functions by nanoindentation." *Experimental Mechanics* 47, no. 1 (2007): 87-98.

26. Cheng, L., X. Xia, W. Yu, L. E. Scriven, and W. W. Gerberich. "Flat-punch indentation of viscoelastic material." *Journal of Polymer Science Part B: Polymer Physics* 38, no. 1 (2000): 10-22.

27. Lu, Hongbing, Gang Huang, and Fang Wang. "Measurements of viscoelastic properties of polymers using flat punch indenter." In *Proceedings of the SEM annual conference and exposition on experimental and applied mechanics*, vol. 2, pp. 697-704. 2007.

28. Cheng, Yang-Tse, and Che-Min Cheng. "General relationship between contact stiffness, contact depth, and mechanical properties for indentation in linear viscoelastic solids using axisymmetric indenters of arbitrary profiles." *Applied Physics Letters* 87, no. 11 (2005): 111914.

29. Cheng, Yang-Tse, Che-Min Cheng, and Wangyang Ni. "Methods of obtaining instantaneous modulus of viscoelastic solids using displacement-controlled instrumented indentation with axisymmetric indenters of arbitrary smooth profiles." *Materials Science and Engineering: A* 423, no. 1 (2006): 2-7.

30. Cao, Yanping. "Determination of the creep exponent of a power-law creep solid using indentation tests." *Mechanics of Time-Dependent Materials* 11, no. 2 (2007): 159-172.

31. Kucuk, Y., C. Mollamahmutoglu, Y. Wang, and H. Lu. "Nonlinearly viscoelastic nanoindentation of PMMA under a spherical tip." *Experimental Mechanics* 53, no. 5 (2013): 731-742.

32. Lu, Hongbing, Gang Huang, Bo Wang, Arif Mamedov, and Sachin Gupta. "Characterization of the linear viscoelastic behavior of single-wall carbon nanotube/polyelectrolyte multilayer nanocomposite film using nanoindentation." *Thin Solid Films* 500, no. 1 (2006): 197-202.

33. Francius, Grégory, Joseph Hemmerle, Vincent Ball, Philippe Lavalle, Catherine Picart, Jean-Claude Voegel, Pierre Schaaf, and Bernard Senger. "Stiffening of soft polyelectrolyte architectures by multilayer capping evidenced by viscoelastic analysis of AFM indentation measurements." *The Journal of Physical Chemistry C* 111, no. 23 (2007): 8299-8306.

34. Sadr, Alireza, Yasushi Shimada, Hongbing Lu, and Junji Tagami. "The viscoelastic behavior of dental adhesives: a nanoindentation study." *dental materials* 25, no. 1 (2009): 13-19.

35. Huang, Gang, Nitin P. Daphalapurkar, Rong Z. Gan, and Hongbing Lu. "A method for measuring linearly viscoelastic properties of human tympanic membrane using nanoindentation." *Journal of biomechanical engineering* 130, no. 1 (2008): 014501.

36. Daphalapurkar, Nitin P., Chenkai Dai, Rong Z. Gan, and Hongbing Lu. "Characterization of the linearly viscoelastic behavior of human tympanic membrane by nanoindentation." *Journal of the mechanical behavior of biomedical materials* 2, no. 1 (2009): 82-92.

37. Huang, Xiaoqin, and Assimina A. Pelegri. "Mechanical characterization of thin film materials with nanoindentation measurements and FE analysis." *Journal of Composite Materials* 40, no. 15 (2006): 1393-1407.

38. Florentin, Eric, and Gilles Lubineau. "Identification of the parameters of an elastic material model using the constitutive equation gap method." *Computational Mechanics* 46, no. 4 (2010): 521-531.

39. Moussawi, Ali, Gilles Lubineau, Eric Florentin, and Benoit Blaysat. "The constitutive compatibility method for identification of material parameters based on full-field measurements." *Computer Methods in Applied Mechanics and Engineering* 265 (2013): 1-14.

40. Sutton, M. A., W. J. Wolters, W. H. Peters, W. F. Ranson, and S. R. McNeill. "Determination of displacements using an improved digital correlation method." *Image and vision computing* 1, no. 3 (1983): 133-139.

41. Lu, H., and P. D. Cary. "Deformation measurements by digital image correlation: implementation of a second-order displacement gradient." *Experimental mechanics* 40, no. 4 (2000): 393-400.

42. Sneddon, Ian N. "The relation between load and penetration in the axisymmetric Boussinesq problem for a punch of arbitrary profile." *International journal of engineering science* 3, no. 1 (1965): 47-57.

43. Huang, Gang, and Hongbing Lu. "Measurement of Young's relaxation modulus using nanoindentation." *Mechanics of time-dependent materials* 10, no. 3 (2006): 229-243.

44. Emri, Igor, and N. W. Tschoegl. "Generating line spectra from experimental responses. Part I: Relaxation modulus and creep compliance." *Rheologica Acta* 32, no. 3 (1993): 311-322.

45. Tschoegl, N. W., and I. Emri. "Generating line spectra from experimental responses. III. Interconversion between relaxation and retardation behavior." *International Journal of Polymeric Materials* 18, no. 1-2 (1992): 117-127.

46. Luk-Cyr, Jacques, Thibaut Crochon, Chun Li, and Martin Lévesque. "Interconversion of linearly viscoelastic material functions expressed as Prony series: a closure." *Mechanics of Time-Dependent Materials* 17, no. 1 (2013): 53-82.

47. Baumgaertel, M., and H. H. Winter. "Determination of discrete relaxation and retardation time spectra from dynamic mechanical data." *Rheologica Acta* 28, no. 6 (1989): 511-519.

48. Luo, Huiyang, Guoqiang Lu, Samit Roy, and Hongbing Lu. "Characterization of the viscoelastic behavior of bismaleimide resin before and after exposure to high temperatures." *Mechanics of Time-Dependent Materials* 17, no. 3 (2013): 369-399.

49. Luo, Huiyang, Yanli Zhang, Bo Wang, and Hongbing Lu. "Characterization of the compressive behavior of glass fiber reinforced polyurethane foam at different strain rates." *Journal of Offshore Mechanics and Arctic Engineering* 132, no. 2 (2010): 021301.

50. Knauss, Wolfgang G., and J. Zhao. "Improved relaxation time coverage in ramp-strain histories." *Mechanics of Time-Dependent Materials* 11, no. 3-4 (2007): 199-216.

51. Kong, Janet WY, Jang-Kyo Kim, and Matthew MF Yuen. "Warpage in plastic packages: effects of process conditions, geometry and materials." *IEEE transactions on electronics packaging manufacturing* 26, no. 3 (2003): 245-252.

52. Yeung, Dickson TS, and Matthew MF Yuen. "Warpage of plastic IC packages as a function of processing conditions." *Journal of Electronic Packaging* 123, no. 3 (2001): 268-272.

53. Lu, H., X. Zhang, and W. G. Knauss. "Uniaxial, shear, and Poisson relaxation and their conversion to bulk relaxation: studies on poly (methyl methacrylate)." *Polymer Engineering & Science* 37, no. 6 (1997): 1053-1064.

54. Constantinides, G., KS Ravi Chandran, F-J. Ulm, and K. J. Van Vliet. "Grid indentation analysis of composite microstructure and mechanics: Principles and validation." *Materials Science and Engineering: A* 430, no. 1 (2006): 189-202.

55. Ulm, Franz-Josef, Matthieu Vandamme, Chris Bobko, Jose Alberto Ortega, Kuangshin Tai, and Christine Ortiz. "Statistical indentation techniques for hydrated nanocomposites: concrete, bone, and shale." *Journal of the American Ceramic Society* 90, no. 9 (2007): 2677-2692.

56. Sorelli, Luca, Georgios Constantinides, Franz-Josef Ulm, and François Toutlemonde. "The nano-mechanical signature of ultra high performance concrete by statistical nanoindentation techniques." *Cement and Concrete Research* 38, no. 12 (2008): 1447-1456.

57. Zhu, Wenzhong, John J. Hughes, Nenad Bicanic, and Chris J. Pearce. "Nanoindentation mapping of mechanical properties of cement paste and natural rocks." *Materials characterization* 58, no. 11 (2007): 1189-1198.

58. Chen, J., and S. J. Bull. "On the relationship between plastic zone radius and maximum depth during nanoindentation." *Surface and Coatings Technology* 201, no. 7 (2006): 4289-4293.

59. Chen, Xi. "Computational Modeling of Indentation." in *Handbook of Nanoindentation with Biological Applications*, edited by M. Oyen, Pan Stanford Publishing, 2010.

60. Schneider, Caroline A., Wayne S. Rasband, and Kevin W. Eliceiri. "NIH Image to ImageJ: 25 years of image analysis." *Nat methods* 9, no. 7 (2012): 671-675.

# CHAPTER 4

# EVALUATION OF THE EFFECT OF THERMAL OXIDATION AND MOISTURE ON THE INTERFACIAL SHEAR STRENGTH OF UNIDIRECTIONAL IM7/BMI COMPOSITE BY FIBER PUSH-IN NANOINDENTATION

## 4.1 Introduction

Bismaleimide (BMI) composites have been used extensively for structural components in aircraft, including composite frames for turbine engines and engine exhaust washed structures due to a unique combination of high service temperature, reasonably high fracture toughness and epoxy-like processing conditions [1, 2]. BMI composites, however, are known to have very limited service life under worst-case operational conditions, due to chemical, physical and mechanical degradation under harsh environmental conditions such as temperature cycles and atmospheric humidity experienced in flight [3–5]. Failure of composites in these aggressive environments has a direct impact on operational cost and fleet readiness. For an IM7/BMI unidirectional composite after exposure to 195°C and 245°C for 2 months, we have reported its dynamic compressive behavior at high strain rates [5]. The results show that thermal oxidation leads to a significant reduction in stiffness and strength. In a follow-up work [6], the dynamic compressive experiments were conducted to determine the effect of thermal oxidation on the mechanical properties of the BMI resin at high strain rates. The resin exposed to 245°C for 1500 hours shows only slightly reduced mechanical properties, which is in stark contrast to the data reported for IM7/BMI unidirectional composite oxidized for two months at 245°C [5]. It indicates that degradation in composites is likely due to matrix shrinkage and debonding at the interface between fibers and matrix. Consequently, measuring the thermal degradation of the

neat resin is a necessary, but not sufficient step for understanding the appropriate mechanism for synergistic degradation at the fiber/matrix interface in a composite. In this paper, an investigation was made to determine the effect of thermal oxidation on the fiber/matrix interface behavior directly using push-in nanoindentation.

Composites can absorb moisture not only during the flight but also in storage. Although it has been known that moisture-induced swelling may degrade the fiber/matrix interface [4], most of literatures investigating the moisture effect in polymer composites have placed an emphasis for predicting the diffusion of moisture, and moisture concentration as a function of position and time. Much less attention is given to the degradation of fiber/matrix interface due to the long-term moisture effects [7, 8]. During the service, the moisture-saturated polymer composites can be subjected to rapid heating. If the heating is too fast for the absorbed moisture, likely in the form of vapor to escape, large internal water vapor pressures can develop, leading to void nucleation in matrix and at the fiber/matrix interface. The steam-induced delamination and blistering (referred as steam blistering effect in this paper) can potentially cause failure of the composite. This phenomenon has led to many research interests from both experimental [9, 10] and theoretical perspectives [11, 12]. While more detailed literature review can be found in [11] and the reference therein, investigations on the effect of steam blistering on the degradation of interfacial shear strength, especially for BMI composites, are very rare.

Over decades, a number of experimental techniques have been developed to evaluate the fiber/matrix interface adhesion by mechanically characterizing the interfacial shear strength (IFSS) [13]. IFSS is commonly measured using micromechanical test methods such as the single-fiber fragmentation test [14], the microbond test [15–17], the single-fiber push-out test

[18, 19], and the fiber push-in test [20–22]. Yang et al. [16] measured IFSS of thermal-oxidative degradation glass fiber-polypropylene composites by microbond test. Yu et al. [7] reported long-term moisture effects on IFSS measured by microbond test. Micrbond test utilize single fibers embedded in a matrix, which has inherent difference with actual as-processed composites. To study the environment effects such as thermal oxidation and steam blistering, it is necessary to measure IFSS on the actual composites, in which case fiber push-out and fiber push-in tests can be applied. However, the fiber push-out test requires the cumbersome preparation of very thin sample (~50 μm), and sample tends to break during the polishing very easily, which results in extremely low yield in sample preparation. Due to these reasons, the fiber push-in experiments were conducted in this investigation. To the best of our knowledge, for IM7/BMI composites, there have been no results reported on the effect of thermal oxidization and steam blistering, with an emphasis on fiber/matrix interface behavior.

In this chapter, unidirectional IM7/BMI composite was exposed to thermo-oxidation at elevated temperatures, close to and above the service temperature for 2 months. IM7/BMI laminates were also immersed in water for 2 years at room temperature. The moisture-saturated specimens were heated to 260$^{o}$C under different thermal histories, and the interfacial shear strength was characterized by fiber push-in nanoindentation. The effect of thermal oxidation and steam blistering was then investigated and discussed in detail.

## 4.2 Material and experiments

### 4.2.1 Material

The thermal oxidized unidirectional IM7/BMI composite plates were the same as those used in our work published earlier [5], thus only a brief description on specimen preparation is presented here, and more details can be found in reference [5]. The composite square plates with a nominal thickness of 2.0 mm and a side length of 150 mm, were oxidized at 195$^{o}$C (close to the service temperature of 204$^{o}$C) and at 245$^{o}$C (higher than the service temperature but lower than glass transition temperature of 270 $^{o}$C) in air, respectively for 1500 hours (about 2 months). After 1500 hours of oxidation, the central portion (at least 41 mm away from all edges) of the large composite plates were cut into small rectangular specimens using 0.3 mm thick diamond-coated saw blade under cooling by flowing water. Subsequently, the specimens were washed, cleaned and dried at 60$^{o}$C for 72 hours. Figure 4.1 shows a schematic diagram of a unidirectional IM7/BMI composite specimen prepared from a composite panel after oxidation. "$x_1$" is along the fiber direction.

To investigate the effect of steam blistering, 6 pieces of unidirectional IM7/BMI composite plates of 38.1 mm wide and 127.0 mm long were cut from composite plates with a thickness of 2.0 mm and 304.8 mm side-length, the samples were immersed in water for nearly 2 years at room temperature. The mass of each plate was weighed by a digital balance (Denver Instrument, APX-200). Before weighing, the plate specimens were removed from water, dried with clean tissues until the tissue did not absorb water.

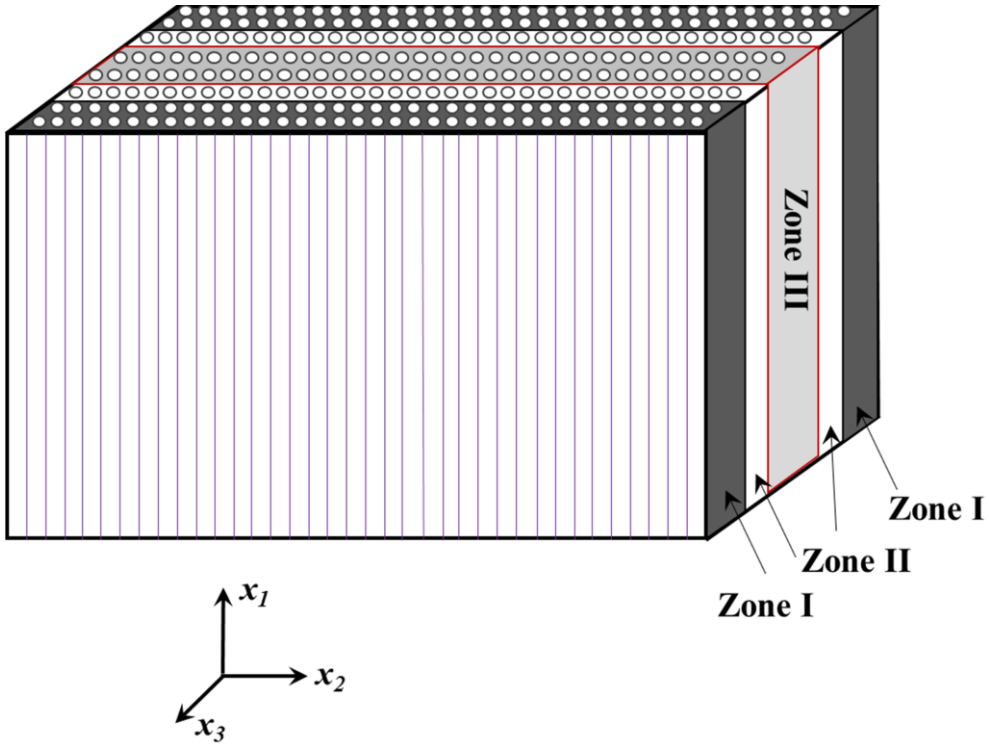


Figure 4.1. Schematic diagram of a thermally oxidized IM7/BMI unidirectional composite laminate after exposure to a high temperature. The schematic diagram shows a central portion of a larger laminate after oxidation. The oxidized composite contains three zones: Zone I (fully oxidized zone), Zone II (active reaction zone), and Zone III (unoxidized zone). A Cartesian frame is also shown, with x1 aligned with fiber direction.

The average weight gain was 0.787% in 1.5 years and no additional weight gain was detected thereafter, indicating that it took about 1.5 year to reach a water saturated state. A 0.3 mm thick diamond-coated blade saw was used to cut the specimens. After cutting, the cutting surfaces were lightly polished by #600 sandpaper to produce smooth surface. Subsequently, the specimens were washed, ultra-sonically cleaned and then placed back into water. Two heating procedures, namely sudden heating (under thermal shock) and ramp heating, were used. In the first procedure, a specimen was directly placed inside an oven preheated to 260 °C. In the second procedure, temperature was slowly ramped up to 260°C at a rate of approximately 6°C/min in a

Fisher Scientific oven LB 305745M (320°C maximum temperature with ±2°C accuracy). For heating at a ramp temperature history, it took 40 minutes to increase the temperature to 260°C at a rate of approximately 6°C/min. The final average weight loss was 0.760%. For the step heating, the wet sample was directly placed inside the oven preheated to 260°C for 5 minutes; and the average final weight loss of a specimen was 0.727%.

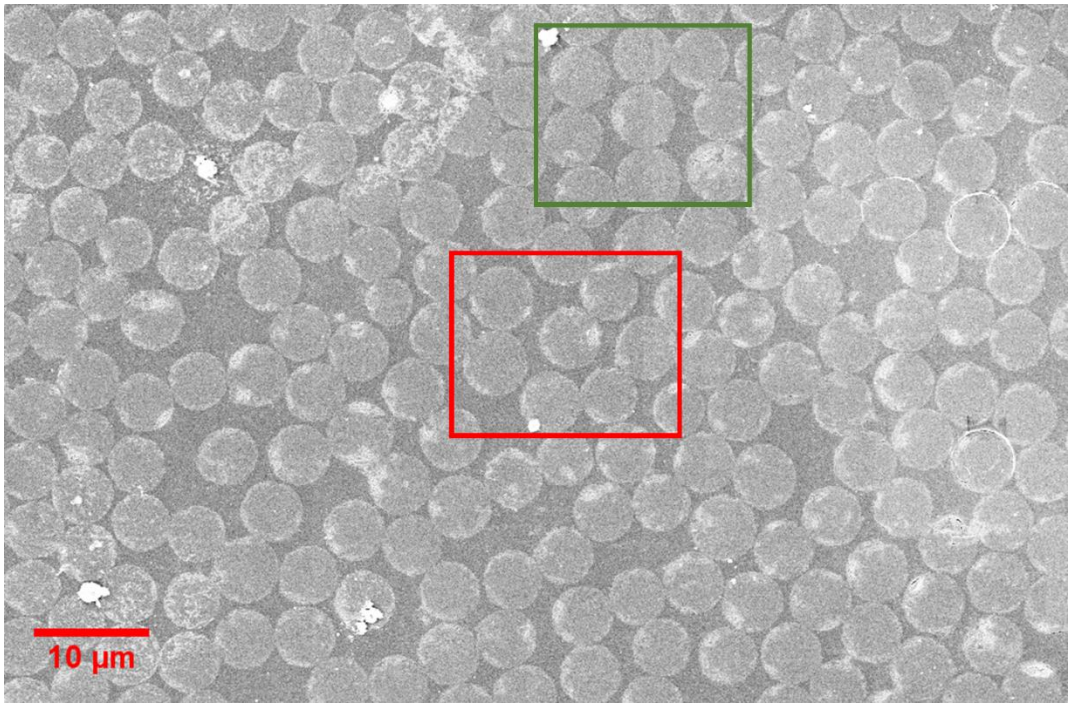


Figure 4.2. Scanning electron micrograph of a cross-section of a pristine IM7/BMI composite. The highlighted regions in the red and green boxes are used in full 3D finite element simulations (shown in Figure 4.8).

The unidirectional IM7/BMI composite specimens were prepared in six conditions, namely baseline specimens, specimens oxidized at 195°C, specimens oxidized at 245°C, wet specimens (fully saturated, and no steam blistering), saturated specimens undergoing step heating history to 260°C, and saturated specimens undergoing ramp heating history to 260°C. The composite specimens were embedded into epoxy potting material (modified Bisphenol A-Epichlorohydin

Epoxy, Allied High Tech Products, Inc.). Each potted sample was cured at room temperature for 24 hours. The cross section perpendicular to the fibers of the unidirectional composite specimens were polished first by #800 and #1200 sandpaper, respectively. The specimens were then polished by a MultiPrep$^{TM}$ system polishing machine using alumina suspension with particle size from 1 μm to 50 nm in sequence. Figure 4.2 shows a typical scanning electron microscopic (SEM) images of the cross-sectional area of baseline specimen. Most of the cross sections of the IM7 fibers were found to be in an approximately circular shape, and the plane parallel to the specimen surfaces can thus be considered to be perpendicular to the fiber. They were used for fiber push-in nanoindentation in the fiber directions.

### 4.2.2 Fiber push-in nanoindentation

In this paper, interfacial shear strength was determined by fiber push-in nanoindentation experiments [20, 21, 23]. All the fiber push-in nanoindentations were conducted on an Agilent G200 nanoindentation system. The nanoindentation system can reach a maximum indentation depth of 500 μm (0.2 nm resolution) and a maximum load of 500 mN (50 nN resolution). A flat punch tip (Micro Star Tech) of 3 μm in diameter was used in this investigation. In order to conduct nanoindentation on an IM7 carbon fiber (5 μm in diameter) at close to the center of a fiber as possible, calibration was conducted to obtain an accurate lateral position of the indenter relative to the sample surface with the use of an optical microscope on the nanoindentation system. All the fiber push-in nanoindenations were conducted at a constant loading rate of 1 mN/s. Considering the fact that the 45$^{o}$ cone angle of indenter used in this investigation, the flat punch tip will not touch the matrix if the maximum displacement is below 1 μm. In this study, the maximum load was chosen such that the maximum nanoindentation displacement was below

700 nm. Twenty-five fiber push-in nanoindentations were conducted for each preparation condition of the IM7/BMI composite specimen. During the experiment, it was found that error in positioning of the flat punch indenter was accumulated over time, making it difficult to push the target fiber right at the center. Thus, the residual indents were checked every five push-in experiments, if the nanoindentation site was off from the center by more than 1 μm, the data was disregarded and the calibration between flat punch tip and optical microscope was re-conducted. The procedure mentioned above was repeated until 25 fiber push-in nanoindentations were completed, with all the nanoindentation sites located approximately in the center of IM7 carbon fibers. Attempts were made to select target fibers that have approximately the same diameter and local fiber configurations, which best represent the overall volume fraction. Fibers selected in experiments were nearly hexagonally packed, and they were not touching the surrounding fibers.

During a fiber push-in nanoindentation experiment, the flat punch tip was pressing on an individual fiber until fiber/matrix interface debonding occurred. The applied nanoindentaion load and the resulting nanoidentation displacement were recorded. A typical push-in nanoindentation load-displacement curve follows an "S" shape [23]. The initial nonlinear region at small depths, designated as "toe" region, is the result of imperfect contact between the fiber and flat punch indenter. As the flat punch tip makes full contact with the fiber end, the resulting push-in load follows a linear relationship with the displacement, giving a contact stiffness $S_0$, representing linear elastic deformation of fiber and matrix. The end of the linear region marks with the beginning of the fiber/matrix interface failure, or debonding. A simplified shear-lag model [20–25]gives the expression for the interfacial shear strength, $\tau_0^{SL}$

$$\tau_0^{SL} = \frac{S_0 P_C}{2\pi^2 r^3 E_f} \tag{4.1}$$

where $S_0$ is the stiffness (slope) of the linear elastic region, $P_c$ is the critical load at the onset of nonlinearity, $r$ is the fiber radius, $E_f$ is the longitudinal elastic modulus of the fiber. The stiffness of the elastic region $S_0$ depends on the fiber and matrix properties, as well as the confinement from the surrounding fiber and matrix, which depends on the local fiber volume fraction. Rodríguez et al. [21] performed a series of numerical simulations, and reported that the above shear-lag model underestimated interfacial shear strength for push-in experiments conducted at the central fiber of highly-packed clusters with hexagonal symmetry, and proposed a simple relationship to provide correction. However, the relationship reported in [21] is based on fiber and matrix properties of one composite with specific compound and fiber/matrix configurations. The relationship does not necessarily hold for the IM7/BMI composite used in this investigation. Thus, for IM7/BMI composites used in this study, numerical simulations were conducted to assist the determination of interfacial shear strength.

## 4.3 Finite element model

### 4.3.1 General model

An inverse method is used to determine the interfacial shear strength from the push-in nanoindentation on the composites. To this end, finite element method (FEM) was used to simulate the fiber push-in experiments on IM7/BMI composite. The commercial software package ABAQUS V6.14 was used for the modeling. A typical three-dimensional (3D) FEM model used to simulate the fiber push-in nanoindentaions is shown in Figure 4.3. The baseline case of a 3D FEM model is simplified as one sixth of the entire 3D model to reduce the

computational time by considering the hexagonal symmetry of the fiber packing. A flat punch tip of 3 μm in diameter, which is same as the one used in experiments, is modelled as rigid.

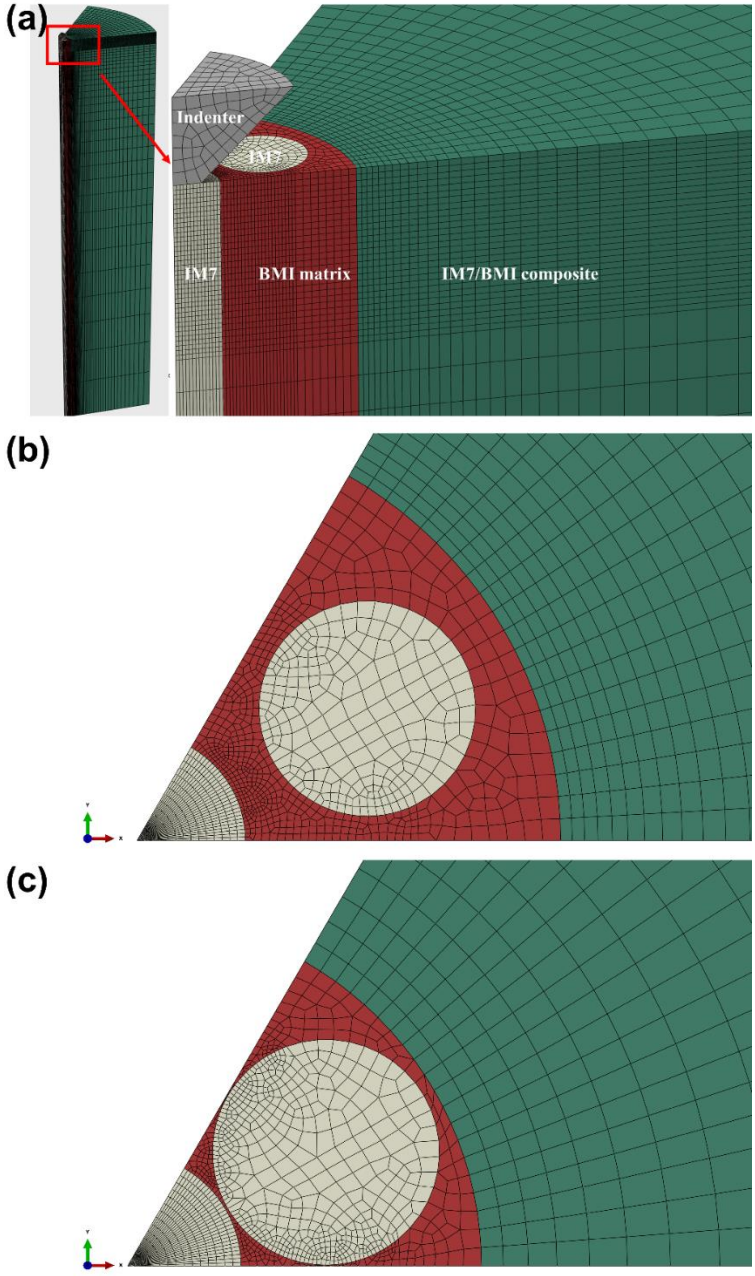


Figure 4.3. Three dimensional finite element models for nanoindentation push-in experiment for IM7/BMI composite. (a) overall geometry and FEM mesh; (b) top surface of the FEM model for pristine composite, with a local fiber volume fraction of 0.6; (c) top surface of the FEM model corresponding to a local fiber volume fraction of 0.9.

The central IM7 carbon fiber with 5 μm diameter is surrounded by six IM7 carbon fibers. Those carbon fibers are embedded in the BMI matrix and this central region is surrounded by an annular region of homogeneous material continuum with effective properties of IM7/BMI composite. The height and radius of the FEM model were selected to be 375 and 80 μm, respectively. This model size was found to be large enough to avoid sample size effect on the push-in nanoindentation load-displacement curve. The distance between the central fiber and surrounding fiber is specified such that it corresponds to a 60% fiber volume fraction. It was found that the local fiber arrangement used in this investigation agreed well with the experimental results. The validity of this assumption will be addressed in the Discussion section.

Table 4.1. Material properties used in FEM simulations

| Material property | | IM7 fiber | IM7/BMI composite | BMI matrix |
|---|---|---|---|---|
| Longitudinal modulus | $E_1$ (GPa) | 276 | 174 | 4.6 |
| Transverse modulus | $E_2$ (GPa) | 19 | 12.1 | |
| Shear modulus | $G_{12}$ (GPa) | 27 | 9.0 | |
| Poisson's ratio | $\nu_{12}$ | 0.2 | 0.36 | 0.35 |
| Poisson's ratio | $\nu_{23}$ | 0.2 | 0.45 | |
| Longitudinal CTE | $\alpha_1$ ($10^{-6}$ /°C) | -0.4 | 0.25 | 44 |
| Transverse CTE | $\alpha_2$ ($10^{-6}$ /°C) | 5.6 | 21.1 | |

The carbon fiber is modeled as a transversely isotropic and linear elastic solid, and the BMI matrix is modeled as a linear elastic isotropic solid. Material properties used in simulations were taken from previously published data [26, 27], as summarized in Table 4.1. The yield strength of BMI matrix is above 200 MPa [28], which is several times larger than the interfacial shear strength. Since the yield strength is twice as large as the interfacial shear strength, plastic deformation of the matrix was not taken into account in this investigation, assuming linear elastic response of BMI matrix will not affect the onset of nonlinearity, and the results on the interfacial

shear strength [21, 29]. In the FEM models, different parameters were considered, these include: interfacial strength, interfacial fracture energy, local fiber arrangement, curing residual stresses, and friction coefficient. The FEM model contains 117,422 linear hexahedral fully-integrated elements (C3D8) and 2,010 linear wedge fully-integrated elements (C3D6). Adaptive meshing was used, and very fine mesh was used at the fiber/matrix interface and the region underneath the flat punch indenter. The fiber/matrix interface was considered as infinitesimally thin, and a surface-based cohesive interactions were used in the model to take into account of the fiber/matrix debonding and effect of friction during fiber push-in nanoindentations. Mesh convergence studies were conducted to ensure that proper mesh refinement has been achieved.

### 4.3.2 Surface-based cohesive behavior

To model the debonding between fiber and matrix, a surface-based cohesive interaction was used and the interface was assumed to satisfy bilinear traction separation law. The undamaged and uncoupled linear elastic traction separation behavior is defined as,

$$\mathbf{t} = \begin{Bmatrix} t_n \\ t_s \\ t_t \end{Bmatrix} = \begin{bmatrix} K_{nn} & 0 & 0 \\ 0 & K_{ss} & 0 \\ 0 & 0 & K_{tt} \end{bmatrix} \begin{Bmatrix} \delta_n \\ \delta_s \\ \delta_t \end{Bmatrix} = \mathbf{K\delta} \tag{4.2}$$

where **t** is nominal traction vector and $\boldsymbol{\delta}$ is separation displacement vector. **K** is stiffness matrix. The subscripts *n*, *s*, and *t* represent normal, shear and tangential components at the fiber/matrix interface, respectively. Damage is initiated once the quadratic traction criterion is satisfied,

$$\left\{\frac{\langle t_n \rangle}{t_n^0}\right\}^2 + \left\{\frac{t_s}{t_s^0}\right\}^2 + \left\{\frac{t_t}{t_t^0}\right\}^2 = 1 \tag{4.3}$$

where $t_n^0$, $t_s^0$ and $t_t^0$ are normal, shear, and tangential interfacial strength, respectively. Brackets for $t_n$ are the Macaulay brackets, which return the argument if it is positive and give a zero if the argument is negative, since the compressive normal stresses will not open the crack [15, 21, 30]. It is noted that the fiber push-in nanoindentations only provide the values of the interfacial shear strength. In this study, the interfacial strengths in three directions are assumed equal to each other, namely $t_n^0 = t_s^0 = t_t^0 = \tau_0$. The cohesive behavior is defined to follow the linear softening damage evolution law,

$$\mathbf{t} = (1-D)\mathbf{K}\boldsymbol{\delta} \tag{4.4}$$

where D is damage parameter defined as 0 in the case of no damage and 1 at the complete failure. Additional details on the bilinear traction separation law can be found elsewhere [15].

In this investigation, a series of simulations were conducted by varying interfacial shear strength, $\tau_0$ = 40, 50, 60, 70, 80, 90 and 100 MPa; interfacial fracture energy, $G_c$ =2, 5, 10, 20, 30, 40 and 80 J/m$^2$; friction coefficient, $\mu$ = 0, 0.2, 0.4 and 0.6. To study the effect of residual stress induced in the curing process, isotropic coefficient of thermal expansion for the BMI matrix, and anisotropic coefficients of thermal expansion for IM7 fiber and IM7/BMI composite were used, with values given in Table 4.1. An initial stress state was introduced based on a cooling from the curing temperature of 227$^o$C to room temperature. The conclusions obtained from above simulations will be used to interpret the experimental data.

## 4.4 Results and discussions

### 4.4.1 Fiber push-in nanoindentation and FEM simulations: baseline specimens

Fiber push-in nanoindentations were conducted first on pristine IM7/BMI composite, and the experimental load-displacement curves are shown in Figure 4.4, from which a reasonably good reproducibility can be observed.

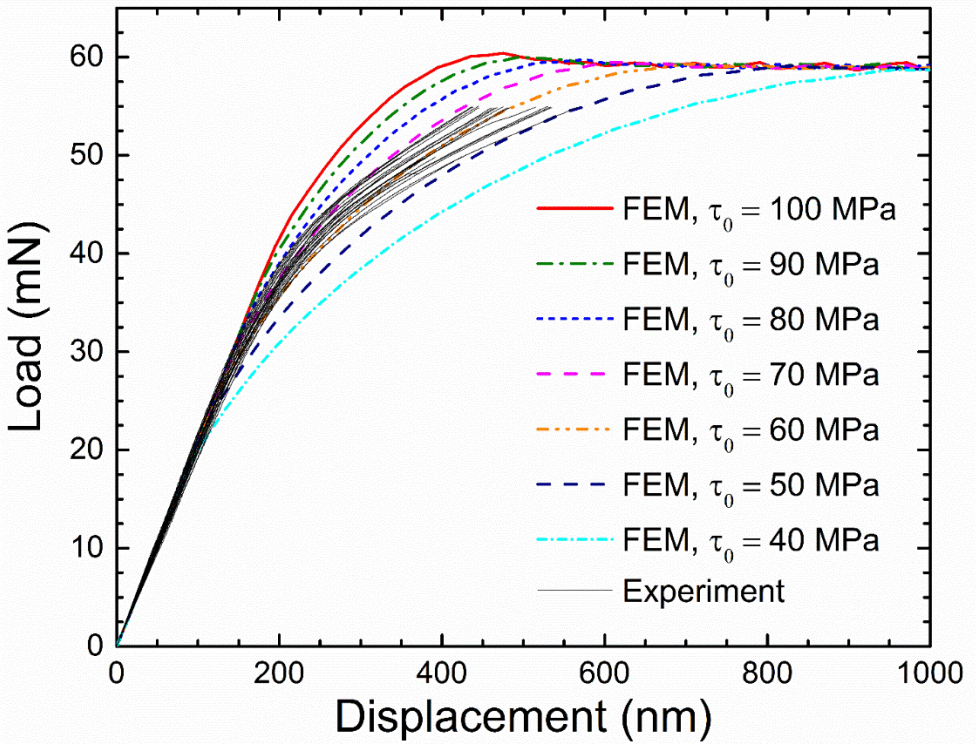


Figure 4.4. Nanoindentation push-in experimental and simulated load-displacement curves for IM7/BMI pristine specimen. Black lines represent the experimental results, other color curves are FEM simulation results with different input values for the interfacial shear strength.

The experimental load-displacement curves are also compared with simulated curves. They agree with each other reasonably well, especially in the linear region, indicating that our FEM model with a fiber volume fraction of 60%, both for overall composite, and for local region could capture the mechanical behavior of IM7/BMI composite during the fiber push-in

nanoindentations. For a detailed microscopic analysis of the load-displacement relationship, fiber push-in nanoindentations were paused at different loading stages, and unloaded. SEM micrographs of the push-in fibers were acquired to illustrate the deformation process, as shown in Figure 4.5.

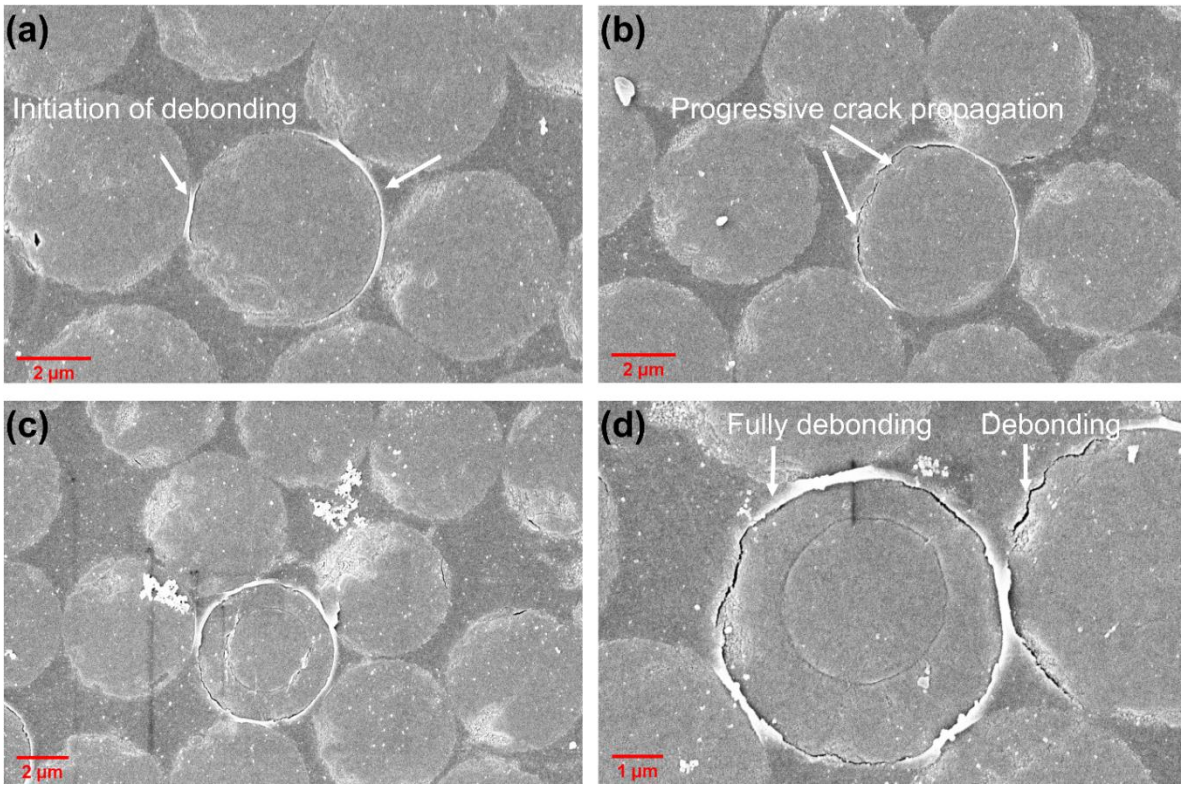


Figure 4.5. SEM images of sample surfaces after interruption at different loading stages during the fiber push-in experiments. (a) experiment paused at nearly 150 nm nanoindentation depth: initiation of fiber/matrix debonding; (b) experiment paused at approximately 250 nm nanoindentation depth: progression of the fiber/matrix debonding; (c) experiment paused at nearly 400 nm nanoindentation depth: fully fiber/matrix debonding; (d) another experiment paused at nearly 400 nm nanoindentation depth: fully fiber/matrix debonding, the debonding was also observed at a neighboring fiber.

By increasing the load, stress at the fiber/matrix interface increases. At the stage corresponding to the nanoindentation depth of approximately 150 nm (Figure 4.5(a)), there was an initiation of fiber/matrix debonding, as indicated by the white marker. As nanoindentation

depth reaches nearly 250 nm, the crack propagation resulted in a larger region of debonding between fiber and matrix, as shown in Figure 4.5(b). Finally, when the nanoindentation depth is close to 400 nm, fiber has fully debonded from the matrix, which are shown in Figure 4.5(c) and 4.5(d). SEM micrographs confirm that the indenter tip has made contact with the fiber only, it did not touch the surrounding matrix region. In some situations, partial debonding also occurred in the neighboring fibers (Figure 4.5(d)). Following this observation, cohesive interaction between neighboring fibers and BMI matrix was also included in our FEM simulations. The debonding in neighboring fibers has been successfully captured by our FEM model, the details of which will be discussed in Section 4.4.1.

In order to determine the interfacial shear strength accurately from experimental load-displacement curves, a series of FEM simulations were conducted to study the effects of interfacial shear strength, interfacial fracture energy, friction between fiber matrix, and residual stress induced in curing process. By doing so, the shear-lag model (Equation (4.1)) was examined by comparing results with FEM simulations, the comparison indicates that the shear-lag model is applicable to the experimental fiber push-in configuration of IM7/BMI composites used in this investigation. For the first set of fiber push-in simulations, friction and curing residual stresses were neglected, and all the fiber/matrix interfaces were assumed to have the identical interfacial fracture energy $G_c$ of 20 J/m$^2$. To perform a parametric sensitivity study, different interfacial shear strengths were assigned in the FEM model, which fall in the typical range of interfacial shear strength of carbon fiber reinforced polymer composites: 40, 50, 60, 70, 80, 90 and 100 MPa, respectively. The corresponding load-displacement curves predicated by FEM are shown in Figure 4.6(a), it was found that all the curves have the same initial slope,

followed by a non-linear region, and a plateau region with constant load, corresponding to the propagation of the interface crack from the upper surface, and steady-state situation of crack propagation, respectively. Further, the lower the assigned interfacial shear strength, the lower is the onset of nonlinearity. Those behaviors are very similar to those reported in reference [21]. Those results are not surprising since the initial slope is governed by the geometry configuration, and elastic properties of the fiber and matrix. The constant load at steady-state is controlled by the interface fracture energy, as shown in Figure 4.6(b).

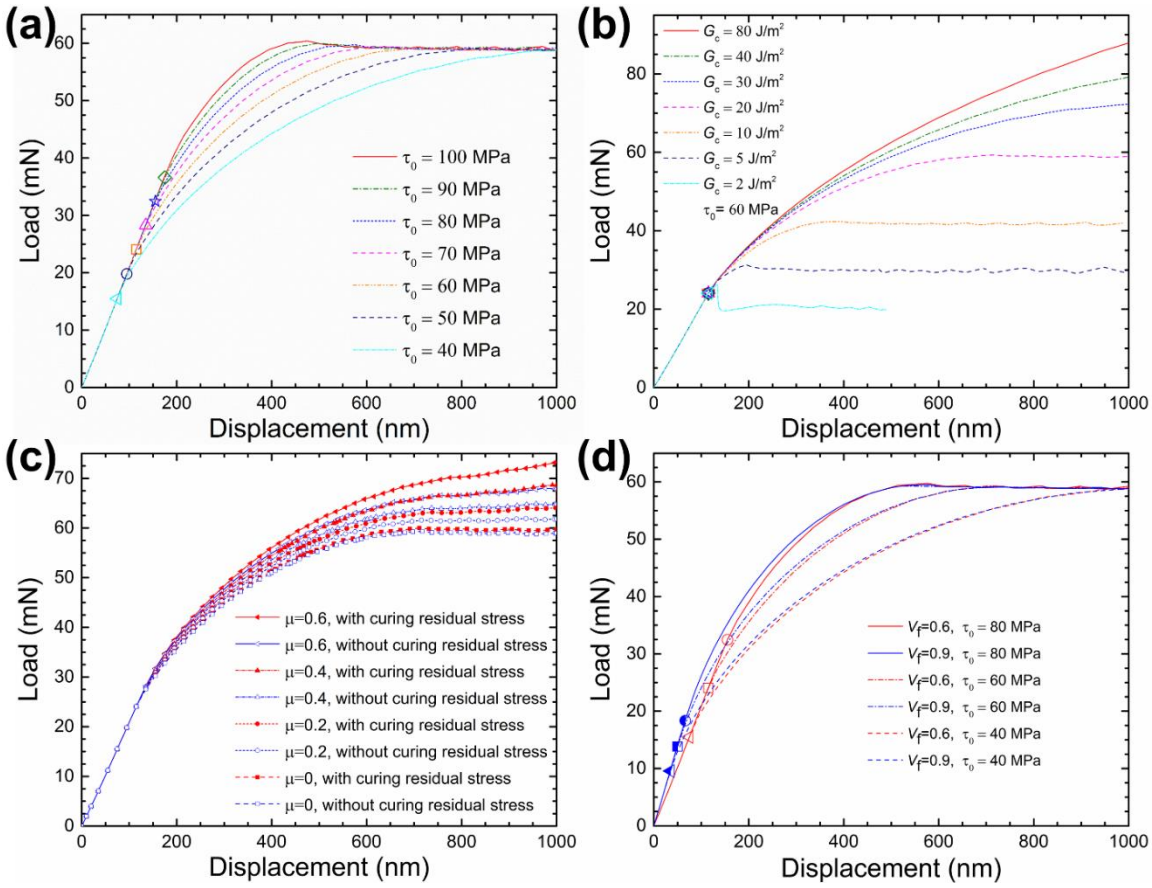


Figure 4.6. FEM simulated nanoindentation push-in load-displacement curves for pristine composite. (a) curves showing the effect of interfacial shear strength, the onset of fiber/matrix debonding is marked with different symbols; (b) effect of interfacial fracture energy; (c) effect of curing residual stress and friction coefficient; (d) effect of local fiber volume fraction.

The push-in nanoindentation load-displacement curves in Figure 4.6(b) are collected from the second series of FEM simulation by varying $G_c$ =2, 5, 10, 20, 30, 40 and 80 J/m$^2$ while interfacial shear strength was kept at a constant value of 60 MPa. It was concluded that the values for interfacial fracture energy did not affect the onset of nonlinearity, thus confirmed that the calculation of interfacial shear strength is independent of interfacial fracture energy, for fiber push-in nanoindentations [21].

Effects of friction and curing residual stresses were also examined. FEM simulations were conducted with different values of the friction coefficient, namely 0, 0.2, 0.4, and 0.6. An initial stress state was introduced based on a cooling from the curing temperature of 227$^o$C to room temperature. In this set of FEM simulations, interfacial shear strength and interfacial fracture energy were given as 60 MPa and 20 J/m$^2$, respectively. The corresponding load-displacement curves are shown in Figure 4.6(c). It was found that friction increases the interfacial shear resistance [21,31], and residual compressive stresses due to curing further enhance the interfacial shear resistance which is due to the added friction resulting from the residual compressive stresses. The onset of nonlinearity is not affected by the existence of friction [21] and thermal residual stresses [31], thus the calculation of interfacial shear strength are unlikely to be affected by these parameters.

FEM simulations have also been conducted to take into account of the configuration with extremely high local fiber volume fraction ($V_f$ = 0.9). Figure 4.3(c) shows the FEM mesh of the top surface, this model is very similar to the configuration in reference [21]. For this case, interfacial fracture energy was assumed to be 20 J/m$^2$ and interfacial shear strength was 40, 60, and 80 MPa, respectively. It was assumed that no friction and residual thermal stress exist. Load-

displacement curves obtained from the above model are compared with baseline FEM model ($V_f$ = 0.6), shown in Figure 4.6(d). The initial stiffness increases as local fiber volume fraction becomes larger, while the critical load at onset of nonlinearity turns to be lower.

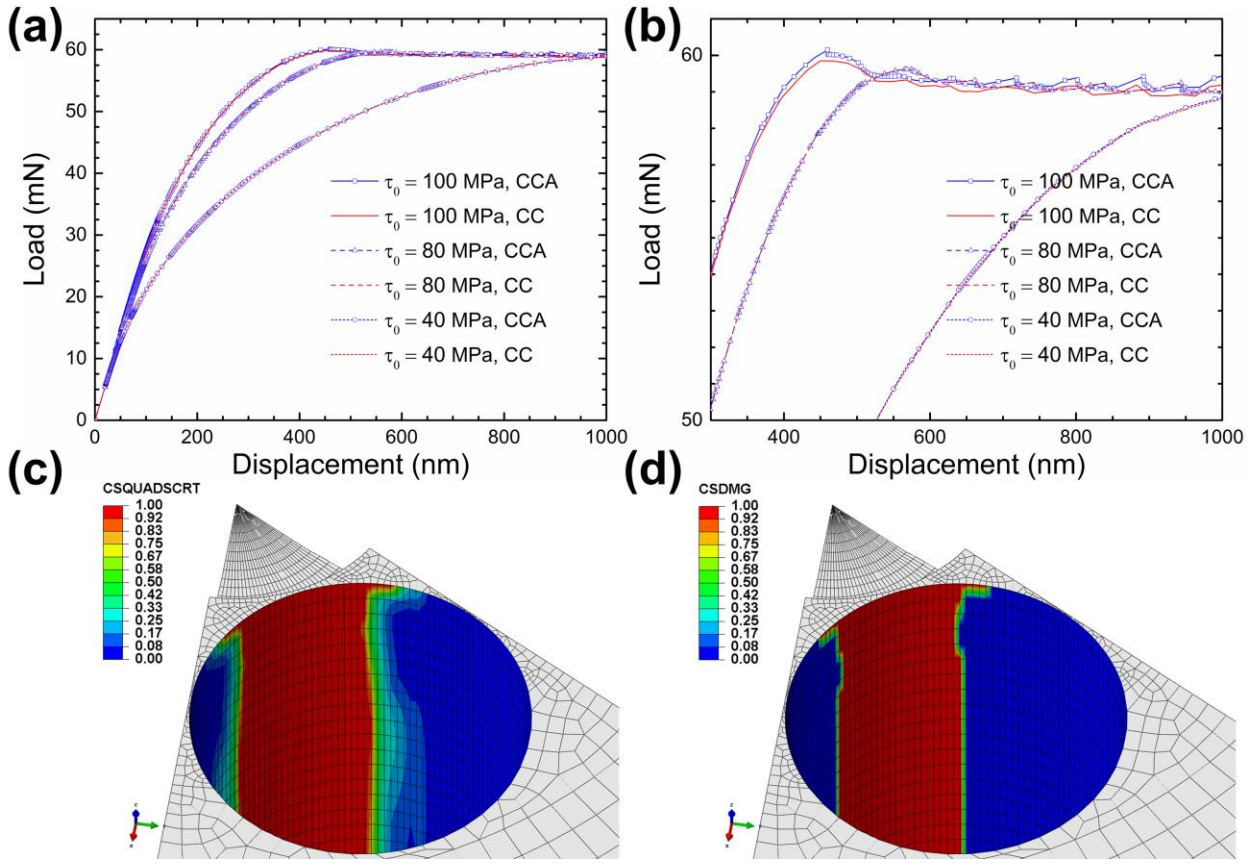


Figure 4.7. FEM simulation of fiber push-in experiments, cohesive interfaces were considered between neighboring fibers and matrix (a) nanoindentation push-in load-displacement curves. "CCA" represents "Cohesive surfaces exist in Central fiber/matrix and Adjunct fiber/matrix region. "CC" represents "Cohesive surface only exist in central fiber/matrix region; (b) enlarged figure of nanoindentation push-in load-displacement curve, a slight difference is observed in the steady-state crack propagation region; (c) contour plot of the damage initiation parameter (CSQUADSCRT) of the cohesive surface; the red region corresponds to the initiation of fiber/matrix debonding; (d) damage parameter of the cohesive surface; the red region represents fully-debonded fiber/matrix interface. The fiber/matrix debonding region in the neighboring fiber is the closest to the central fiber.

In addition, debonding of neighboring fiber was investigated by using this model. The interfacial shear strength was set to be 40, 80, and 100 MPa, respectively, and interface fracture

energy was assumed to be 20 J/m$^2$. The interface properties were assumed to be the same for both cohesive surfaces, namely central fiber/matrix and neighboring fiber/matrix.

As shown in Figure 4.7(a) and (b), cohesive interaction between neighboring fiber and matrix has negligible effect on the overall load-displacement relationships. Differences are only observed in the steady-state crack propagation region. Figure 4.7(c) and (d) indicate that initiation and propagation of debonding at the neighboring fiber/matrix interface does occur. And debonding occurs in the region close to the central fiber. This agrees with the observation in experimental results shown in Figure 4.5(d).

Equation (4.1) was used to calculate the interfacial shear strength. It was found that the shear-lag model underestimates the local constraint effect for $V_f$ = 0.9 FEM model, and an empirical correction coefficient 1.32 could be used for such a model, with the consideration of IM7/BMI composite material properties. The empirical correction coefficient is not universal, which depends on geometry configuration and constitutive behavior of fiber, matrix and surrounding composites. More details can be found in the work by Rodríguez et al. [21], where the correction coefficient is 1.92 in their case.

In this investigation, $V_f$ = 0.6 FEM model was chosen as the baseline model for the following reasons: First, in contrast to $V_f$ = 0.9 FEM model, for FEM model with $V_f$ = 0.6, interfacial shear strength calculated by Equation (4.1) is very close to the interface strength assigned. This is due to the fact that, the shear-lag model works very well if the surrounding fiber constraint is not high, such as in the extreme cases such as $V_f$ = 0.9 model, detailed discussions can be found in [22]. Second, as shown in Figure 4.5, a very good agreement has been reached between experiments and $V_f$ = 0.6 FEM model, particularly on the initial stiffness part. In the

case where Equation (4.1) was not used, inverse method can be used to allow the simulation curves to agree with experimental data, by adjusting the interface properties. Such an inverse calculation method will not be possible for $V_f$ = 0.9 model, since the initial slope of load-displacement curve will not change by modifying interface properties only. For the work reported in [21]. There are non-negligible differences between experimental load-displacement curves with their simulation curves, in the sense of initial slope and critical load. We should be very careful to apply an empirical correction coefficient, which obtained from one initial stiffness, to load-displacement curve with the other clearly distinguishable initial stiffness. Last, but not least, a perfect hexagonal packing, i.e, symmetric and highly packed central fiber can be found. However, the surrounding fiber of this 7 fibers may not be hexagonally-packed, and in some cases, matrix rich region can be found near to a hexagonal-packed fiber, which can be seen in Figure 4.2 and Figure 4.5. The constraint effect from surrounding fiber and matrix is not that strong, compared with $V_f$ = 0.9 FEM simulation, where only the central fiber and 6 fibers around it was considered, while the surrounding area is assumed to behave as bulk composite. Recently, Jäger et al. [30] and Naya et al. [32] used a larger RVE, taken from cross-section micrograph, in their FEM simulation, which is very promising. When such a RVE is used, the fiber volume fraction in the central part (multiple fibers surrounded by matrix) is comparable to fiber volume fraction of the bulk composites, which supports our model assuming local fiber volume fraction equals the global. In our case, computational cost is much smaller in comparison with references [30, 32].

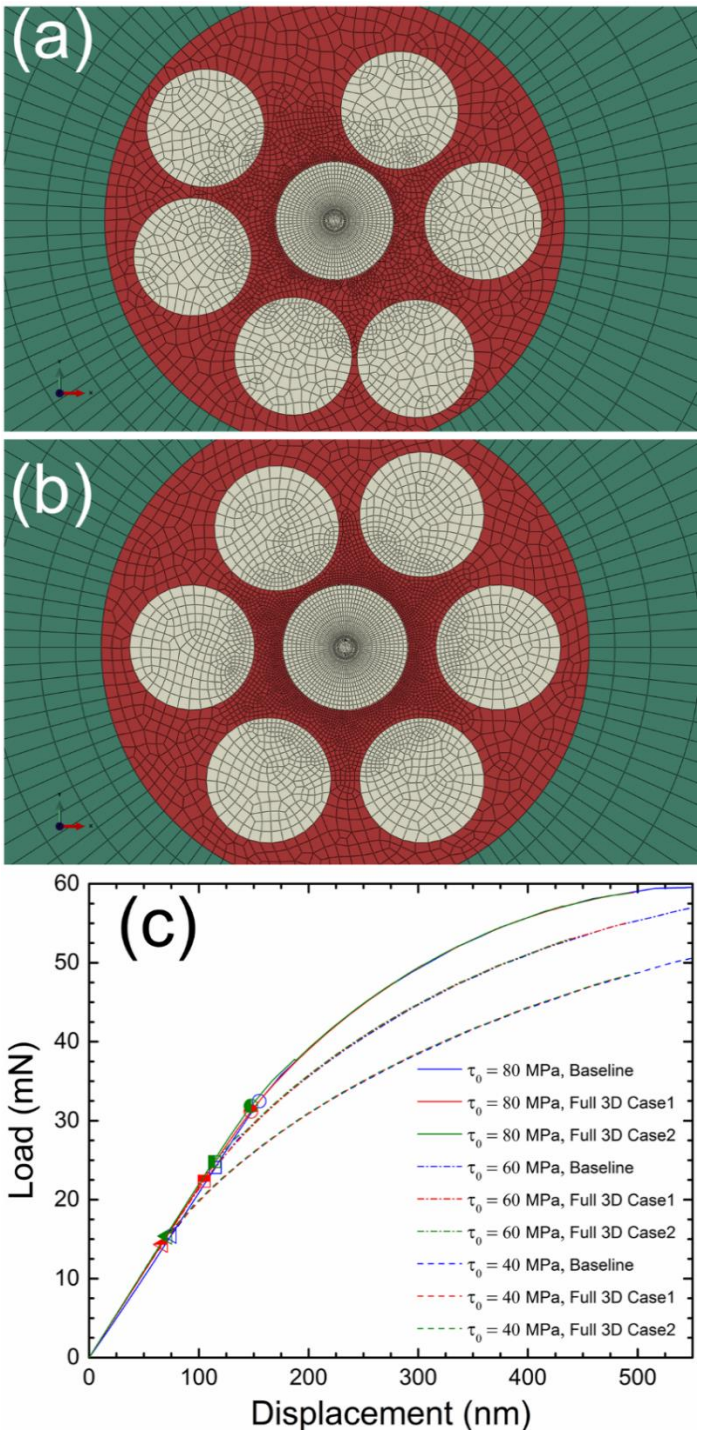


Figure 4.8. FEM simulation results for fiber push-in experiments. Full 3D FEM models were considered. (a) local fiber arrangement of Case 1, surface information was taken from the red box in Figure 4.2; (b) local fiber arrangement of Case 2, surface information was taken from green box in Figure 4.2; (c) push-in load-displacement curves.

It was observed that there was slight uncertainty of the experimental load-displacement curves, the reason of which can be different surrounding environment of the analyzed fibers and/or deviation of nanoindentation site from the center of the IM7 fiber. The baseline FEM model is established under the assumption of symmetric loading and geometry. Two non-symmetric configurations were simulated, as shown in Figure 4.8. The entire 3D model was simulated due to the loss of symmetry. There are 425,650 and 435,351 elements, respectively. The fiber arrangement in central region was taken from the SEM micrograph, as shown in Figure 4.2. It is seen that both the critical load and the slope of nanoindentation load-displacement curves of these two configurations are slightly different with the baseline FEM model. However, IFSS calculated by shear-lag model is fairly accurate.

Due to the reasons mentioned above, it was determined to use the $V_f$ = 0.6 model as the baseline simulation model. Even though there is a slight underestimation of interfacial shear strength for some extreme cases, namely a lot of fibers highly hexagonally-packed together, the interfacial shear strength obtained in this study can be at least considered as lower bound. In our experiments, such extreme situation was not easy to find, and nanoindentation made on those area, if any, has been avoided.

### 4.4.2 Effect of thermal oxidation on interfacial shear strength

After isothermal oxidation for 1500 h, the composite specimens show larger reduction in interfacial shear strength for specimens isothermally oxidized at 245ºC than at 195ºC. The specimens were cut from areas of the oxidized plates far away from the edges [5], oxidation occurs primarily in the thickness or the $x_3$- direction. After thermal oxidation, composites have three oxidative zones from the surface to the core of a unidirectional composite specimen [5, 33],

namely zone I, zone II and zone III, as schematically shown in Figure 4.1. The oxygen diffused from atmosphere into the surface layer, to form oxidized and damaged zone I; zone II is the active oxidation process zone, which is the transition region between zone I and zone III. Zone III is in the central core region occupied by the unoxidized material if it has not yet been oxidized. After 2 months of exposure to elevated temperatures, the outer layers of composite panel have been thermally oxidized while the interior was thermally aged but not necessarily oxidized. In this study, fiber push-in experiments were conducted on zone I (close to the edge of the specimens) and zone III (close to the center of the specimens).

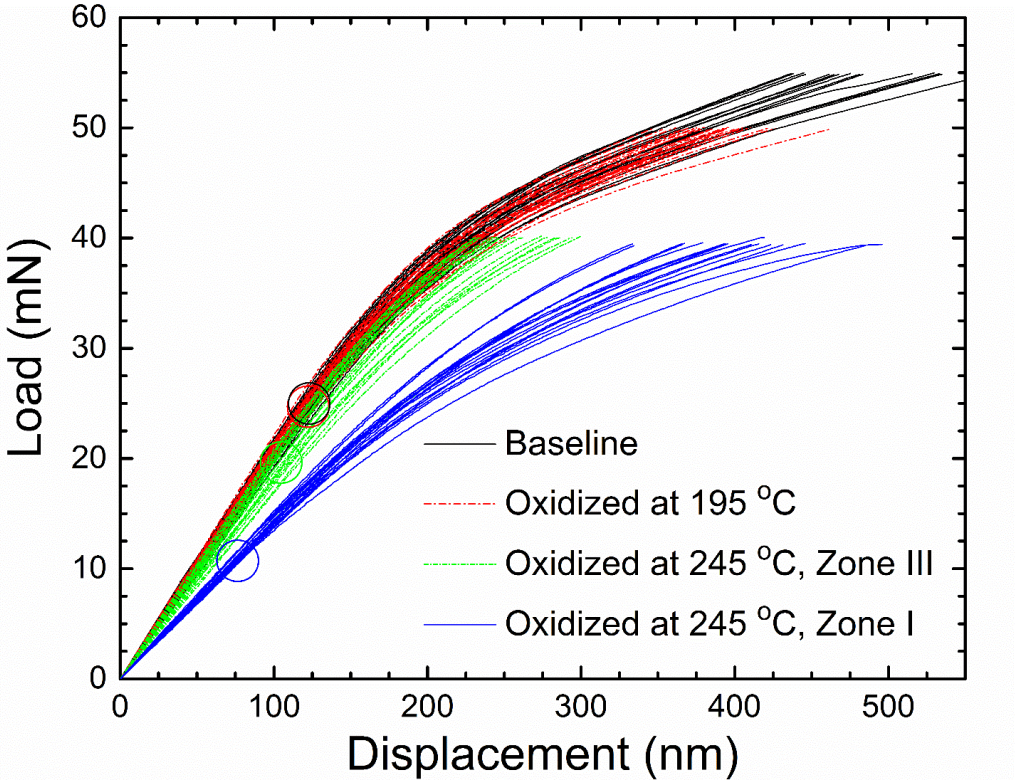


Figure 4.9. Experimentally obtained nanoindentation push-in load-displacement curves for unidirectional IM7/BMI specimen: effect of thermal oxidation.

Figure 4.9 shows the load-displacement curves from fiber push-in nanoindentations on different specimens, namely baseline specimens, specimens oxidized at 195°C, specimens

oxidized at 245°C. In Figure 4.9, the initial nonlinear region was removed, in other words, toe correction at small displacement has been made on these curves following the ASTM Standard D695-15. Equation (4.1) uses linear slope of the load-displacement curve, which is outside of the toe region. Figure 4.9 indicates that for specimens oxidized at 195°C, the change of slope and critical load is not apparent, while for specimens oxidized at 245 °C, both the linear slope and critical load reduce significantly, in particular, in zone I.

To determine the interfacial shear strength, it is important to accurately identify the critical load at the onset of nonlinearity of load-displacement curve. The algorithm for seeking the onset of nonlinearity is briefly introduced here: the data point between 0 mN and 10 mN was used to obtain an average slope. For every data point thereafter, the slope was compared with the average slope. If the difference was larger than 0.5%, the data point was marked as a "suspect" point. The 30 data points following the "suspect" point were checked to compare the slope with the average slope. If any slope from these 30 data points was same or within 0.5% difference compared with the average slope, the "suspect" point was disregard. Otherwise, the "suspect" point is marked as "critical" point. The above iteration continues until the critical load is found. The algorithm mentioned above has been implemented in a MATLAB routine. The MATLAB routine was checked and verified with FEM simulations curve to ensure its accuracy, then it was applied to experimental load-displacement curve to determine the critical load.

The interfacial shear strength determined by fiber push-in nanoindentations is summarized in Table 4.2. After oxidation for 1500 h at 195ºC, the interfacial shear strength shows almost negligible reduction (1.4 % only) compared with baseline, indicating good durability at a service temperature of 195ºC for IM7/BMI composites. After oxidation for 1500 h at 245ºC, the

interfacial shear strength in zone III shows a reduction of 18.7% compared with baseline data, while the interfacial shear strength in zone I shows a very significant reduction of 64.7%, compared with baseline. It indicates that significant reduced durability at a temperature that is 40$^{o}$C higher than the service temperature (204$^{o}$C) for IM7/BMI composites. The degradation in interfacial strength concur and provide direct evidence of the marked reduction in compressive stiffness and strength of the composites reported earlier [5].

Table 4.2. Summary of interfacial shear strength of IM7/BMI composite in different conditions.

| Samples | Interfacial shear strength (MPa) | Percentage of reduction (%) |
|---|---|---|
| Baseline | 58.3 $\pm$ 3.7 | -- |
| Oxidized at 195 $^{o}$C | 57.5 $\pm$ 4.9 | 1.4 |
| Oxidized at 245 $^{o}$C, Zone III | 47.4 $\pm$ 4.3 | 18.7 |
| Oxidized at 245 $^{o}$C, Zone I | 20.6 $\pm$ 3.5 | 64.7 |
| Water immersion for 2 year | 56.7 $\pm$ 2.9 | 2.7 |
| Ramp heating | 57.1 $\pm$ 3.7 | 2.1 |
| Step heating | 47.7 $\pm$ 2.8 | 18.2 |

### 4.4.3 Effect of steam blistering on interfacial shear strength

Figure 4.10 shows the load-displacement curves of fiber push-in nanoindentations on different type of specimens, namely baseline specimens, water-immersed specimens, ramp heating, step heating. It is observed that load-displacement curves obtain from the water-immersed specimens and ramp heating specimens are comparable with baseline, while load-displacement curves obtained from step heating specimens show reduction in both initial slope and critical load. The interfacial shear strength determined by fiber push-in nanoindentations is summarized in Table 4.2. It is found that there is a negligible reduction in interfacial shear strength of both water-immersed specimens and ramp heating specimens, compared with baseline data. A significant reduction (18.2%) in interfacial shear strength is found in step heating specimens, compared with

baseline. It indicates that the fiber/matrix interface of IM7/BMI composites can sustain long-term moisture exposure without appreciable degradation in interfacial shear strength. It also indicates that slow heating will simply dry the IM7/BMI composites while rapid heating may result in large internal water vapor pressures, leading to void nucleation in matrix and at the fiber/matrix interface, which reduces the fiber/matrix interface strength. The degradation at the interface makes it easier for the initiation and propagation of microcracks, which can potentially lead to global failure of the structural components in aircraft.

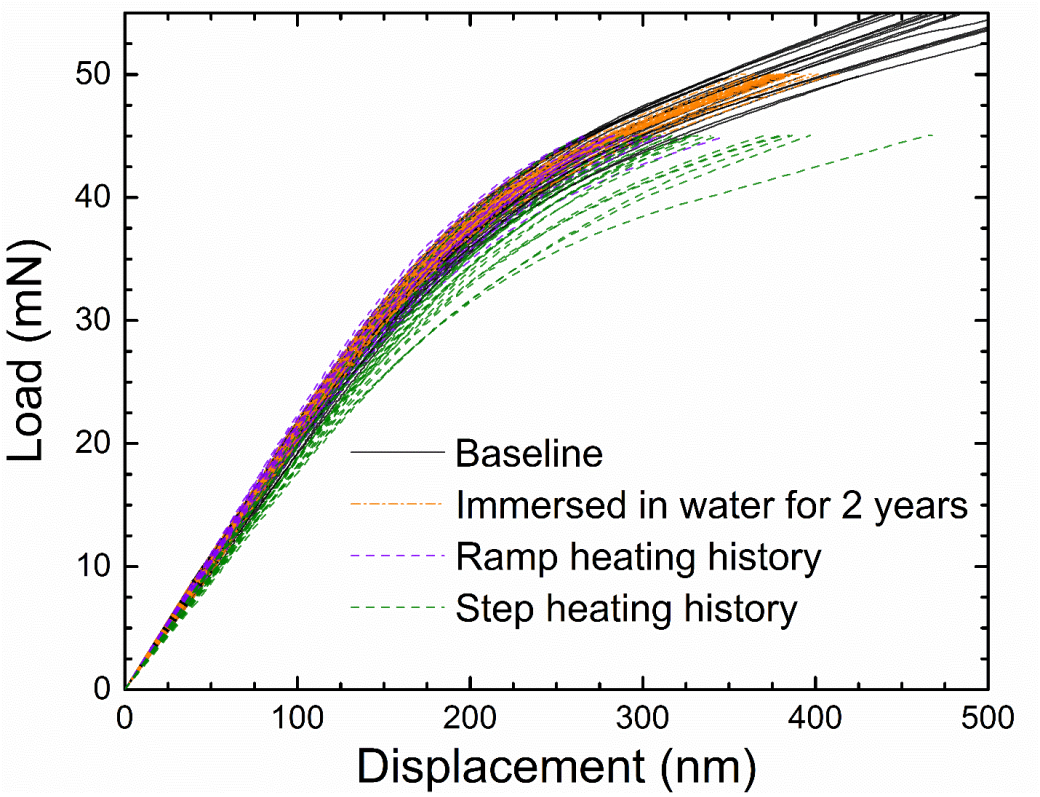


Figure 4.10. Experimentally obtained nanoindentation push-in load-displacement curves for unidirectional IM7/BMI composite specimen: effect of steam blistering.

The degradation at the interface was also confirmed by SEM micrographs of IM7/BMI composite specimens, as shown in Figure 4.11. Figure 4.11 (a) and (b) were acquired in zone I

which is the fully oxidized region of IM7/BMI specimens oxidized at 245°C. It was observed that microcracks or initiation of debonding exist extensively at fiber/matrix interface, which correlate with the degradation of interface strength. Figure 4.11(c) and (d) show the typical surface of IM7/BMI specimens under step heating history. For some of the fibers, microcracks are clearly observed at the fiber/matrix interface, which confirms the previous hypothesis mentioned in last paragraph.

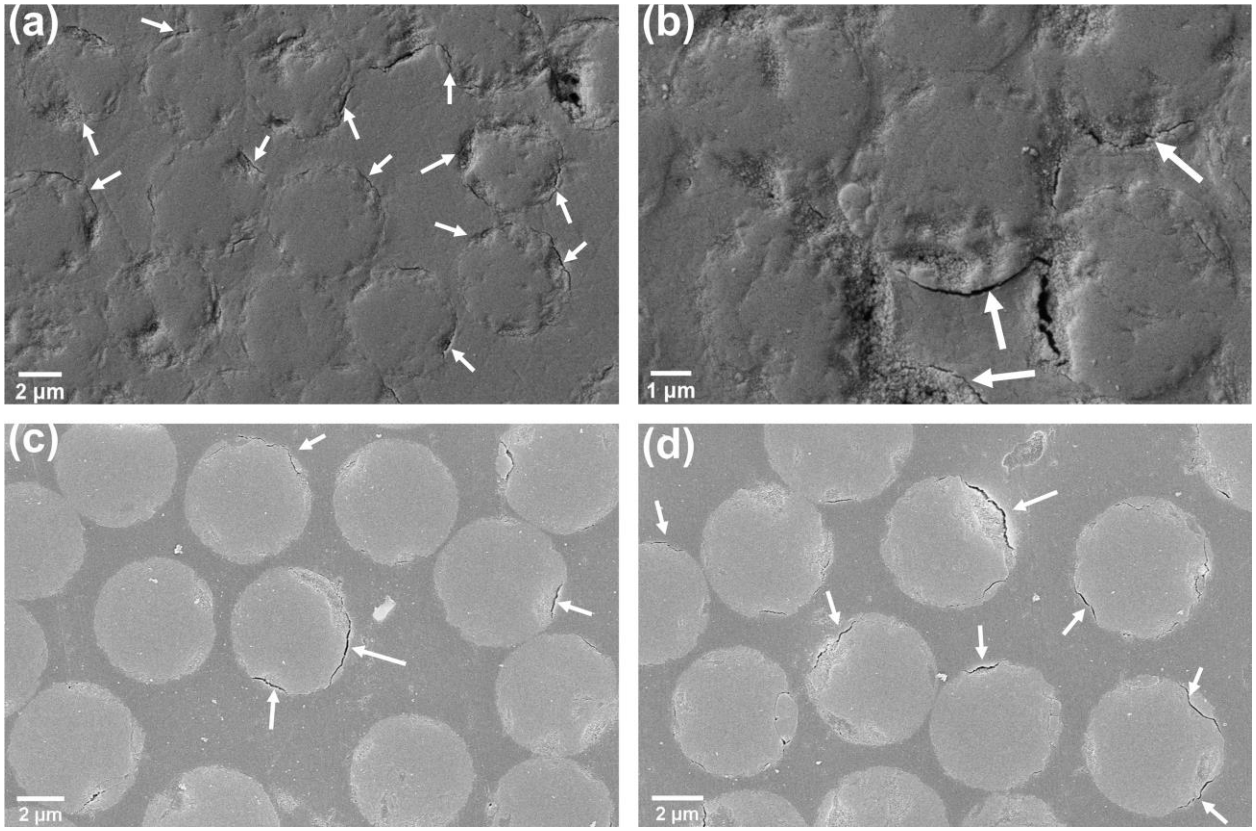


Figure 4.11. Typical SEM micrographs of IM7/BMI unidirectional composite sample surfaces. The white arrows point to the pre-existing initial cracks at the fiber/matrix interface (a) thermally oxidized zone at 245°C, fully oxidized region (Zone I); (b) enlarged view of thermally oxidized zone at 245°C, Zone I; (c) one region formed after a step heating history; (d) another region after a step heating history.

## 4.5 Conclusions

Fiber push-in experiments were conducted to evaluate the effects of thermal oxidation and steam blistering on the interface behavior of IM7/BMI unidirectional composite. Systematical FEM simulations with appropriate geometric configuration have been performed to validate and justify the fiber-push in experiments. Parametric study shows that lower-bound interfacial shear strength can be determined by shear-lag model, regardless of the interfacial fracture energy, residual stresses due to curing process, and friction between fiber and matrix. FEM simulations agree reasonably well with the fiber push-in nanoindentations for baseline specimens. For composite specimens isothermally oxidized at 195$^{o}$C for 2 months, the degradation in interfacial shear strength was found to be negligible. For composite specimens isothermally oxidized at 245$^{o}$C for 2 months, significant degradation was found in interfacial shear strength, namely 18.7% reduction in central unoxidized zone III and 64.7% reduction in oxidized and damaged zone I, respectively. Those results provide direct evidence that extensive oxidative degradation of fiber/matrix interface strength, resulting in easier fiber/matrix debonding and crack growth, is the primary cause of the eventual dynamic compressive failure observed in prior studies. For composite specimens immersed in water for 2 years, the degradation in interfacial shear strength was found to be negligible, indicating a reasonably good moisture resistance of IM7/BMI composites. For the composite specimens immersed in water for 2 years, two temperature histories were involved to study the effect of steam blistering. It was conclude that ramp heating at a rate of nearly 6°C/min was a slow drying procedure with negligible reduction in interface strength, while specimens subjected to a sudden heating was found to have an 18.2% degradation in interface strength. In this investigation, it is evident that extensive thermal oxidation and steam

blistering degrade the fiber/matrix bonding, which makes it easier to initiate and propagate microcracks along the interface, potentially leading to global failure of the structural components in aircraft.

## 4.6 Reference


1. Morgan, Roger J., Robert J. Jurek, Anna Yen, and Tom Donnellan. "Toughening procedures, processing and performance of bismaleimide-carbon fibre composites." *Polymer* 34, no. 4 (1993): 835-842.

2. Morgan, Roger J., E. Eugene Shin, Boris Rosenberg, and Ann Jurek. "Characterization of the cure reactions of bismaleimide composite matrices." *Polymer* 38, no. 3 (1997): 639-646.

3. Drukker, E., A. K. Green, and G. Marom. "Mechanical and chemical consequences of through thickness thermal gradients in polyimide matrix composite materials." *Composites Part A: Applied Science and Manufacturing* 34, no. 2 (2003): 125-133.

4. Ju, Jaehyung, and Roger J. Morgan. "Characterization of microcrack development in BMI-carbon fiber composite under stress and thermal cycling." *Journal of composite materials* 38, no. 22 (2004): 2007-2024.

5. Luo, Huiyang, Samit Roy, and Hongbing Lu. "Dynamic compressive behavior of unidirectional IM7/5250-4 laminate after thermal oxidation." *Composites Science and Technology* 72, no. 2 (2012): 159-166.

6. Luo, Huiyang, Guoqiang Lu, Samit Roy, and Hongbing Lu. "Characterization of the viscoelastic behavior of bismaleimide resin before and after exposure to high temperatures." *Mechanics of Time-Dependent Materials* 17, no. 3 (2013): 369-399.

7. Yu, Bin, Zhenyu Jiang, and Jinglei Yang. "Long-term moisture effects on the interfacial shear strength between surface treated carbon fiber and epoxy matrix." *Composites Part A: Applied Science and Manufacturing* 78 (2015): 311-317.

8. Bradley, W. L., and T. S. Grant. "The effect of the moisture absorption on the interfacial strength of polymeric matrix composites." *Journal of Materials Science* 30, no. 21 (1995): 5537-5542.

9. Czabaj, Michael W., Alan Zehnder, and Kathy C. Chuang. "Blistering of moisture saturated graphite/polyimide composites due to rapid heating." *Journal of Composite Materials* 43, no. 2 (2008) 153-174.

10. Czabaj, Michael W., Alan T. Zehnder, and Chung-Yuen Hui. "Delamination of moisture

saturated graphite/polyimide composites due to rapid heating." *Composites Part B: Engineering* 41, no. 7 (2010): 568-577.

11. Hui, Chung-Yuen, Vijayanand Muralidharan, and Michael O. Thompson. "Steam pressure induced in crack-like cavities in moisture saturated polymer matrix composites during rapid heating." *International journal of solids and structures* 42, no. 3 (2005): 1055-1072.

12. Hui, Chung-Yuen, Vijayanand Muralidharan, and Michael O. Thompson. "Steam pressure induced in crack-like cavities in moisture saturated polymer matrix composites during rapid heating." *International journal of solids and structures* 42, no. 3 (2005): 1055-1072.

13. Zhandarov, Serge, and Edith Mäder. "Characterization of fiber/matrix interface strength: applicability of different tests, approaches and parameters." *Composites Science and Technology* 65, no. 1 (2005): 149-160.

14. Kelly, A., and amd WR Tyson. "Tensile properties of fibre-reinforced metals: copper/tungsten and copper/molybdenum." *Journal of the Mechanics and Physics of Solids* 13, no. 6 (1965): 329in1339-338in2350.

15. Minnicino, Michael A., and Michael H. Santare. "Modeling the progressive damage of the microdroplet test using contact surfaces with cohesive behavior." *Composites science and technology* 72, no. 16 (2012): 2024-2031.

16. Yang, Liu, J. L. Thomason, and W. Zhu. "The influence of thermo-oxidative degradation on the measured interface strength of glass fibre-polypropylene." *Composites Part A: Applied Science and Manufacturing* 42, no. 10 (2011): 1293-1300.

17. Yang, Liu, and J. L. Thomason. "Development and application of micromechanical techniques for characterising interfacial shear strength in fibre-thermoplastic composites." *Polymer Testing* 31, no. 7 (2012): 895-903.

18. Zhang, Lifeng, Chengzu Ren, Changling Zhou, Hongzhao Xu, and Xinmin Jin. "Single fiber push-out characterization of interfacial mechanical properties in unidirectional CVI-C/SiC composites by the nano-indentation technique." *Applied Surface Science* 357 (2015): 1427-1433.

19. Mueller, W. M., J. Moosburger-Will, M. G. R. Sause, and S. Horn. "Microscopic analysis of single-fiber push-out tests on ceramic matrix composites performed with Berkovich and flat-end indenter and evaluation of interfacial fracture toughness." *Journal of the European Ceramic Society* 33, no. 2 (2013): 441-451.

20. Zidi, Mondher, Luc Carpentier, Antoine Chateauminois, and François Sidoroff. "Quantitative analysis of the micro-indentation behaviour of fibre-reinforced composites: development and validation of an analytical model." *Composites science and technology* 60, no. 3 (2000): 429-437.

21. Rodríguez, M., Jon M. Molina-Aldareguía, C. González, and J. LLorca. "A methodology to measure the interface shear strength by means of the fiber push-in test." *Composites Science and Technology* 72, no. 15 (2012): 1924-1932.

22. Molina-Aldareguía, Jon M., M. Rodriguez, C. González, and J. LLorca. "An experimental and numerical study of the influence of local effects on the application of the fibre push-in test." *Philosophical Magazine* 91, no. 7-9 (2011): 1293-1307.

23. Medina, Carlos, Jon M. Molina-Aldareguía, Carlos González, Manuel F. Melendrez, Paulo Flores, and Javier LLorca. "Comparison of push-in and push-out tests for measuring interfacial shear strength in nano-reinforced composite materials." *Journal of Composite Materials* (2015): 0021998315595115.

24. Mandell, J. F., J. H. Chen, and F. J. McGarry. "A microdebonding test for in situ assessment of fibre/matrix bond strength in composite materials." *International Journal of Adhesion and Adhesives* 1, no. 1 (1980): 40-44.

25. Marshall, David B., and W. C. Oliver. "Measurement of Interfacial Mechanical Properties in Fiber-Reinforced Ceramic Composites." *Journal of the American Ceramic Society* 70, no. 8 (1987): 542-548.

26. Andrews, E. W., and M. R. Garnich. "Stresses around fiber ends at free and embedded ply edges." *Composites Science and Technology* 68, no. 15 (2008): 3352-3357.

27. Craven, R., S. Pindoria, and R. Olsson. "Finite element study of compressively loaded fibres fractured during impact." *Composites Science and Technology* 69, no. 5 (2009): 586-593.

28. Buckley, C. P., P. J. Dooling, J. Harding, and C. Ruiz. "Deformation of thermosetting resins at impact rates of strain. Part 2: constitutive model with rejuvenation." *Journal of the Mechanics and Physics of Solids* 52, no. 10 (2004): 2355-2377.

29. Xu, Qiang, Weiming Tao, Shaoxing Qu, and Qingda Yang. "A cohesive zone model for the elevated temperature interfacial debonding and frictional sliding behavior." *Composites Science and Technology* 110 (2015): 45-52.

30. Jäger, J., M. G. R. Sause, F. Burkert, J. Moosburger-Will, M. Greisel, and S. Horn. "Influence of plastic deformation on single-fiber push-out tests of carbon fiber reinforced epoxy resin." *Composites Part A: Applied Science and Manufacturing* 71 (2015): 157-167.

31. Esqué-de los Ojos, D., R. Ghisleni, A. Battisti, G. Mohanty, J. Michler, J. Sort, and A. J. Brunner. "Understanding the mechanical behavior of fiber/matrix interfaces during push-in tests by means of finite element simulations and a cohesive zone model." *Computational Materials Science* 117 (2016): 330-337.

32. Naya, F., C. González, C. S. Lopes, S. Van der Veen, and F. Pons. "Computational micromechanics of the transverse and shear behavior of unidirectional fiber reinforced polymers including environmental effects." *Composites Part A: Applied Science and Manufacturing* 92 (2017): 146-157.

33. Pochiraju, K. V., G. P. Tandon, and G. A. Schoeppner. "Evolution of stress and deformations in high-temperature polymer matrix composites during thermo-oxidative aging." *Mechanics of Time-Dependent Materials* 12, no. 1 (2008): 45-68.

# CHAPTER 5

# CARBON NANOTUBE SHEET SCROLLED FIBER COMPOSITE FOR ENHANCEMENT IN INTERFACIAL SHEAR STRENGTH

## 5.1 Introduction

Fiber reinforced polymer matrix composites have found increasing applications in such areas as aerospace, automotive, wind farms, offshore drilling, sports, and construction. In these composites failure manifests in one of the four primary modes: fiber microbuckling in compression, fiber/matrix interfacial debonding, fiber fracture (or fragmentation), and matrix cracking. Load transfer has to take place through the interface between the fiber and polymer matrix, and the matrix is primarily responsible for shear load transfer. The stiffness and transverse strength of fiber reinforced composites depends on the behavior at the interface with a thickness on the order of 100 nm or less. Swadener et al. [1] determined that the failure or the delamination of a glass fiber occurs in the matrix 3 nm away from the fiber surface. Similar behavior has also been observed in Single Wall Carbon Nanotube (SWNT)/nanocomposites. Ding et al. [2] observed that a few nanometers of polycarbonate remains wrapped around a SWNT when the SWNT is pulled out of the polycarbonate matrix during fracture. In order to increase the strength of composites, it is critical to improve the interfacial mechanical properties through modification of the polymer matrix, fibers and/or the interface.

The high tensile strength of fiber reinforced polymer matrix composites (PMC) is mainly derived from the high strength of the carbon (or glass) fibers embedded in the matrix. Fibers typically have high strength in tension. However, their compressive strength is generally much lower due to the fact that under compression, the fibers tend to fail through micro-buckling (or

kinking) well before compressive fracture occurs. Also, fiber misalignment and presence of voids during manufacturing processes contribute to a further reduction in compressive strength. In fact, the overall compressive strength of a PMC is only about 50% of the tensile strength, and hence there is potential for significant improvement. Further, the mechanical load transfer in carbon fiber composites is often limited by the strength of the interface between fiber and matrix. In recent years considerable effort has been directed towards increase the strength of matrix by introducing nanofillers to the matrix to make nanocomposites [3,4], or to increase the interfacial strength using carbon nanotubes (CNTs) grafted on carbon fibers in the radial directions [5-16]. The improvement in interfacial strength, however, is generally not significant, and CNT grafting often results in a reduction in the properties of the carbon fiber.

In this chapter, we will take a different approach. We propose to use CNT sheet to spiral-wrap around an individual carbon fiber. While the CNT sheet scrolled on the carbon fiber has the potential to enhance mechanical, thermal, and electrical properties, this project focuses on investigating the enhancement of mechanical properties of the fiber/matrix interphase that directly influences the fiber/matrix debond strength and compressive strength of the composite. The CNT sheet drawn from MWNT forest is meso-porous with high specific surface area [17-21], consequently very small amount of CNT sheet in weight can be used to wrap around large volume of carbon fibers. Upon impregnation in a polymer, the wrapped CNT sheet is impregnated in the polymer to form nanocomposites, thereby modifying the polymer matrix near a carbon fiber due to the high volume fraction of well-aligned CNT in the matrix, and mechanical interlocking.

## 5.2 Nanoscale fabrication of MWNT scrolled carbon fiber composite

Under proper conditions, MWNT forests will exhibit special properties to allow it to be drawn into a continuous, high quality sheet.

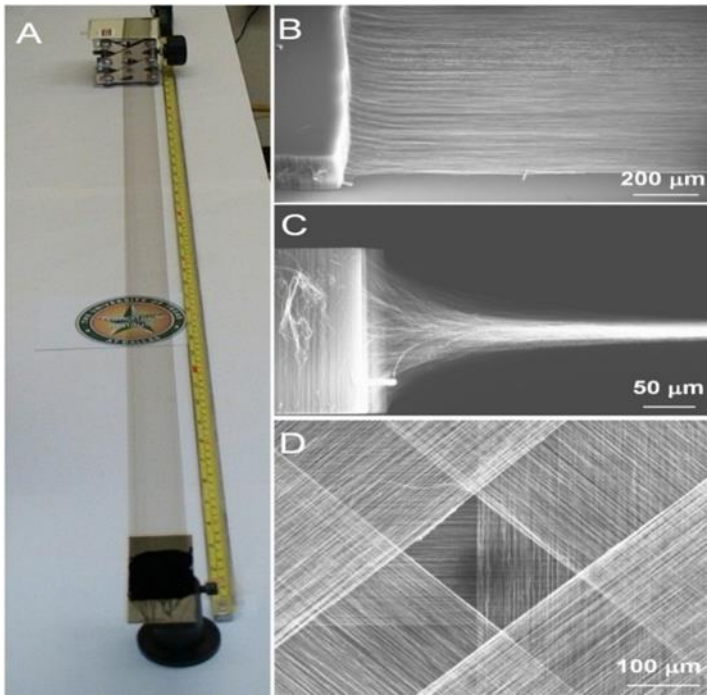


Figure 5.1. MWNT forest conversion into sheets and assemblies of those sheets. (a) Photograph of a 3.4-cm-wide, meter-long MWNT sheet. (b) SEM image of a MWNT forest being drawn into a sheet. (c) SEM micrograph showing the cooperative 90º rotation of MWNTs in a forest to form a sheet. (d) SEM micrograph of a two-dimensionally re-reinforced structure fabricated by overlaying four nanotube sheets with a 45º shift in orientation between successive sheets [17].

Figure 5.1(a) shows a self-supporting 3.4 cm wide, 1 meter long MWNT sheet hand drawn from a nanotube forest. Figure 5.1(b) shows the SEM micrograph of a MWNT forest being drawn into a MWNT sheet. Figure 5.1(c) shows a SEM micrograph of the cooperative 90-rotation view of MWNTs in a forest to form a sheet. The nanotube sheets can also be oriented and laminated as shown in Figure 5.1(d). We have observed that the drawability of the MWNT depends strongly on the degree of MWNT alignment in a forest. MWNT forest with volumetric

MWNT density of 23 mg/cm$^3$ is not drawable, while a MWNT forest with volumetric density of 39 mg/cm$^3$ is drawable. Higher volumetric MWNT densities yield better aligned and more drawable forests. Liquid densified MWNT sheet shows tensile strength of 450 MPa. The CNT sheet drawn from CNT forest is an aerogel with a mass density of near 1.0 mg/cm$^3$ and an internal surface area near 500 m$^2$/g. Densification of MWNT aerogel sheet in a liquid leads to formation of MWNT xerogel sheet with density of 1.5 mg/ cm$^3$, which still has low density and high internal surface area.

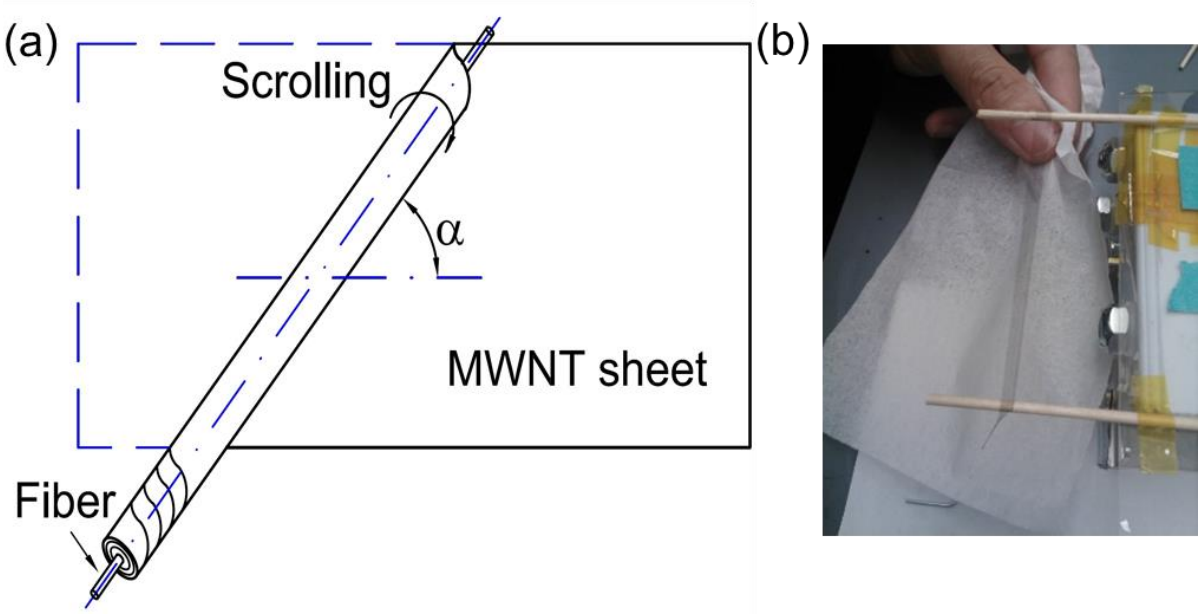


Figure 5.2. (a) A schematic diagram showing a MWNT scrolling a carbon fiber. Drawing is not to scale, (b) MWNT sheet used in experiments.

Figure 5.2(a) shows a schematic diagram of a MWNT sheet being wrapped circumferentially on a carbon fiber at a wrapping angle α. The MWNT wrapped carbon fiber is then embedded into a polymer matrix. The inner ply of the MWNT sheet adheres to the carbon fiber via Van der Waals forces. Figure 5.2(b) shows the actual pulled MWNT sheet before warping. Figure 5.3 shows sized fibers after MWNT scrolling following the scheme in Figure

5.2(a). 0, 30 and 45$^{o}$ wrap bias angle was used for this case. The effect of bias angle on interfacial shear strength will be investigated.

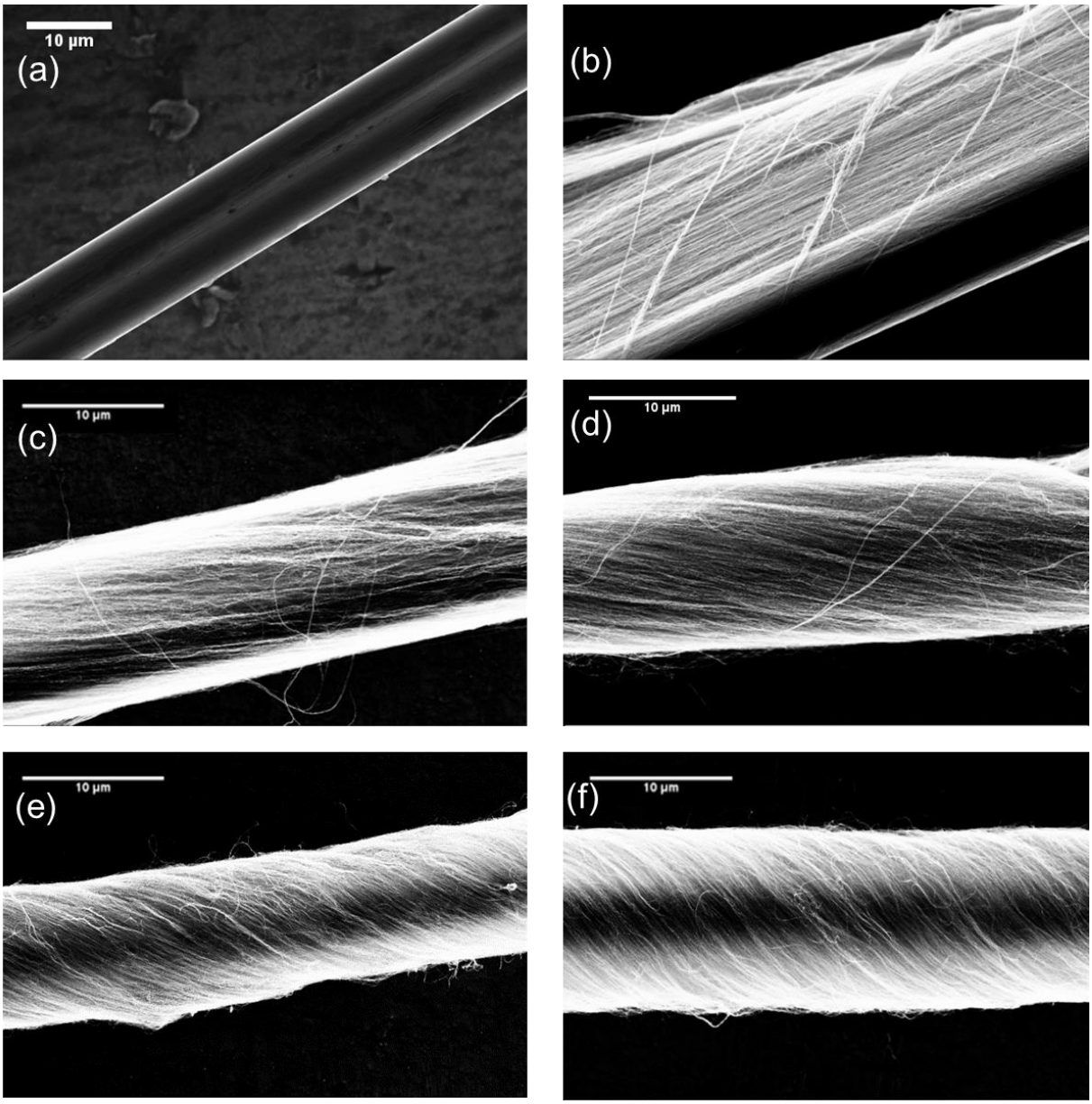


Figure 5.3. The same magnification was used in all SEM micrographs. (a) A segment of the single carbon fiber, (b) a segment of the single carbon fiber with 0$^{o}$ warp bias angle, (c) a segment of the single carbon fiber with 30$^{o}$ bias angle (d) another segment of the same single carbon fiber with MWNT plies scrolled around it. (e) A segment of the single carbon fiber with 45$^{o}$ warp bias angle, (f) another segment of the same single carbon fiber with 45$^{o}$ warp bias angle.

Different segments of the same carbon fiber with and without MWNT sheet overwrap are shown. The same magnification was used in both SEM micrographs. As can be seen, MWNT sheet wraps very well around the single carbon fiber, giving a very uniform diameter. It is noted that at this magnification, SEM micrograph cannot resolve the meso-pores. The large number of scrolled MWNT plies has increased the fiber diameter by nearly 150%. For practical applications, a small number of CNT plies may be used to wrap a carbon fiber, so that the diameter change is insignificant. Consequently, this technique is not anticipated to reduce the carbon fiber volume fraction significantly.

The approach mentioned above has been working very well for preparation of "modal" single fiber composite. In order to prepare a specimen with multiple fibers, which is more comparable with the realistic polymer based composites such as IM7/BMI used in chapter 4. False twisting method has been applied to wrap MWNT onto carbon fiber bundle, as schematically shown in Figure 5.4.

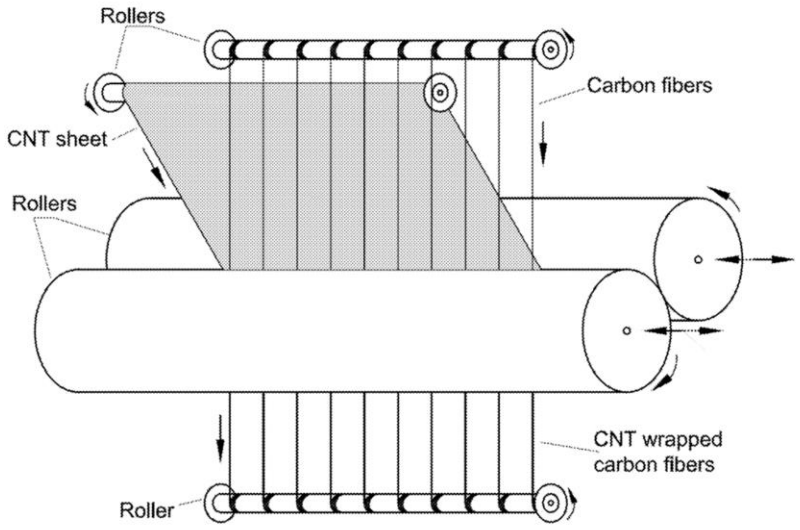


Figure 5.4. Schematic diagram showing a MWNT scrolling a carbon fiber bundle by false-twisting process [22].

Figure 5.5 shows the SEM images of MWNT wrapped carbon fiber bundles prepared by false-twisting method. It can be observed that the MWNT is well aligned with fiber direction, corresponding to a bias angle of $0^o$. It is noted that at this magnification, SEM micrograph cannot resolve the meso-pores.

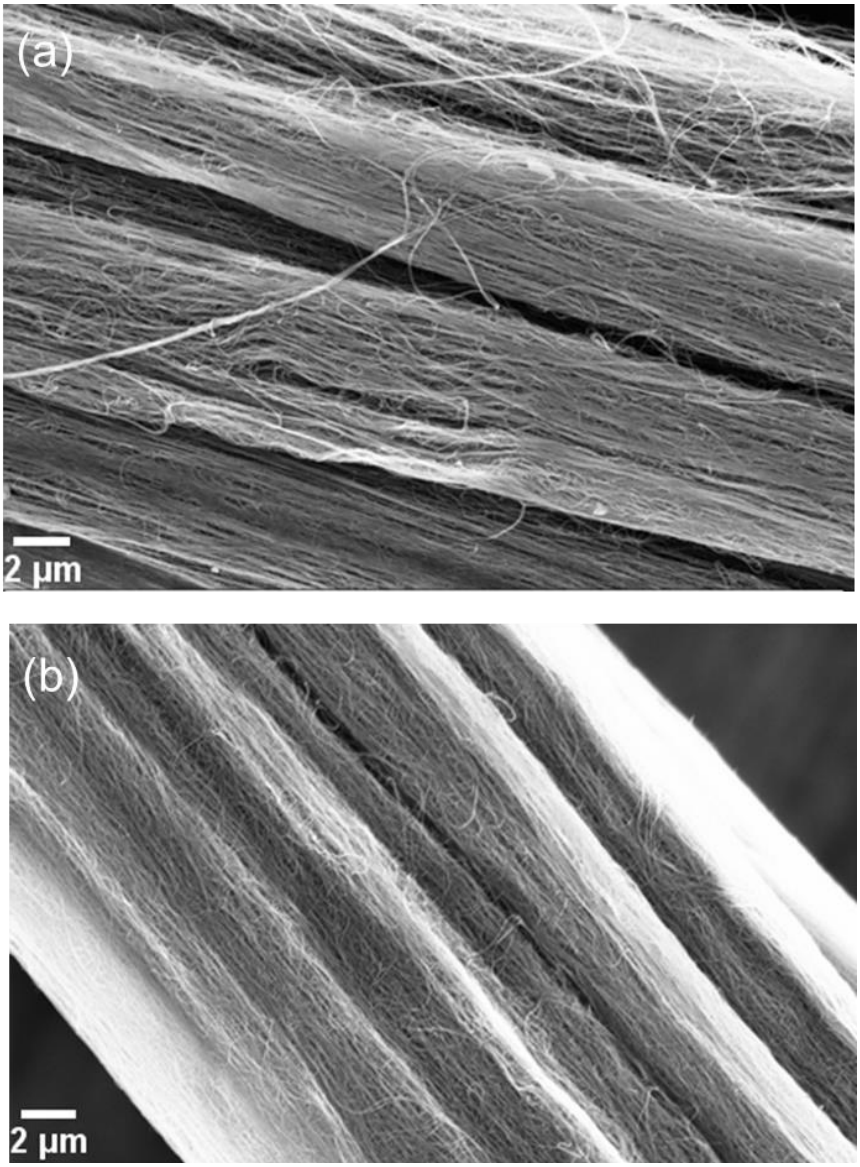


Figure 5.5. (a) SEM micrographs showing carbon fiber bundle with each fiber wrapped by MWNT. (b) SEM micrographs in a larger magnification.

## 5.3 Interphase stiffness and enhancement mechanism

It is well known that both the fiber and the MWNT can modify the polymer properties near the interface. The confinement provided by the fiber and the MWNT will modify the properties in these cases. Figure 5.6 shows the surface topography measured by AFM of the exposed profile of the baseline and MWNT scrolled carbon fiber embedded in polymer matrix. It can be observed that there is an apparent interphase region in Figure 5.6(b). The mismatch in the wear behavior and hence the susceptibility toward interfacial weakness is dramatically reduced by the scrolling of carbon nanotube around the fiber.

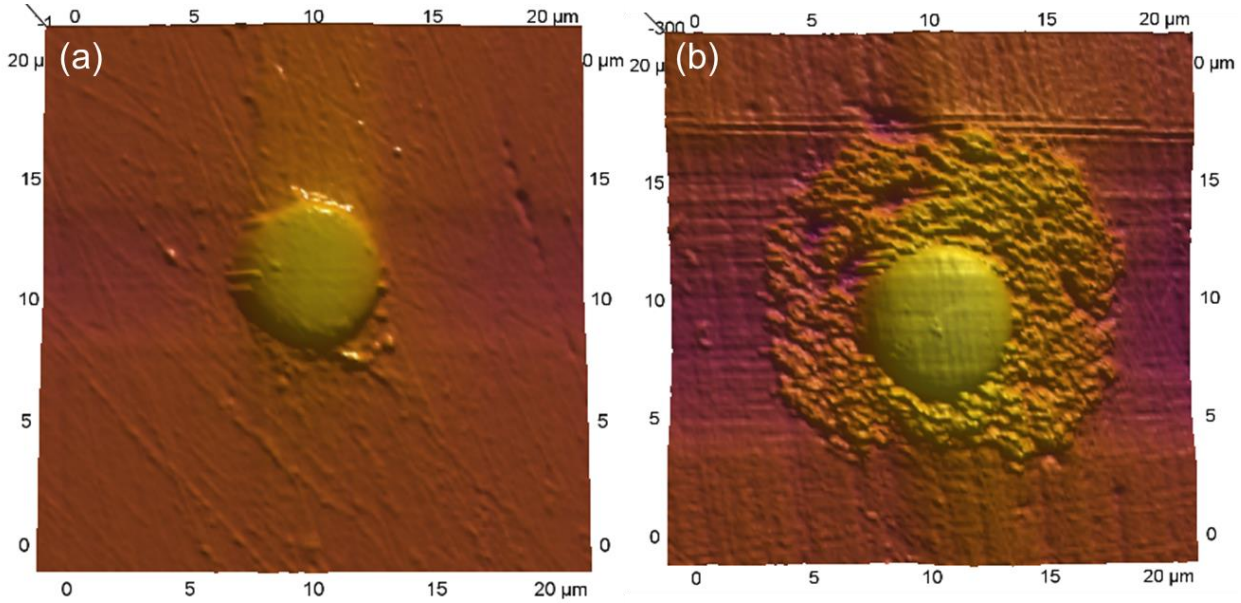


Figure 5.6. Surface topography measured by atomic force microscopy of (a) carbon fiber embedded in polymer matrix, (b) MWNT scrolled carbon fiber embedded in polymer matrix.

In this study, nanoindentation was conducted to determine the properties of the polymer at the interface. Modulus scanning using a cube corner nanoindenter tip was conducted on baseline specimen (IM7 carbon fiber embedded in Epon 862 matrix) and IM7 wrapped by MWNT (bias angle : $0^o$ and $45^o$). The same Agilent G200 nanoindentation system was used, and the maximum

nanoindentation depth was about 200 nm. The distance between two nanoindentation sites was selected to be 1.5 μm, which is large enough to ensure there is no residual stress effect from the neighboring nanoindentation. Figure 5.7 shows typical experimental results. It is very distinguishable when indenter made contact on fiber, fiber/matrix interphase or matrix only, as shown in Figure 5.7(b).

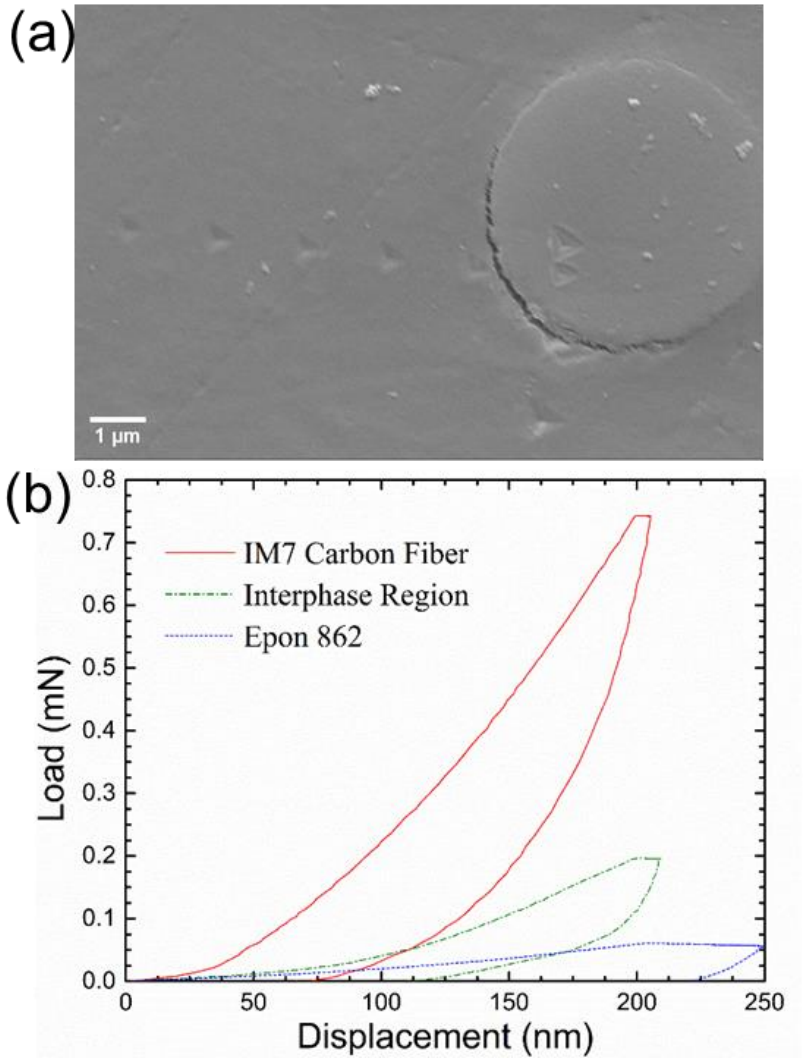


Figure 5.7. Modulus scanning to determine the interphase stiffness (a) residual nanoindents showing the line scan (b) typical nanoindentation load-displacement curves when nanoindentation was made on different target.

For each type of specimen, five fibers were scanned to ensure enough information for statistical analysis. The results are shown in Figure 5.8. For nanoindentation made on fiber, there is not much difference in modulus for three cases. However, indentation modulus in the interphase region near to fiber is 4.33 ± 0.05 GPa, 13.2 ± 1.2 GPa, 24.7 ± 3.2 GPa for baseline, IM7 wrapped by MWNT with a 45° bias angle, and IM7 wrapped by MWNT with a 0° bias angle, respectively, which clearly shows the improvement in interphase stiffness. Indentation modulus in the interphase region near to epoxy is 3.76 ± 0.08 GPa, 7.8 ± 2.6 GPa, 16.1 ± 0.9 GPa for baseline, IM7 wrapped by MWNT with a 45° bias angle, and IM7 wrapped by MWNT with a 0° bias angle, respectively.

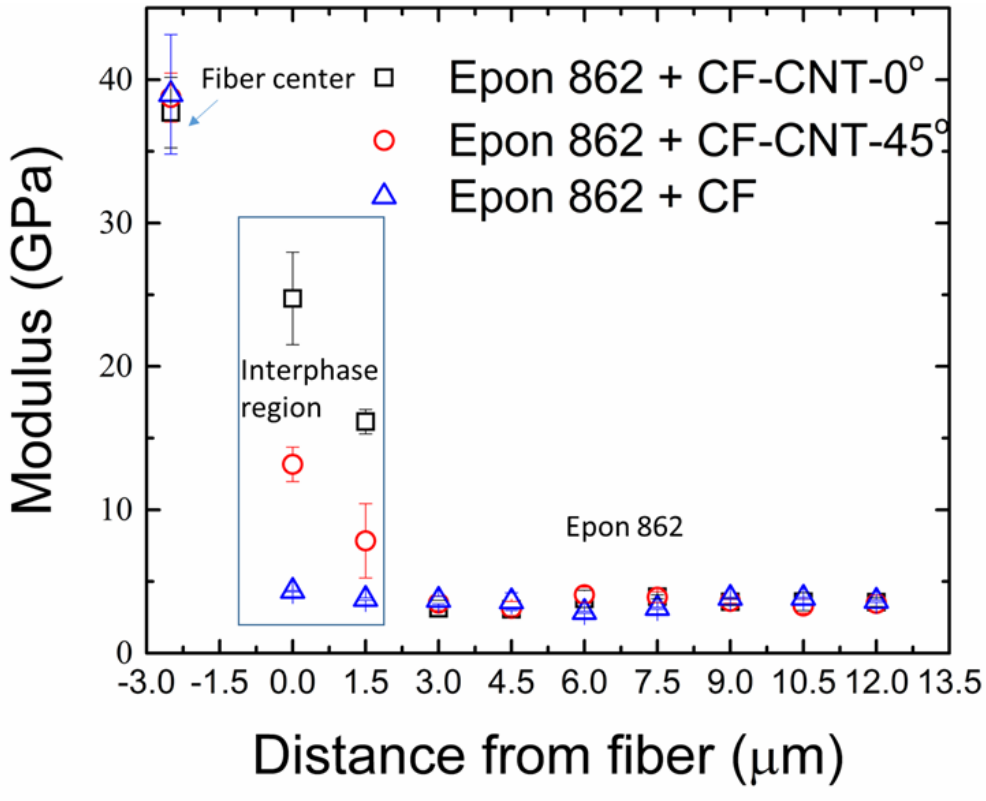


Figure 5.8. Modulus scanning results. X-axis denotes the distance from the fiber edge.

The enhancement of the interphase stiffness, as shown in Figure 5.8, is very promising, and it contributes to the improvement of interfacial shear strength as will be discussed in next section. FEM simulations were conducted to illustrate the effect of MWNT-polymer nanocomposite interphase region. A spherical tip with a diameter of 10 µm was used to make nanoindentation on the baseline and MWNT scrolled carbon fiber case. The nanoindentation modulus scan data was used as input for FEM simulations. The stress distribution underneath the nanoindenter is shown in Figure 5.9.

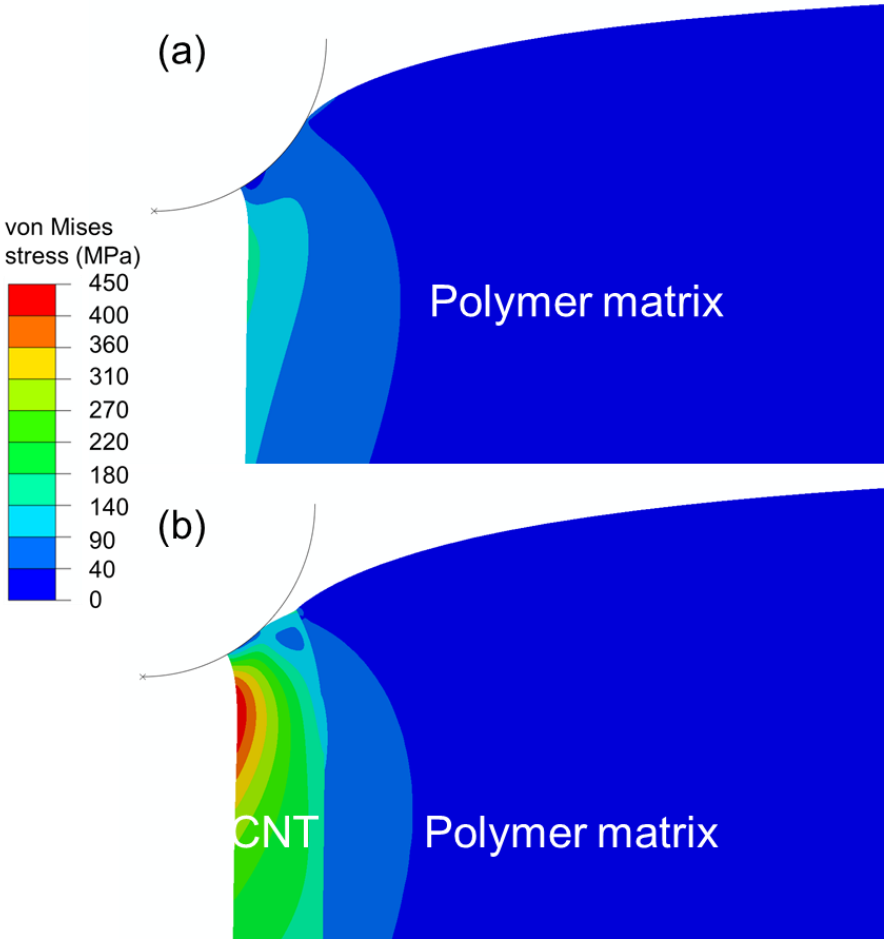


Figure 5.9. FEM simulations of a spherical nanoindentation (a) stress distribution of the baseline case, (b) stress distribution of the MWNT scrolled carbon fiber embedded in polymer matrix. The plot scale bar is same for both figures.

Figure 5.9 shows that the existence of MWNT-polymer nanocomposite interphase region plays a significant role: the stress transition from carbon fiber to polymer matrix became much smoother; and the maximum stress in matrix reduced from 152.9 MPa to 87.6 MPa, for baseline and MWNT scrolled carbon fiber case, respectively.

It is thus proposed the MWNT scrolling will enhance the interface strength by the following two mechanism working together: first, adhesion between MWNT ply and carbon fiber. The incorporation of the scrolled MWNTs increase the specific surface area significantly, improve Van der Waals interaction at the interface, hence the interfacial shear strength; second, MWNT wrapped carbon fiber is impregnated into the polymer matrix, polymer will infiltrate into the pores of the multilayer CNT sheet to bond with the carbon fiber to form CNT/polymer nanocomposite surrounding a fiber. It provides reinforcement to the interface between carbon fiber and polymer matrix. In order to examine the proposed enhancement, a series of experiments were conducted to measure the apparent interfacial shear strength, which will be discussed in details in next section.

## 5.4 Characterization of interfacial shear strength

It was determined that the MWNT/polymer nanocomposite in the interphase region has a modulus significantly higher than that of the polymer matrix, thus allowing stress to be optimally distributed in the interphase region – the maximum shear stress is much lower than the case without CNT scrolling carbon fiber under the same applied shear force. In this investigation, Different methods were used in experiments to characterize the interfacial shear strengths: these include fiber pull-out, fiber push-out by a nanoindenter tip, and push-in by a flat-ended

nanoindenters tip. Finite element analysis incorporating interfacial normal and shear traction separation laws in the cohesive interface was conducted to extract the interfacial shear strength.

### 5.4.1 Fiber pull-out

In this section, the interfacial shear strength is determined by using fiber pull-out test. A sized carbon fiber tow (IM7, Hexcel) was infiltrated with polyvinyl alcohol (PVA) to bind the fibers within the tow. Two different tows were used in this preliminary work, they are 250 μm and 130 μm. The MWNT aerogel sheets (10 mm long, 5 mm wide) were scrolled around each of the carbon fiber tows, and densified with acetone. A long fiber tow was cut into smaller segments for making the scrolled fibers and for the control specimen (without the use of MWNT sheet scrolling). Wrapping angle was 0º with the MWNT sheet aligned with the carbon fibers. The MWNT scrolled carbon was then immersed in epoxy matrix (Epon Resin 862, Hexion), and subsequently placed on a paper frame to hold the sample, as shown in Figure 5.10(a).

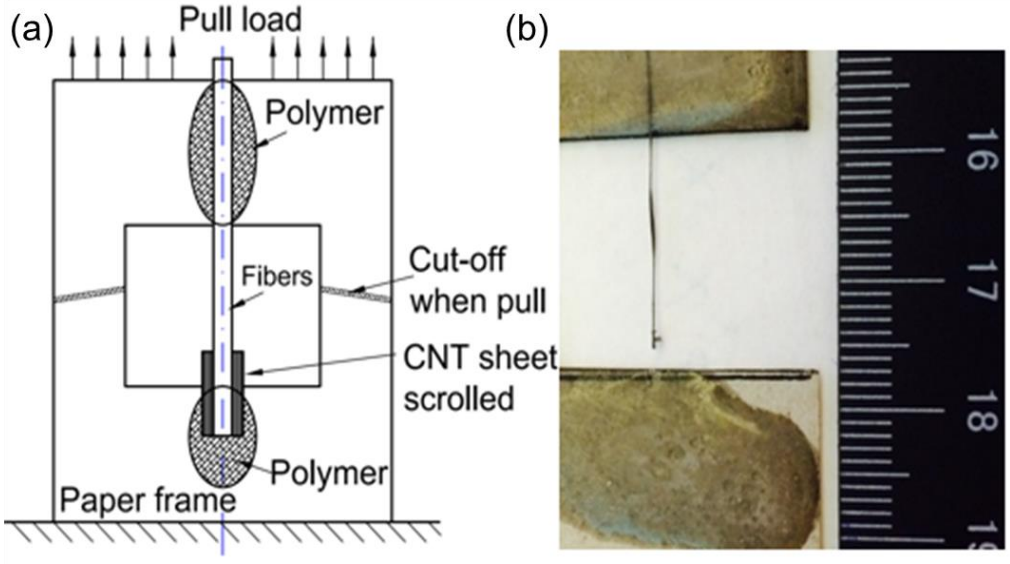


Figure 5.10. (a) A schematic for fiber pull-out test when a CNT scrolled fiber is embedded in a polymer at the bottom of the paper frame. (b) Fiber pulled out from epoxy matrix.

Different embedded lengths of the scrolled carbon fiber in epoxy were tried and it was found that the embedded length has to be small (typically ≤ 1 mm) in fiber pull-out test for CNT scrolled IM7 fiber due to enhanced interfacial shear strength, and hence smaller critical length. After curing for twelve hours the paper frame holding the embedded scrolled fiber sample was clamped in an Instron fixture for fiber pull-out test. For comparison, a control experiment was conducted using IM7 (without MWNT wrapping around it) fiber tow embedded in epoxy. Figure 5.10(b) shows that the fiber has been successfully pulled out with embedded length as 1 mm. The pull-out force was plotted as a function of displacement for each of the two cases and shown in Figure 5.11. The use of scrolled fiber embedded in epoxy has increased the pull-out force from an average value of 17.8 N to an average value of 30.0 N for the 130 μm (an increase of 68.5%), and has increased the pull-out force from 24.9 N to 35.2 N for the 250 μm tow (an increase of 41.4%).

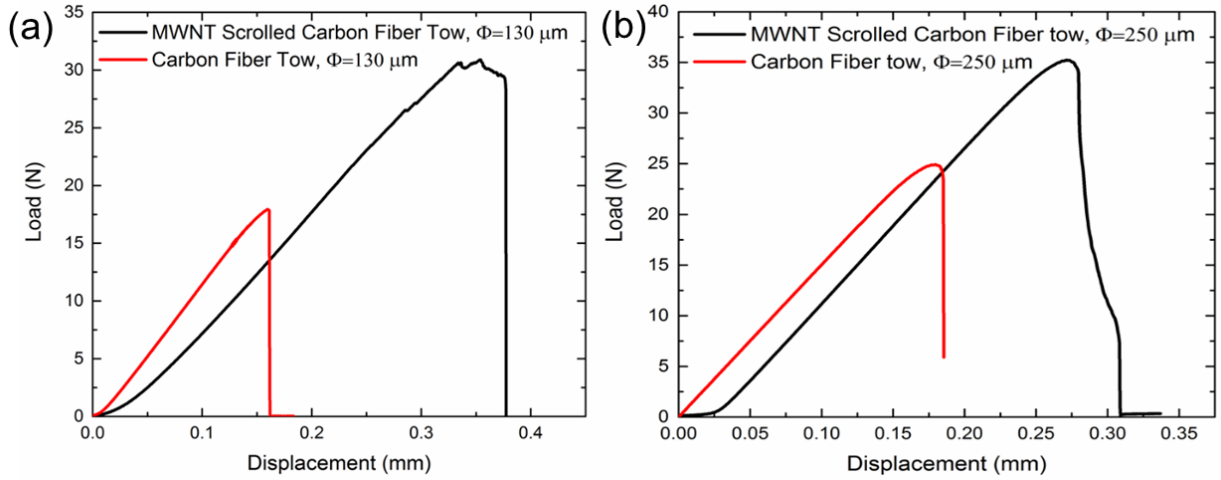


Figure 5.11. Force vs. displacement in the pull-out tests. Black lines are results for MWNTs sheet scrolled sized-carbon fiber. Red lines are results for the control without MWNT scrolling. (a) A carbon fiber tow with a diameter of 130 μm. CNT scrolling increased the pull-out force from 17.8 N to 30.0 N for the 130 μm tow (increase of 68.5 %). (b) A carbon fiber tow with a diameter of 250 μm. CNT scrolling has increased the pull-out force from 24.9 N to 35.2 N for the 250 μm (an increase of 41.4%).

The area enclosed by the pull-out force-displacement curve up to the peak load, indicative of the toughness or ductility of the interface, has improved in both cases. As mentioned earlier, in order to successfully pull out the fiber from the matrix, fiber embedded length has to be smaller than 1 mm, which is very hard to control, and is also a potential source for inducing errors. Thus some other approaches may be necessary to accurately determine the interfacial shear strength.

### 5.4.2 Fiber push-out: Experiment and FEM simulations

To further confirm the enhancement of interfacial shear strength provided by MWNT, we characterized the interfacial shear strength by fiber push-out test, a nanoindenter tip pushes the fiber out and the resulting load is recorded as a function of displacement for analytical or finite element analysis to determine the interfacial properties. Fiber push-out tests were conducted on a 40 μm tow embedded in a BMI (bismaleamide) polymer matrix. The embedded length of the tow was 60 μm that has been pushed out of the matrix using nanoindentation.

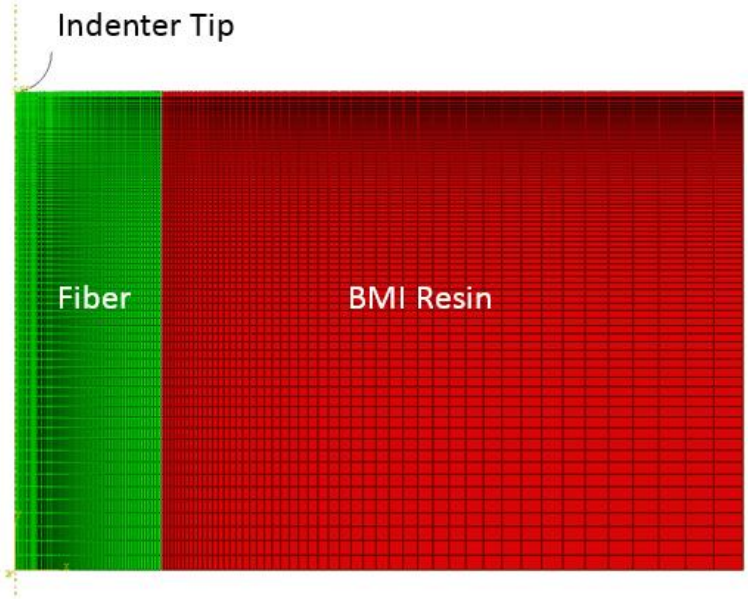


Figure 5.12. The FEM model for the simulation of fiber push-out experiment.

To extract the interfacial shear strength from push-out test, FEM analysis was conducted. In FEM simulations, an axisymmetric model was used as shown in Figure 5.12, both the fiber tow and BMI resin were assumed to be linearly elastic. The height of sample is 60 μm, diameter of the fiber tow is 40 μm, the 10 μm spherical indenter tip was modeled as rigid. A FEM model consists of nearly 15000 elements, with refined mesh in the region under indenter and at the interface between fiber and BMI resin. To model the delamination between fiber and matrix, a cohesive zone model was used and the interface was assumed to satisfy bilinear traction separation law (Equations (4.2)-(4.4)), which has been discussed in details in chapter 4.

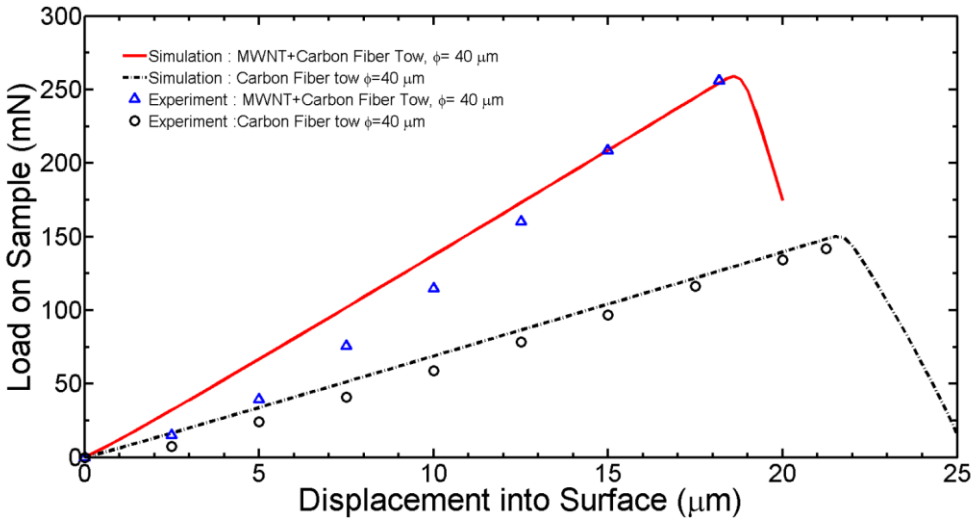


Figure 5.13. Force vs. displacement in the push-out tests. Solids line is simulation result for MWNTs sheet scrolled sized-carbon fiber. Dashed line is simulation result for the control without MWNT scrolling, a tow with a diameter of 40 μm. The blue triangle and the black round markers represent the experimental MWNT scrolled carbon fiber and carbon fiber alone, respectively.

An inverse calculation was conducted to fit nanoindentaton load-displacement curve into experimental results. Figure 5.13 shows both experimental and simulated load-displacement curves, the push-out force for control (fiber alone) is 141.68 mN in experiment, and 148.38 mN

in simulation. For fiber scrolled with WMNT, push-out force is 256 mN in experiment; and simulation gives a value of 258.65 mN. In both cases, simulation and experimental results agree with each push out force as a function of displacement for two cases: a carbon fiber embedded in BMI (baseline), and a CNT wrapped fiber embedded in a BMI resin.

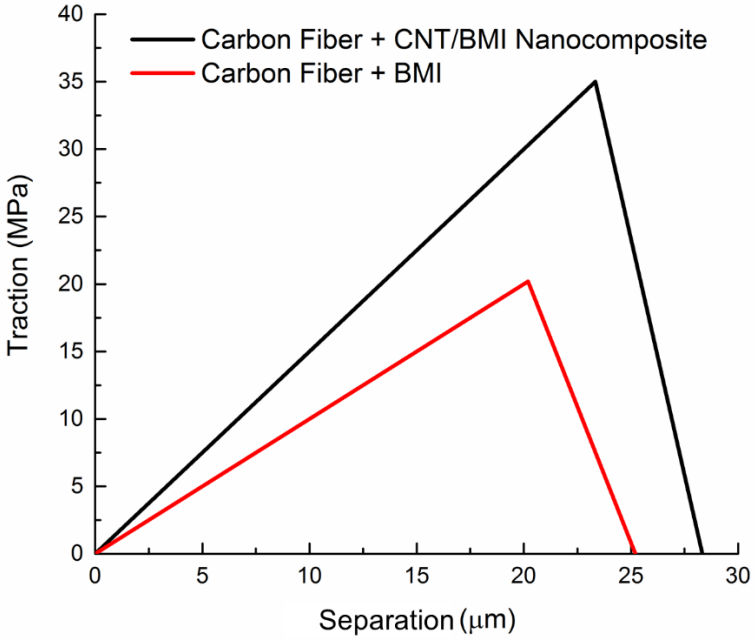


Figure 5.14. Bilinear traction separation law offer best-fit load-displacement curve between simulation and experiments.

The cohesive law used for the best-fit cases is shown in Figure 5.14, it can be seen that the use of scrolling CNT sheet delayed the onset of damage initiation, and increased fracture toughness (increases energy required to create a unit new surface. Note that the interfacial shear strength of carbon fiber (without MWNT warpped) is 19.8 MPa which is very close to experimentally determined value (18.79 MPa), and the interfacial shear strength used in MWNT scrolled simulation was 35 MPa, which is also very close to the interfacial shear strength 33.96 MPa determined by experiments.

### 5.4.3 Fiber push-in experiments and simulations

Over decades, a number of experimental techniques have been developed to assess fiber/matrix interface adhesion by characterizing the mechanically measured value of interfacial shear strength (IFSS). IFSS is commonly measured using micromechanical test methods such as the single-fiber fragmentation test, the microbond test, the single-fiber push-out test, and the fiber push-in test. The commonest measurement techniques applied to single-fiber microcomposites is the fiber fragmentation test. However, one drawback is that, if MWNT is wrapped around the single fiber, from our preliminary experimental efforts, it is very hard to observe the birefringent patterns for determining the fiber fracture length. Thus we are not able to evaluate the improvement on interfacial shear strength offered by MWNT via single-fiber fragmentation test. Other tests suffer from several experimental difficulties: the fiber pull-out test is not easy to perform because it requires a very short embedded length, in order to successfully pull out the fiber from the matrix instead of breaking the fiber, typically fiber embedded length has to be smaller than 1 mm, which is very hard to control, and is also a potential source for inducing errors. The fiber push-out test requires the cumbersome preparation of very thin sample (~50 μm), and sample tends to break during the polishing very easily, which results in a very low successful rate of sample preparation. These considerations lead to the need to conduct push-in test which is performed on a thicker real composite specimen with a thickness of few mm.

In this investigation, three types of samples are prepared: (a) sized IM7 fiber embedded in Epon 862 matrix (b) unsized IM7 fiber embedded in Epon 862 matrix (c) sized IM7 fiber wrapped by MWNT and embedded in Epon 862 matrix. Each sample was cured at room temperature for 24 hours. The cross section perpendicular to the fibers of the unidirectional

composite specimens were polished first by #800 and #1200 sandpaper, respectively. The specimens were then polished by a MultiPrepTM system polishing machine using alumina suspension with particle size from 1 μm to 50 nm in sequence. All the samples have the final dimensions approximately as 15 mm × 10 mm × 5 mm. All the fiber push-in nanoindentations were conducted on an Agilent G200 nanoindentation system. A flat punch tip (Micro Star Tech) of 2.2 μm in diameter was used in this investigation. In order to conduct nanoindentations on the IM7 carbon fibers (5 μm in diameter) as much center as possible, calibration was performed to obtain an accurate lateral position of the indenter relative to the sample surface with the use of an optical microscope on the nanoindentation system. All the fiber push-in nanoindenations were conducted at a constant loading rates of 1 mN/s. The experimental results are shown as in Figure 5.15.

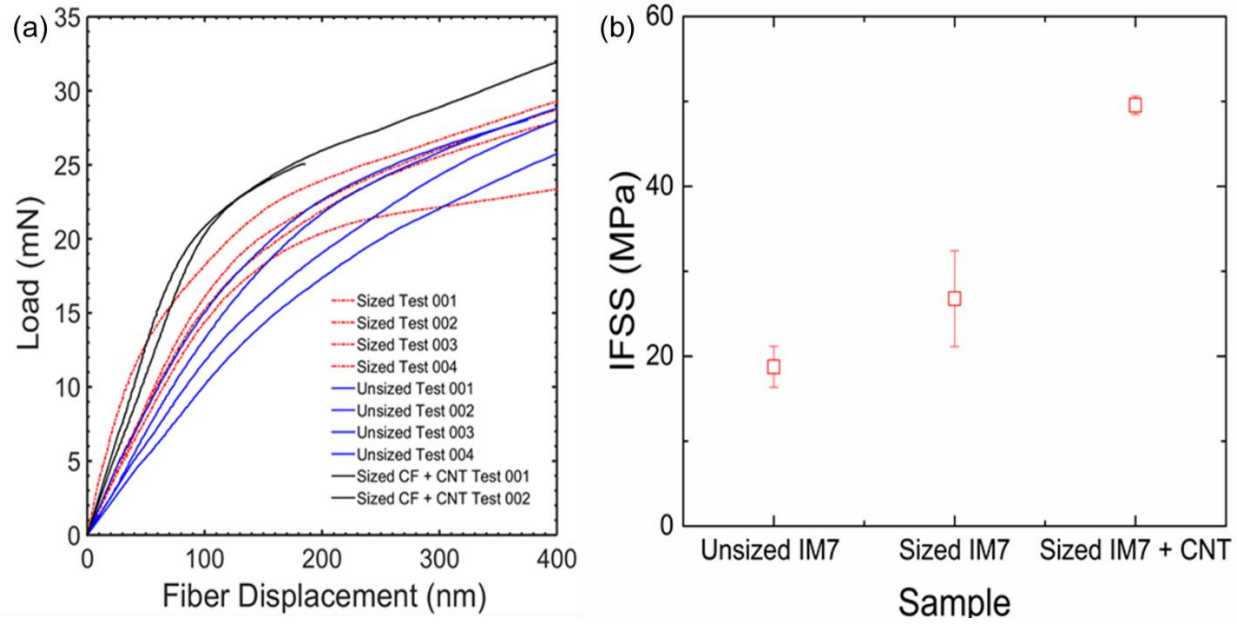


Figure 5.15. Fiber push-in experiments to determine IFSS : (A) Load displacement curves. The solid line is sized carbon fiber with CNT. The blue line is unsized fiber without CNT. The red dash line is sized fiber without CNT. (B) IFSS calculated by shear lag model.

The shear-lag model (Equation (4.1)), which has been well justified in Chapter 4, was used to determine the interfacial shear strength. The IFSS determined by Equation (4.1) are shown in Figure 5.15(b). Comparing sized IM7 wrapped by CNT (49.5±18.7 MPa) with sized IM7 without CNT (26.8±5.6 MPa), both embedded in Epon 862 matrix, introducing CNT results in 87% improvement in IFSS.

## 5.5 Conclusions

In this study, we have demonstrated the feasibility of repeatable fabrication of carbon fiber with different MWNT sheet bias angle has been established. The technique allows warpping a carbon fiber (or carbon fiber bundles) with MWNT sheet at different bias angles. Two different bias angles, namely $0^o$ and $45^o$, were fabricated as example. The MWNT scrolled carbon fiber in a polymer matrix to form a nanocomposite interphase region, thereby creating a well aligned CNT/polymer nanocomposite interphase region near a carbon fiber to enhance the mechanical stiffness, strength and ductility of the interphase. Modulus scanning has been performed, and it was found that the modulus in the interphase region has been improved significantly (200% and 400% for $0^o$ and $45^o$ MWNT wrapping respectively), thus allowing stress to be optimally distributed in the interphase region – the maximum shear stress is much lower than the case with MWNT scrolling carbon fiber under the same applied force. Different experimental methods were used to determine the interfacial shear strength, all of which show consistently a significant improvement by using MWNT scrolled carbon fibers in a composite.

## 5.6 References


1. Swadener, J. G., K. M. Liechti, and A. L. De Lozanne. "The intrinsic toughness and adhesion mechanisms of a glass/epoxy interface." *Journal of the Mechanics and Physics of Solids* 47, no. 2 (1999): 223-258.

2. Ding, W., A. Eitan, F. T. Fisher, X. Chen, D. A. Dikin, R. Andrews, L. C. Brinson, L. S. Schadler, and R. S. Ruoff. "Direct observation of polymer sheathing in carbon nanotube-polycarbonate composites." *Nano letters* 3, no. 11 (2003): 1593-1597.

3. Hussain, Farzana, Mehdi Hojjati, Masami Okamoto, and Russell E. Gorga. "Review article: polymer-matrix nanocomposites, processing, manufacturing, and application: an overview." *Journal of composite materials* 40, no. 17 (2006): 1511-1575.

4. Thostenson, Erik T., Chunyu Li, and Tsu-Wei Chou. "Nanocomposites in context." *Composites Science and Technology* 65, no. 3 (2005): 491-516.

5. Jia, Jingjing, Jingna Zhao, Geng Xu, Jiangtao Di, Zhenzhong Yong, Yuyu Tao, Chao Fang et al. "A comparison of the mechanical properties of fibers spun from different carbon nanotubes." *Carbon* 49, no. 4 (2011): 1333-1339.

6. Frankland, S. J. V., and Vasyl Michael Harik. "Analysis of carbon nanotube pull-out from a polymer matrix." *Surface Science* 525, no. 1 (2003): L103-L108.

7. Qian, Hui, Alexander Bismarck, Emile S. Greenhalgh, and Milo SP Shaffer. "Carbon nanotube grafted carbon fibres: a study of wetting and fibre fragmentation." *Composites Part A: Applied science and manufacturing* 41, no. 9 (2010): 1107-1114.

8. Chowdhury, S. C., and T. Okabe. "Computer simulation of carbon nanotube pull-out from polymer by the molecular dynamics method." *Composites Part A: Applied Science and Manufacturing* 38, no. 3 (2007): 747-754.

9. Sager, R. J., P. J. Klein, D. C. Lagoudas, Q. Zhang, J. Liu, L. Dai, and J. W. Baur. "Effect of carbon nanotubes on the interfacial shear strength of T650 carbon fiber in an epoxy matrix." *Composites Science and Technology* 69, no. 7 (2009): 898-904.

10. Fang, Chao, Jingna Zhao, Jingjing Jia, Zuoguang Zhang, Xiaohua Zhang, and Qingwen Li. "Enhanced carbon nanotube fibers by polyimide." *Applied Physics Letters* 97, no. 18 (2010): 181906.

11. Grimmer, Christopher S., and C. K. H. Dharan. "Enhancement of delamination fatigue resistance in carbon nanotube reinforced glass fiber/polymer composites." *Composites Science and Technology* 70, no. 6 (2010): 901-908.

12. Mei, Lei, Xiaodong He, Yibin Li, Rongguo Wang, Chao Wang, and Qingyu Peng. "Grafting carbon nanotubes onto carbon fiber by use of dendrimers." *Materials Letters* 64, no. 22 (2010): 2505-2508.

13. Zhang, Fu-Hua, Rong-Guo Wang, Xiao-Dong He, Chao Wang, and Li-Ning Ren. "Interfacial shearing strength and reinforcing mechanisms of an epoxy composite reinforced using a carbon nanotube/carbon fiber hybrid." *Journal of materials science* 44, no. 13 (2009): 3574-3577.

14. Godara, A., Larissa Gorbatikh, Gerhard Kalinka, A. Warrier, O. Rochez, L. Mezzo, F. Luizi, A. W. Van Vuure, S. V. Lomov, and I. Verpoest. "Interfacial shear strength of a glass fiber/epoxy bonding in composites modified with carbon nanotubes." *Composites Science and Technology* 70, no. 9 (2010): 1346-1352.

15. Siddiqui, Naveed A., Man-Lung Sham, Ben Zhong Tang, Arshad Munir, and Jang-Kyo Kim. "Tensile strength of glass fibres with carbon nanotube–epoxy nanocomposite coating." *Composites Part A: Applied Science and Manufacturing* 40, no. 10 (2009): 1606-1614.

16. Zhang, Y. C., and X. Wang. "Thermal effects on interfacial stress transfer characteristics of carbon nanotubes/polymer composites." *International journal of solids and structures* 42, no. 20 (2005): 5399-5412.

17. Zhang, Mei, Shaoli Fang, Anvar A. Zakhidov, Sergey B. Lee, Ali E. Aliev, Christopher D. Williams, Ken R. Atkinson, and Ray H. Baughman. "Strong, transparent, multifunctional, carbon nanotube sheets." *Science* 309, no. 5738 (2005): 1215-1219.

18. Zhang, Mei, Ken R. Atkinson, and Ray H. Baughman. "Multifunctional carbon nanotube yarns by downsizing an ancient technology." *Science* 306, no. 5700 (2004): 1358-1361.

19. Dalton, Alan B., Steve Collins, Edgar Muñoz, Joselito M. Razal, Von Howard Ebron, John P. Ferraris, Jonathan N. Coleman, Bog G. Kim, and Ray H. Baughman. "Super-tough carbon-nanotube fibres." *Nature* 423, no. 6941 (2003): 703-703.

20. Baughman, Ray H., Anvar A. Zakhidov, and Walt A. de Heer. "Carbon nanotubes--the route toward applications." *science* 297, no. 5582 (2002): 787-792.

21. Baughman, Ray H., Changxing Cui, Anvar A. Zakhidov, Zafar Iqbal, Joseph N. Barisci, Geoff M. Spinks, Gordon G. Wallace et al. "Carbon nanotube actuators." *Science* 284, no. 5418 (1999): 1340-1344.

22. LU, Hongbing, Ray H. Baughman, Mohammad H. Haque, and Shaoli D. Fang, "Method of fabricating carbon nanotube sheet scrolled fiber reinforced polymer composites and compositions and uses thereof", U.S. Patent 20,160,024,262, issued January 28, 2016.

# CHAPTER 6

# CONCLUSIONS AND OUTLOOK

## 6.1 Conclusions

In this study, nanoindentation was used to characterize the mechanical behavior of multiple materials at small scales, which includes viscoelastic behavior of SU-8 negative photoresist, temperature-dependent modulus of molding compound in integrated circuits, interface degradation of carbon fiber reinforced polymer matrix composites due to the environmental effects; and enhancement in interface properties by introducing a carbon nanotube sheet scrolling fiber as reinforcement.

The mechanical properties of SU-8 at microscale were measured under both micropillar compression and nanoindentation on a film on a substrate. The effects of loading rate and micropillar size are examined. It was determined that the SU-8 exhibits viscoelastic properties at room temperature, the time-average Young's modulus increases in general with the loading rate. The average Young's modulus determined by compression of a micropillar was 4.1 GPa at a strain rate near $10^{-3}$ $s^{-1}$. For nanoindentation on a SU-8 film supported by a silicon substrate, the default output from the nanoindenter for the Young's modulus was approximately 6.0 GPa with the consideration of elastic-plastic behavior of the SU-8. When the viscoelastic effects were considered, the time-average Young's modulus at a given strain rate was determined to be near 3.6 GPa, which agrees with the reported values in literature obtained from tension and bending, and also correlates reasonably well with data from microcompression. This work indicates that viscoelastic analysis is necessary to extract the valid mechanical properties at nano/microscales for SU-8.

The mechanical properties of a molding compound on a packaged integrated circuit were measured by spherical nanoindentation using a 50 μm radius diamond tip. Statistical analysis was conducted to determine the representative volume element (RVE) size for a nanoindentation grid. Nanoindentation was made on the RVE to determine the effective viscoelastic properties. The relaxation functions were converted to temperature-dependent Young's modulus at a given strain rate at several elevated temperatures. The Young's modulus values at a given strain rate from nanoindentation were found to be in a good agreement with the corresponding data obtained from tensile samples at or below 90°C. However, the values from nanoindentation were significantly lower than the data obtained from tensile samples when the temperature was near or higher than 110°C, which is near the glass transition. The spatial distribution of the Young's modulus at a given strain rate was determined using nanoindentation with a Berkovich tip. The spatial variation of the Young's modulus at a given strain rate is due to the difference in nanoindentation sites (glass beads, epoxy or the interphase region). A graphical map made from an optical micrograph agrees reasonably well with the nanoindentation results.

Fiber push-in nanoindentation was conducted on a unidirectional carbon fiber reinforced bismaleimide resin composite (IM7/BMI) after thermal oxidation to determine the interfacial shear strength. A unidirectional IM7/BMI laminated plate was isothermally oxidized under various conditions, including in air for 2 months at 195°C and 245°C, and immersed in water for 2 years to reach a moisture-saturated state. The water-immersed specimens were subsequently heated to 260°C upon sudden heating, or under slow heating at a rate of approximately 6°C/min, respectively. A flat punch tip of 3 μm in diameter was used to push the fiber into the matrix while the resulting load-displacement data was recorded. From the load-displacement

relationships, the interfacial shear strength was determined using a shear-lag model, which was verified by finite element method simulations. It was found that thermal oxidation at 245ºC in air leads to a significant reduction in interfacial shear strength of the IM7/BMI unidirectional composite, and moisture concentration has a negligible effect on the interfacial shear strength. For moisture-saturated specimens under a slow heating rate, there is no detectable reduction in the interfacial shear strength. In contrast, the moisture-saturated specimens under thermal shock showed a significant reduction in interfacial shear strength. Scanning electron micrographs of IM7/BMI composite reveal that both thermal oxidation at 245ºC in air and sudden heating induced debonding along the fiber/matrix interface, thereby weakening the interface.

A method is introduced to use carbon nanotube (CNT) sheet to scroll carbon fibers to enhance the interfacial shear strength of the composite. The CNT sheet is drawn from multiwall carbon nanotube (MWNT) forest, it is then used to wrap around a carbon fiber, and is impregnated into polymer matrix. Since CNT is meso-porous with high specific surface area, a very small amount of CNT sheet in mass can wrap around a large volume of carbon fibers. The CNT scrolled carbon fiber in a polymer matrix to form a nanocomposite interphase region, thereby creating a well aligned CNT/polymer nanocomposite interphase region near a carbon fiber to enhance the mechanical stiffness, strength and ductility of the interphase. The technique allows wrapping a carbon fiber with CNT sheet at different bias angles. Nanoindentation was made to measure the spatial distribution of the Young's modulus in the interphase region containing the MWNT/polymer nanocomposite. It was determined that the MWNT/polymer nanocomposite in the interphase region has modulus significantly higher than that of the polymer matrix, thus allowing stress to be optimally distributed in the interphase region – the maximum

shear stress is much lower than the case without CNT scrolling carbon fiber under the same applied shear force. Different methods were used in experiments to characterize the interfacial shear strengths; these include fiber pull-out, fiber push-out by a nanoindenter tip, shear of a microbond attached to a carbon fiber and push-in by a flat-ended nanoindenter tip. Finite element analysis incorporating interfacial normal and shear traction separation laws in the cohesive interface was conducted to extract the interfacial shear strength. All experimental results show consistently a significant improvement in interfacial shear strength by using MWNT scrolled carbon fibers in a composite.

## 6.2 Outlook

Beyond the work in this thesis, the following questions remain interesting to explore in future work.

### 6.2.1 FEM Simulation of SU-8 microcompression

There is difference between simulation results and experimental data and the difference occurs in the plastic regime. In current simulation, an elastic-perfectly plastic model was used, with an intention to simulate the linear response, and the onset of plastic deformation to extract Young's modulus and yield strength. The model used in our simulation does not have ability to capture hardening or softening, if any in the material. The strain-bursts shown in Figure 2.6 suggest the existence of a relatively strong strain softening in the plastic region. Once plastic deformation occurs, it continues catastrophically until the micropillar is fully compressed. To simulate the entire plastic deformation, another appropriate nonlinear constitutive model is needed. This is beyond the scope of the current study, which focused on measurements of Young's modulus. In

the future, simulations with other constitutive models need to be conducted to reach agreement with experiments. This has been tried by implementing Boyce vicoplastic model through VUMAT. However, there are still some deficiencies. In order to quantitatively characterize the strain softening, a displacement-controlled nanoindentation system is needed. In-situ nanoindentation system "Nanofilp" may be an option, which can record the deformation process, and compared with FEM simulation.

### 6.2.2 Long-term viscoelastic properties of molding compound at service tempertures

In current study, the relaxation modulus measured by use of nanoindentation. The specimen IC was potted, cross-sectioned and polished prior to the testing. However the relaxation time was 5 seconds. Additional temperature points and length of time are needed to complete the viscoelastic master curve used in the constitutive relationship in a structural analysis. In future work, uniaxial relaxation experiments can be conducted on molding compound in bulk form, the relaxation experiment can be conducted to find the relaxation modulus over a period of $10^4$ s. The selected strain measurement technique will be a non-contact measurement method referred to as digital image correlation technique (DIC).

### 6.2.3 Wrap carbon fibers with MWNT sheet to form fiber tows

In the current research, we have characterized the interfacial shear strength of MWNT scrolled single carbon fiber composite using a suite of technique, including fiber-pull out, fiber push-out, fiber push-in nanoindentation, and observed consistently improved interfacial shear. All data indicated an improvement of interfacial shear strength from 40% to over 100% from the baseline data obtained from the situation where MWNT sheet was not used. The significant enhancement

in interfacial shear strength has potential to translate into enhanced strengths in compression, shear and perhaps even in tension. Our current method, however, relies on primarily manual operations and thus cannot produce enough materials for ASTM standard testing on larger samples for validation, or for making large volume of materials for practical applications.

In future work, a continuous nanomanufacturing process can be developed to wrap individual carbon fibers with MWNT sheet to form tows. This scalable nanomanufacturing process should allow preparation of large quantities of MWNT scrolled tows, which will be subsequently used to prepare unidirectional or woven prepregs for use in polymer matrix composites. ASTM standard composite testing can then be conducted using samples prepared from these prepregs, and modeling and simulations will be conducted to optimize the material design, and the processing conditions.

## BIOGRAPHICAL SKETCH

Tingge Xu was born in Zhongjiang, Sichuan province, China in 1992. In the 2009 National College Entrance Examination, he ranked 1st in Zhongjiang and was admitted by Shanghai Jiao Tong University, where he obtained his B.S. degree in 2013, majoring in Mechanical Engineering. After graduation, he came to The University of Texas at Dallas to pursue his PhD degree under the supervision of Dr. Hongbing Lu. His current research focuses on mechanical characterization of microelectronics, composites, and time-dependent materials at small scales. His research involved a combination of experiments (primarily nanoindentation), analytical modelling, and numerical simulation (mainly finite element method). He received the best graduate student award from ASEM North Texas Section. He was also the recipient of multiple travel grants and scholarships.

# CURRICULUM VITAE

Tingge Xu

## Education

**The University of Texas at Dallas (UTD)** Richardson, TX
Ph.D. in Mechanical Engineering Advisor: Dr. Hongbing Lu May 2017
Cumulative GPA: **4.0/4.0**

**Shanghai Jiao Tong University (SJTU)** Shanghai, China
B. Eng. of Mechanical Engineering & Automation June 2013
Honor class

## Professional Experience

*Research Assistant*, **Department of Mechanical Engineering, UTD**, Richardson, TX 08/2013-Present

- Four years of experience on mechanical characterization of microelectronics, composites, and time-dependent materials at small scales. My research involved a combination of experiments (primarily nanoindentation), analytical modelling, and numerical simulation (mainly finite element method).

*Teaching Assistant,* **Department of Mechanical Engineering, UTD**, Richardson, TX 08/2014-05/2016

- Advanced Solid Mechanics (graduate level), Continuum Mechanics (graduate level)
- Mechanics of Materials Laboratory (undergraduate level)

## Publications

1. **Tingge Xu**, Yingjie Du, Huiyang Luo, Gyu-ho Kim, Zhe Xu, Majid Minary-Jolandan, Les Stark, Terry Baughn, and Hongbing Lu, "Measurement of Temperature-Dependent Young's Modulus at a Strain Rate for a Molding Compound by Nanoindentation," *Experimental Mechanics*, 2016. DOI 10.1007/s11340-016-0205-7
2. **Tingge Xu**, Jun Hyeon Yoo, Sachin Babu, Samit Roy, Jeong-Bong Lee and Hongbing Lu, "Characterization of the mechanical behavior of SU-8 at microscale by viscoelastic analysis," *Journal of Micromechanics and Microengineering*, 26, 105001, 2016
3. Zhenxing Hu, **Tingge Xu**, Huiyang Luo, Rong Z. Gan, and Hongbing Lu, "Measurement of thickness and profile of a transparent material using fluorescent stereo microscopy," *Optics Express* 24, 29822-29829 2016
4. Yingjie Du, **Tingge Xu**, Thomas M Shaw, Xiao Hu Liu, Griselda Bonilla, Han Li, and Hongbing Lu, "A novel tri-layer nanoindentation method to measure the mechanical properties of a porous brittle ultra-low-K dielectric thin film", *Extreme Mechanics Letters*, 2017, in press
5. **Tingge Xu**, Huiyang Luo, Zhe Xu, Zhenxing Hu, Majid Minary-Jolandan, Samit Roy, and Hongbing Lu, "Evaluation of the effect of thermal oxidation and moisture on the interfacial shear strength of unidirectional IM7/BMI composite by fiber push-in nanoindentation", *Experimental Mechanics*, under review
6. **Tingge Xu**, Yingjie Du, Huiyang Luo, Zhenxing Hu, Lei Guo, and Hongbing Lu, "Characterization of the Mechanical Properties of Mason sand at Grain-Level by nanoindentation", *Experimental Mechanics*, in preparation

7. Huiyang Luo, Zhenxing Hu, **Tingge Xu**, and Hongbing Lu, "High-strain rate compressive behavior of a clay under uniaxial strain state", *Dynamic Behavior of Materials*, Volume 1. Springer International Publishing, 2017, 117-122.
8. Huiyang Luo, **Tingge Xu**, Xuemin Wang, and Hongbing Lu "Interaction of Shock Wave with Granular Materials", *Challenges in Mechanics of Time Dependent Materials*, Volume 2. Springer International Publishing, 2016. 35-43.
9. Katsuyuki Sakuma, Buck Webb, Xiao Hu Liu, John Knickerbocker, Thomas Weiss, Shidong Li, Hongqing Zhang, Conor R Thomas, Eric Perfecto, **Tingge Xu**, and Hongbing Lu "Fluxless Bonding Process Using Thermo-Compression Micro-Scrub for 61 μm Pitch SnAg Solder 3-D Interconnections", In Electronic Components and Technology Conference (ECTC), 2016 IEEE 66th, pp. 329-335. IEEE, 2016.

## Conference Presentation (Selected)

1. **Tingge Xu**, Jun Hyeon Yoo, Jeong-Bong Lee, and Hongbing Lu, "Mechanical properties characterization of SU-8 at microscale by viscoelastic analysis", 2017 SEM Annual-A305, June 12-15, 2017, Indianapolis, Indiana
2. **Tingge Xu**, Huiyang Luo, Zhenxing Hu, Samit Roy, and Hongbing Lu, "Evaluation of Environmental Effects on Interfacial Shear Strength of Unidirectional IM7/BMI Composite by Nanoindentation", 2017 SEM Annual-A194, June 12-15, 2017, Indianapolis, Indiana
3. **Tingge Xu**, Huiyang Luo, Samit Roy, and Hongbing Lu, "Effects of Thermal Oxidation on the Interfacial Shear Strength of IM7/BMI Composite by Fiber Push-in Nanoindentation", 14$^{th}$ International Conference on Fracture (ICF14), June 18-23, 2017, Rhodes, Greece
4. **Tingge Xu,** Yingjie Du, Xiao Hu Liu, Thomas M. Shaw, Griselda Bonilla, and Hongbing Lu, "Try-Layer Nanoindentation for Mechancial Characterization of Ultra-Low-K Dielectrics", IEEE International Interconnect Technology (IITC), May 16-18, 2017, Hsinchu, Taiwan
5. **Tingge Xu**, Gyu-ho Kim, Jing Lu et al., "Carbon Nanotube Sheet Scrolled Fiber Composite for Enhancement in Interfacial Shear Strength", IMECE2016-65736, November 11-27, 2016, Phoenix, Arizona
6. **Tingge Xu**, Yingjie Du, Gyu-ho Kim et al., "Measurement of Temperature-Dependent Young's Modulus of Molding Compound at Elevated Temperatures", InterPACKICNMM2015-48157, July 6-9, 2015, San Francisco, CA
7. **Tingge Xu**, Gitogo Churu, Alison Lee et al., "Mechanics of Aerogels – Modeling and Simulations of Multifunctionalities: Part II", IMECE2014-4028, November 14-20, 2014, Montreal, Canada
8. **Tingge Xu**, Gitogo Churu, Alison Lee et al., "Mechanics of Aerogels – Modeling and Simulations of Multifunctionalities: Part I", IMECE2014-4027, November 14-20, 2014, Montreal, Canada

## Selected Honors and Awards

2016 Cyrus Cantrell III UTD Phi Kappa Phi Travel Grant
2016 PhD Research Small Grant at UTD
2016 Louis Beecherl, Jr. Graduate Fellowship at UTD
2016 Phi Kappa Phi Honor Society
2015 ASME Graduate Student Award (North Texas Section)
2015 Ericsson Graduate Fellowship at UTD
2014 Golden Key International Honor Society
2012 National Encouragement scholarship
2011&2012 Academic Excellent student scholarship in SJTU